



THE HONG KONG
POLYTECHNIC UNIVERSITY

香港理工大學

Pao Yue-kong Library

包玉剛圖書館

Copyright Undertaking

This thesis is protected by copyright, with all rights reserved.

By reading and using the thesis, the reader understands and agrees to the following terms:

1. The reader will abide by the rules and legal ordinances governing copyright regarding the use of the thesis.
2. The reader will use the thesis for the purpose of research or private study only and not for distribution or further reproduction or any other purpose.
3. The reader agrees to indemnify and hold the University harmless from and against any loss, damage, cost, liability or expenses arising from copyright infringement or unauthorized usage.

IMPORTANT

If you have reasons to believe that any materials in this thesis are deemed not suitable to be distributed in this form, or a copyright owner having difficulty with the material being included in our database, please contact lbsys@polyu.edu.hk providing details. The Library will look into your claim and consider taking remedial action upon receipt of the written requests.

**ACOUSTIC BEHAVIOR OF MICRO-PERFORATED
PANELS IN GRAZING FLOW**

XIAOQI ZHANG

PhD

The Hong Kong Polytechnic University

2020

The Hong Kong Polytechnic University

Department of Mechanical Engineering

**ACOUSTIC BEHAVIOR OF MICRO-PERFORATED
PANELS IN GRAZING FLOW**

Xiaoqi Zhang

**A thesis submitted in partial fulfillment of the
requirements for the degree of Doctor of Philosophy**

December 2019

Certificate of originality

I hereby declare that this thesis is my own work and that, to the best of my knowledge and belief, it reproduces no material previously published or written, nor material that has been accepted for the award of any other degree or diploma, except where due acknowledgement has been made in the text.

Xiaoqi Zhang

(Signed)

(Name of student)

Abstract

Micro-perforated panels (MPPs) are widely used for broadband sound absorptions. A MPP exposed to a grazing flow is an important problem in acoustics and has many practical engineering applications. Despite the considerable efforts and the progress made during the last decades, many fundamental issues still remain to be addressed. To mention a few, explanations on the sound energy dissipation mechanism in the presence of flow are not consistent and convincing in the open literature; existing acoustic impedance formulae based on different flow parameters give inconsistent results etc. This calls for a systematic investigation of these important issues and eventually find more intrinsic flow parameters allowing for a reliable acoustic impedance prediction.

In this thesis, 3D CFD simulations are conducted on a MPP with a backing space in a flow duct. Numerical analyses allow scrutinizing the flow field near the perforation hole and its interaction with the incoming acoustic waves, identifying viscous dissipation in the shear layer near the orifice as the dominant sound energy dissipation mechanism in a linearly low acoustic excitation regime, identifying the flow velocity gradient in the viscous sublayer as the intrinsic flow parameter and showing its linear relationship with a flow-related term in the acoustic resistance formula. Through a linear regression analysis, a new set of acoustic impedance formula is proposed, applicable within a certain flow range under the linear acoustic regime. The proposed impedance formulae are validated through comparisons with existing impedance data

reported in the open literature as well as with experimentally measured results using an inverse derivation method. Results show a good agreement with these data and the superiority of the proposed impedance formulae over the existing ones in terms of prediction accuracy.

Capitalizing on the established acoustic impedance prediction formulae, the noise attenuation performance of MPPs in flow ducts with grazing flow is investigated for various configurations. Incorporating the acoustic impedance formulae into the general Patch Transfer Function (PTF) framework, numerical analyses are conducted to analyze the effects of various system parameters and to shed light on the underlying sound attenuation mechanism of MPP silencers in flow ducts. Effects of various system parameters, such as grazing flow velocities, solid partitions inside the backing cavity of the MPPs, their dimension and other panel parameters, are examined in view of providing guidelines for the practical design of MPP-based silencers. The numerically predicted noise attenuation curves are then validated through comparisons with measurements under various grazing flow conditions.

Finally, the feasibility of integrating MPPs in a simplified home appliance model having a more complex geometry and being subjected to flow is explored. Two methods, the hybrid theoretical-numerical technique based on PTF approach and the other one using coordinate transformation technique, are presented to tackle the numerical challenges in coping with the increasing system complexity. The possibility of

implementing MPP absorbers in practical industrial devices for acoustic noise mitigation is demonstrated. Results reveal a hybrid noise reduction mechanism and point at the need for proper systematic parameter tuning in order to achieve the noise control target. As an illustration, a few selected optimization problems are discussed to highlight the efficacy of the PTF approach alongside the proposed acoustic impedance prediction formulae established in this thesis. Meanwhile, the improved capability and efficiency of the improved PTF approach based on coordinate transformation are also demonstrated by comparing with the optimization results from hybrid theoretical-numerical treatment.

Publications arising from the thesis

Journal papers

[1] **X. Zhang** and L. Cheng. "Acoustic impedance of micro-perforated panels in a grazing flow." *The Journal of the Acoustical Society of America*, 2019, 145 (4): 2461-2469.

[2] **X. Zhang**, C. Yang, L. Cheng, and P. Zhang, "An experimental investigation on the acoustic properties of micro-perforated panels in a grazing flow," *Applied Acoustics*, 2020, 159:107119.

[3] **X. Zhang** and L. Cheng. "Acoustic silencing in a flow duct with micro-perforated panel liners," *Applied Acoustics*, 2020, 167:107382.

Conference paper

X. Zhang and L. Cheng. "Numerical studies of the acoustic impedance of micro-perforated panels under grazing flow." *The 25th ICSV Conference paper*, 2018.

Acknowledgements

First and foremost, I would like to take this opportunity to express my gratitude to my supervisor Prof. Li Cheng for his guidance, inspiration, and encouragement during my stay in PolyU. He has been providing me with an excellent atmosphere to freely pursue new understandings while guiding me in the correct direction toward the target.

I also wish to thank Dr. Choy, Dr. Cheng Yang, Dr. Stephen, Mr. Penglin Zhang, Mr. Chong Wei and Mr. Long Wei for their help in the experiments. Many thanks to Dr. Zhongyu Hu and Dr. Xiang Yu for helping me understand the framework of PTF approach.

Thanks to all my groupmates, Dr. Zhongyu Hu, Dr. Shengbo Shan, Mr. Tong Zhou, Mr. Fuzhen Wen, Ms. Li Ma, Ms. Liling Tang, Ms. Linli Zhang, Dr. Shancheng Cao and Dr. Qi Xu, who have helped to make my study a pleasant one.

Last but most importantly, I would like to give my special thanks to my parents, my wife and my daughter for their unconditional love and support for my PhD study.

Table of contents

Certificate of originality.....	I
Abstract.....	II
Publications arising from the thesis	V
Acknowledgements.....	VI
Table of contents	VII
List of figures.....	XI
List of tables.....	XVIII
Nomenclature.....	XIX
Chapter 1. Introduction.....	1
1.1 Background.....	1
1.2 Literature review.....	2
1.2.1 Conventional sound absorption materials.....	2
1.2.2 Micro-perforated panels and Crandall's theory on acoustic propagation in a single tube	5
1.2.3 Impedance model of Micro-perforated panels without flow	9
1.2.4 Works on MPP without flow.....	11
1.2.5 MPPs with grazing flow.....	13
1.3 Motivations and thesis layout	17
Chapter 2. CFD Simulations and Energy Dissipation Mechanism	21
2.1. Computational model and simulation method	21

2.1.1. Model	21
2.1.2. Computational method	26
2.2. Validation of the CFD model	30
2.2.1. Mean stream-wise velocity	30
2.2.2. Friction velocity	32
2.2.3. Acoustic impedance simulation and comparisons with experiments...	34
2.3. Flow field visualizations and analyses	37
2.3.1. Flow field at different Mach numbers.....	38
2.3.2 Flow field at different SPLs	40
2.3.3 Sound energy dissipation mechanism	42
2.3.4 Increase of the acoustic resistance with flow velocity	44
2.3.5. Intrinsic flow parameters for acoustic impedance prediction	45
2.4. Summary	46
Chapter 3. Impedance Prediction Formula and Validation	50
3.1. Acoustic impedance prediction formula	50
3.1.1. Relationship between the velocity gradient and the acoustic resistance of MPPs.....	50
3.1.2. Impedance prediction model of MPPs and validations.....	54
3.2. Impedance derivation method.....	61
3.3 Measurements	66
3.3.1 Test sample.....	66
3.3.2 Experimental set-up	67

3.4. Results and discussions.....	70
3.4.1 Mean flow profile in the duct.....	70
3.4.2 Measured and predicted MPP acoustic impedance.....	71
3.5. Summary.....	75
Chapter 4. MPPs in Simple Acoustic Environment under a Grazing Flow.....	76
4.1. Absorption coefficient calculations.....	77
4.2. Grazing flow effects.....	78
4.3. Effects of the hole diameter	82
4.4. Effects of the perforation ratio	85
4.5. Summary.....	88
Chapter 5. MPPs in Flow Ducts	90
5.1. Principle of the PTF approach	93
5.2. PTF calculations of conventional subsystems	99
5.2.1 PTFs of an acoustic cavity	99
5.2.2 PTFs of a semi-infinite duct.....	102
5.2.3 PTFs of the MPP.....	104
5.3. Formulations of the flow duct problem	106
5.4. Experimental validations	112
5.5. Numerical results and analyses.....	118
5.5.1. Grazing flow effects.....	118
5.5.2. Effects of the partition inside the backing cavity.....	126
5.5.3 Effects of panel parameters.....	128

5.6. Summary	136
Chapter 6. MPPs in Noise Control Devices with Complex Geometry.....	138
6.1. Formulation of the problem	139
6.2. Experimental validations	145
6.3. Numerical results and analyses	153
6.3.1. Duct without MPP.....	153
6.3.2. Effects of the MPP absorber	156
6.3.3. Parametric studies	158
6.3.4. Optimizations.....	163
6.4. Improved PTF approach for systems with geometric complexities.....	168
6.4.1. PTF calculations of irregular cavity with coordinate transformation	169
6.4.2. Effects of the shape of irregular cavity	175
6.4.3. Optimizations	178
6.5. Summary	180
Chapter 7. Conclusions and Future Work.....	182
References:.....	189

List of figures

Figure 1.1. A Micro-perforated panel.	6
Figure 1.2. Schematic drawing of an angular ring of fluid.	7
Figure 2.1. Perforated panel (left) modeled by a single Helmholtz resonator (right)..	22
Figure 2.2. System model.	23
Figure 2.3. Acoustic pressure (a) and the corresponding normal velocity (b) at the hole inlet section. $M=0.2$, 3.15 kHz, $ V_a = 0.025m/s$	25
Figure 2.4. Mean x-velocity profiles at different locations upstream the resonator, through the $y=0$ cross section. $M=0.25$	31
Figure 2.5. Semi-log plots of the mean stream-wise velocity profile upstream the resonator at $x = -50mm$, through $y=0$ cross section. $M=0.25$	32
Figure 2.6. Comparison of the friction velocity between CFD and the empirical equation [92].	34
Figure 2.7. Comparison of the normalized acoustic impedance of panel 1 between CFD and experiments.	37
Figure 2.8. Velocity stream-lines of mean grazing flow near the hole of the resonator through $y=0$ cross section at different flow Mach numbers. (a) $M=0.04$, (b) $M=0.1$, (c) $M=0.25$	39
Figure 2.9. Velocity streamlines near the hole of the resonator through $y=0$ cross section at different flow velocities. $f=3.15$ kHz, $Va=0.025m/s$. (a) $M=0.04$, (b) $M=0.1$, (c) $M=0.25$	40

Figure 2.10. Velocity streamlines near the orifice of the resonator through $y=0$ cross section at different sound pressure level. $M=0.1$, $f=3.15$ kHz.	41
Figure 2.11. Vorticity field near the orifice through $y=0$ cross section at different sound pressure level. $M=0.1$, $f=3.15$ kHz.	42
Figure 2.12. Normalized resistance of panel 1 at different SPLs predicted by CFD. $M=0.1$, $f=3.15$ kHz.	43
Figure 3.1. Relationship between θ and G for Panel 1. $Va=0.025$ m/s.	52
Figure 3.2. Relationship between θ and G for panel 2 and 3. $Va=0.025$ m/s.	53
Figure 3.3. Normalized acoustic resistance comparisons between proposed formula and experimental data for panel 1. $f=3.15$ kHz, $Va=0.025$ m/s.	55
Figure 3.4. Normalized acoustic resistance comparisons between proposed formula and CFD for panel 1. $ V_a = 0.025$ m / s.	56
Figure 3.5. Normalized acoustic resistance comparisons between proposed formula and CFD for panel 2. $ V_a = 0.025$ m / s.	56
Figure 3.6. Normalized acoustic resistance comparisons between proposed formula and CFD for panel 3. $ V_a = 0.025$ m / s.	57
Figure 3.7. Comparisons between the proposed formula with that of Kirby and Cummings [70] and that of Allam and Abom [75] for panel 1. $f=3.15$ kHz, $Va=0.025$ m/s.	58
Figure 3.8. Normalized acoustic reactance comparisons between Cummings' [77] model and experimental data for panel 1. $f=3.15$ kHz, $Va=0.025$ m/s.	60
Figure 3.9. Sketch of the system.	61

Figure 3.10. Test sample (a) Honeycomb core; (b) assembled honeycomb MPP absorber.	67
Figure 3.11. Sketch of the test setup for derivation of the acoustic impedance of a MPP liner.	69
Figure 3.12. Experimental setup for derivation of the acoustic impedance of a MPP liner.	69
Figure 3.13. Setup for microphone calibrations.....	70
Figure 3.14. Mean flow profiles upstream the liner at different flow velocities.	71
Figure 3.15. Comparisons of the acoustic impedance obtained from the prediction formulae and experiments at different flow velocities.....	74
Figure 4.1. Sketch of a MPP absorber under a grazing flow.....	77
Figure 4.2. Absorption coefficient of a MPP absorber with different flow velocities.	79
Figure 4.3. Absolute value of the difference in the maximum absorption value, resonant frequency and absorption bandwidth between no flow and other grazing flow conditions for different MPP absorbers with $t/d=1$	81
Figure 4.4. Absolute value of the difference in the maximum absorption value, resonant frequency and absorption bandwidth between no flow and other grazing flow conditions for different MPP absorbers with different t/d ratios.	82
Figure 4.5. Resonant frequency of MPP absorbers with different hole diameters.	84
Figure 4.6. Maximum absorption coefficient of MPP absorbers with different hole diameters.	84
Figure 4.7. Bandwidth of MPP absorbers with different hole diameters.....	85

Figure 4.8. Resonant frequency of MPP absorbers with different perforation ratio....	86
Figure 4.9. Maximum absorption coefficient of MPP absorbers with different perforation ratio.	87
Figure 4.10. Bandwidth of MPP absorbers with different perforation ratio.	87
Figure 5.1. Sketch of a simple vibro/acoustic coupled system.	96
Figure 5.2. A 3D rectangular cavity with a vibrating boundary \bar{u}_e	99
Figure 5.3. A rectangular semi-infinite duct with a vibrating boundary \bar{u}_e	102
Figure 5.4. Pressure and velocity description for a MPP.	104
Figure 5.5. Sketch of the investigated flow duct system.	106
Figure 5.6. Sub-system treatment by using PTF approach.	107
Figure 5.7. Sketch of the experimental setup.	113
Figure 5.8. Test sample.	114
Figure 5.9. Comparisons between predictions and the experimental data at $M = 0.035$, (a) TL, (b) sound absorption coefficient.	115
Figure 5.10. Comparisons between prediction and the experimental data at $M = 0.048$, (a) TL, (b) sound absorption coefficient.	116
Figure 5.11. Comparisons between prediction and the experimental data at $M = 0.064$, (a) TL, (b) sound absorption coefficient.	117
Figure 5.12. Silencing performance of MPP silencers without solid partitions under different flow velocities. (a)TL, (b) sound absorption and reflection coefficient.	120
Figure 5.13. Sound pressure distribution inside the MPP silencer without solid	

partitions at $f = 1377$ Hz and $M = 0.05$.	121
Figure 5.14. Silencing performance of honeycomb MPP silencers under different flow velocities. (a) TL, (b) sound absorption coefficient.	124
Figure 5.15. Absolute value of the difference in the TL maximum value, peak frequency and TL bandwidth between $M=0.025$ and other grazing flow velocities for different MPP silencers with $t/d=1$.	125
Figure 5.16. Silencing performance of MPP silencers with different solid partitions. (a) TL, (b) sound absorption coefficient, (c) reflection coefficient.	128
Figure 5.17. (a) TL peak value, (b) TL peak frequency and bandwidth of MPP silencers with different hole diameters.	130
Figure 5.18. TLs of non-partitioned MPP silencers with different hole diameters.	130
Figure 5.19. (a) TL peak value, (b) TL peak frequency and bandwidth of MPP silencers with different perforation ratio.	132
Figure 5.20. Silencing performance of honeycomb MPP silencers with different panel lengths. (a) TL, (b) sound absorption coefficient.	133
Figure 5.21. Sound pressure field of a MPP silencer with a backing cavity containing nine partitions at the peak frequency $f = 863$ Hz and $M = 0.05$.	133
Figure 5.22. TLs of non-partitioned MPP silencers with different panel lengths at $M=0.05$.	135
Figure 5.23. Sound pressure distribution inside a non-partitioned MPP silencer with panel length of 500mm at one peak frequency $f = 1221$ Hz and $M = 0.05$..	136
Figure 6.1. Housing of a range hood (right) and its mock-up (left).	140

Figure 6.2. Sub-structure treatment of the whole system.	141
Figure 6.3. Test sample.	146
Figure 6.4. Sketch of the test set-up.....	147
Figure 6.5. Photo of the experimental setup.	147
Figure 6.6. Comparisons between the predictions and experimental data at $M=0$, (a) TL, (b) sound absorption coefficient, (c) reflection coefficient.....	149
Figure 6.7. Comparisons between the predictions and experimental data at $M = 0.035$, (a) TL, (b) sound absorption coefficient, (c) reflection coefficient.	151
Figure 6.8. Comparisons between the predictions and experimental data at $M = 0.064$, (a) TL, (b) sound absorption coefficient, (c) reflection coefficient.	152
Figure 6.9. TL of the model without MPP.	154
Figure 6.10. Sound absorption and reflection coefficient curves of the model without MPP.....	155
Figure 6.11. Sound pressure field of the model without MPP in the absence of grazing flow, (a) $f = 1169Hz$, (b) $f = 1625Hz$	155
Figure 6.12. TL curves of the range hood model with and without MPP.	156
Figure 6.13. Sound absorption and reflection coefficient curves of the range hood model with MPP.....	158
Figure 6.14. Sound pressure field in the model with MPP at $f = 979Hz$ in the absence of grazing flow.	158
Figure 6.15. TL curves of the range hood model with MPP under different flow velocities.	160

Figure 6.16. Absorption coefficient curves of the range hood model with MPP under different flow velocities.	160
Figure 6.17. TL curves of the range hood model with MPP having different diameters under grazing flow.	162
Figure 6.18. Distribution of the total transmitted power with respect to the diameter of the hole and perforation ratio.	165
Figure 6.19. TL curves of optimization and empty model.....	166
Figure 6.20. Sound absorption and reflection coefficient curves for the first optimization case.	167
Figure 6.21. Sound absorption and reflection coefficient curves for the second optimization case.	168
Figure 6.22. Illustration of coordinate transformation technique.	169
Figure 6.23. Comparison of the TL curve between coordinate transform technique and FEM method, $d = t = 0.5mm$, $\delta = 0.945\%$ and $M = 0$	175
Figure 6.24. TL curves of the range hood model having MPP with the trapezoidal cavity having different inclined angles, $d = t = 0.7mm$, $\delta = 1\%$ and $M = 0.048$...	176
Figure 6.25. TL curves of the range hood model with MPP having different irregular cavity depths, $d = t = 0.7mm$ and $\delta = 1\%$ $M = 0.048$	177
Figure 6.26. Optimized TL curves for case 1, $M = 0.048$	179

List of tables

TABLE 2.1. Geometry parameters of MPPs. Plate 1 is taken from Malmay <i>et al.</i> [55].	23
TABLE 2.2. Computational cases.....	36
TABLE 3.1. Computational cases used to find the relation between G and the acoustic resistance.....	51

Nomenclature

BW	The half absorption bandwidth
c	Speed of sound
d	Hole diameter
D	Cavity depth
e	The half channel height
f	Frequency of acoustic excitation
\bar{f}_e	The mean normal force excitation exerted on the excited patch
f_r	The resonance frequency
f_p	Peak frequency on the transmission loss curve
G	Velocity gradient in viscous sublayer
h	Channel height
$\text{Im}\{ \}$	The imaginary part of the complex number
k_0	The wave number
L	Length of lined part in the duct
L_s	Side length of Helmholtz resonator cavity length
L_x, L_y, L_z	The side lengths of the 3D rectangular cavity
L_x^d, L_z^d	The side lengths of the duct.
L_{mic}	Distance between two microphones
L_{irr}	Thickness of the trapezoidal cavity
M	Mach number

p	Acoustic pressure
\bar{P}_{in}	The space mean acoustic pressure at inlet surface of the hole
\bar{P}_{out}	The space mean acoustic pressure at outlet surface of the hole
Δp	The pressure difference across the hole
$\Delta \bar{p}$	The space mean pressure difference across the hole
r	The radius vector of cylindrical coordinates inside the tube
R	Normalized resistance for no flow condition
R_{flow}	Normalized resistance with grazing flow
R_e	Reynolds number
R_{ef}	Reflection coefficient
$\text{Re}\{ \}$	The real part of the complex number
S	Channel surface area
S_h	The surface area of a single hole
S_s	Occupied surrounding area by a single hole
S_{patch}^{MPP}	The surface area of the segmented patch.
S_{panel}	Panel surface area
TL	The transmission loss
TL_{max}	The maximum value of transmission loss
t	Hole length or panel thickness
u	Velocity of the air particle
u_h	The vibration velocity of the air in the hole
u_p	Vibration velocity of the panel

\bar{u}	The space mean acoustic velocity normal to the hole section
\bar{u}_{cl}	The centerline velocity
\bar{u}_r	The mean normal velocity on the receiving patch
$\langle U \rangle$	Mean stream-wise velocity
U_τ	Friction velocity at the wall
U_∞	Freestream velocity
$ V_a $	Velocity amplitude of the acoustic excitation
W	5dB TL bandwidth
Y_{re}	PTF between patches for vibrating structure
Y_p	The mobility of the MPP plate base
Y_{MPP}	PTF between patches for MPP
z_{fl}	The normal wall distance from the first layer mesh to the wall
Z_{hole}	Normalized acoustic impedance of a single hole
Z_{MPP}	Normalized acoustic impedance of MPPs
Z_{re}	PTF between patches in acoustic domain
Z_s	The normalized surface acoustic impedance of the liner absorber
Π_{in}	Incident sound power
Π_{out}	Transmitted sound power
α	Sound absorption coefficient
α_{max}	Maximum value of sound absorption coefficient
$\alpha_{irr}, \beta_{irr}$	Inclined angle of the tilted wall of trapezoidal cavity
δ	Perforation ratio of the panel

μ	Air dynamic viscosity
τ_w	Shear stress at the wall
ρ	Air density
λ	The Darcy friction factor
λ_w	Acoustic wavelength
ν	Air kinematic viscosity
θ	Changed viscous effects due to the presence of grazing flow
χ	The normalized acoustic reactance without flow
ω	Angular frequency

Chapter 1. Introduction

1.1 Background

Noise has been recognized as one of the major issues, which impacts on people's living quality as well as the competitiveness of products. Nowadays, noise control becomes a necessity and arouses an increasing interest and draws persistent attention of researchers, R&D engineers and practitioners. Typically, noise problem can be tackled from three aspects: noise reduction at the source, noise control in the propagation path and noise shielding at the receiver. Among existing solutions, sound absorption material is commonly used as one of the major means for noise control and mitigation. However, the use of traditional sound absorption materials, such as fibrous and porous materials, would cause numerous problems such as contamination, aging and environment-unfriendliness [1]. These problems can harm the health of people in the long run and jeopardize the practical use of the conventional materials in many applications. Therefore, new and more environmental-friendly materials which can provide efficient and reliable sound absorptions are in great need and of significant practical significance.

A Micro-perforated panel (MPP) is a thin sheet with thickness-through perforations over its surface. With the hole size typically in the sub-millimeter range, a MPP provides a high acoustic resistance (loss) and a low acoustic reactance (mass) by the structure itself. Without the use of any porous material, broadband noise attenuation

could be achieved with a proper design. Meanwhile, MPPs can be manufactured by using fibrous-free, incombustible and cleanable materials. Owing to their unique and environmentally friendly nature, MPPs are being widely used in various noise control applications as an alternative to traditional porous/ fibrous sound absorption materials.

MPPs have been extensively studied and firstly used in simple acoustic environment such as the one in both open and close space with still acoustic media. In many applications, however, MPPs are subjected to flow, especially the grazing flow, in which case flow arrives in the direction which is parallel to the MPP surface. One of the typical examples is mufflers or flow ducts. In the presence of flow, the problem turns out to be much more complicated than its counterpart without flow, and generally speaking, the problem has not been fully understood. Meanwhile, prediction tools, which are necessary to guide the design of MPPs for noise control with flow, are also lacking. Therefore, in the work presented here, the acoustic behavior of MPPs under fully developed turbulent grazing flow conditions within the linear acoustic regime is investigated, and their applications in flow ducts and complex noise control devices are presented.

1.2 Literature review

1.2.1 Conventional sound absorption materials

Sound absorption materials are widely used for acoustic noise control. These materials can absorb the incident sound energy with little reflection. A large variety of

sound absorption materials exist, among which fibrous and porous materials are the most commonly used ones. These materials contain fibers or foam skeletons, forming small cavities or channels, through which sound waves propagate. The acoustic waves then generate the vibration of the air and that of the porous structure, at both the surface of the material and inside the pores. As a result, part of the incident sound energy is converted into heat through thermal and viscous losses at the walls of the interior pores and tunnels within the material [2].

Propagation of sound waves in porous material is determined by two complex parameters: the characteristic impedance and the propagation coefficient. Various models have been developed to obtain these parameters through measurable non-acoustic parameters such as porosity, flow resistance and tortuosity. Through transmission-line analysis on the measured acoustic quantities of a large amount of fibrous materials, Delany and Bazley [3] developed a simple empirical formula based on a single physical parameter: the flow resistance of the material. Owing to its simplicity, this model is widely used to describe the wave propagation in fibrous absorbent materials. To improve the low frequency accuracy of Delany and Bazley equation [3] for some specific porous materials, several slightly different but similar laws [4, 5] were developed. Generally, most of the models were established based on the assumption that the frame of the material is rigid. Although the complete poro-elastic model [6], considering the structural non-rigidity, was developed as well, the accuracy of the simplified models with rigid material frame assumption is deemed

sufficient for most practical cases. The aforementioned models are generally called phenomenological models with the consideration that the porous medium is a globally compressive fluid and the mathematical expressions are simple. However, for porous materials with a complex geometry, these models [3-5] may not be suitable. In light of this, various microstructural models [7-10] were developed to describe acoustic wave propagation through porous materials with arbitrary orientation. The derivation of the characteristic impedance and the propagation coefficient often need more parameters. For instance, five parameters (porosity, flow resistance, tortuosity, and the viscous and thermal pore shape factors) are needed in the model established in [10].

In many practical cases, high-speed flow or large temperature variations exist, like in the case of exhaust pipes of engines. These circumstances are hostile to the use of classical porous materials which can be easily damaged. As a common practice, perforated panels are usually used to shield and protect the porous materials. In these cases, porous materials are enclosed by perforated panels with a hole size typically in the range of millimeter. With a hole size in such a large scale, as opposed to the so-called micro-perforated panels to be investigated in this thesis, the panels themselves can hardly provide any meaningful sound absorption without porous components [11-17].

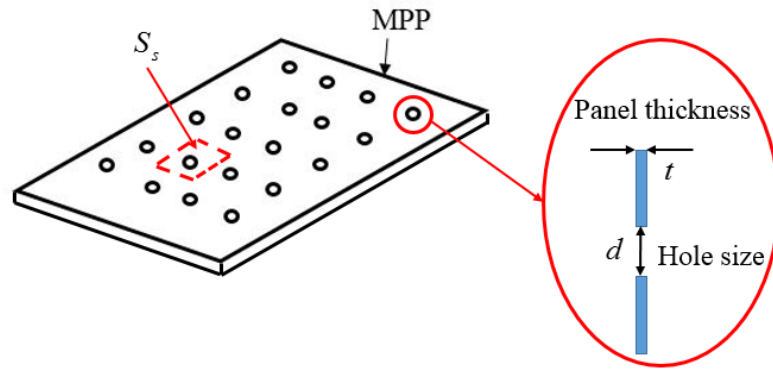
Although widely used, porous absorption materials can cause numerous problems. For example, they can accumulate dust and oil and can be easily damaged. In the long

run, the bacterial contamination can also be generated, which is harmful to public health which hampers their use in some more rigorous conditions like in hospitals, food and pharmaceutical industries. As the concerns of public health increase, more effective, robust and environmental-friendly sound absorption materials are needed.

1.2.2 Micro-perforated panels and Crandall's theory on acoustic propagation in a single tube

As an alternative to traditional porous sound absorbing materials, Micro-perforated Panels (MPPs) have been drawing persistent attention. A MPP is a thin panel with perforated holes over its surface. The typical structure of a MPP is shown in Fig.1.1. The size of the holes is typically in the sub-millimeter range. The holes are separated by a distance which is much larger than the hole size, but usually smaller than the wavelength of the impinging acoustic wave. Considering the perforated holes are uniformly distributed, each hole then has the same surrounding area S_s as shown in Fig. 1.1a. The perforation ratio δ is defined as the ratio between the surface area of a single hole S_h and that of its surrounding area. The perforation ratio of MPPs is usually around 1%. With the hole size in the sub-millimeter range, the small hole ensures a small oscillating mass in the hole and an effective viscous dissipation in the shear layer of the hole. Thus, MPPs can provide a high acoustic resistance (loss) and a sufficiently low acoustic reactance (mass) by the structure itself, conducive to effective sound absorption with a proper design. More importantly, by using MPPs alone,

broadband noise attenuations can be achieved without the use of any porous materials.



(a)



(b)

Figure 1.1. A Micro-perforated panel.

The acoustic behavior of a MPP is usually characterized by its surface impedance. The development of the MPP impedance prediction tools originates from the sound propagation in a tube as proposed by Rayleigh [18]. Crandall [19] then simplified the model into a finite short tube, which was considered by him as a single hole in a perforated panel. Due to the viscous retardation near the wall of the hole, the fluid in the hole was treated as a collection of shear layers. By considering an angular ring of

fluid as the control volume, shown in Fig. 1.2, and applying the fundamental physical principles, the governing equation of motion of the fluid in the hole can be obtained.

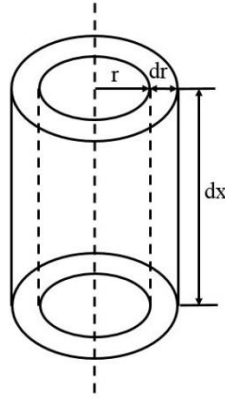


Figure 1.2. Schematic drawing of an angular ring of fluid.

Taking the axis of the hole as x , the total driving force on the angular ring, at a radius r , can be written as $\frac{\partial p}{\partial x} 2\pi r dr dx$. This is balanced by the inertial force

$\rho \frac{\partial u}{\partial t} 2\pi r dr dx$ and the net viscous resistive force $\mu \frac{\partial}{\partial r} \left(\frac{\partial u}{\partial r} r \right) 2\pi dr dx$, which is

proportional to the gradient of the flow velocity and the contact area between the layers.

Therefore, the equation of motion can be written as:

$$\frac{\mu}{r} \frac{\partial}{\partial r} \left(\frac{\partial u}{\partial r} r - \rho \dot{u} \right) = - \frac{\partial p}{\partial x}, \quad (1.1)$$

where u is the velocity of the air particle; ρ the density of air; μ the air dynamic viscosity and r the radius vector of cylindrical coordinates inside the tube.

When the length of the tube or that of the hole (thickness of the panel) is much smaller than an acoustic wavelength, the pressure gradient $\frac{\partial p}{\partial x}$ can be approximated by the ratio between the pressure difference across the two ends of the hole Δp and the hole length t , Eq. 1.1 can then be written as:

$$\frac{\mu}{r} \frac{\partial}{\partial r} \left(\frac{\partial u}{\partial r} r - \rho \dot{u} \right) = -\frac{\Delta p}{t}. \quad (1.2)$$

In a harmonic regime, Eq. 1.2 becomes:

$$j\omega\rho u - \frac{\mu}{r} \frac{\partial}{\partial r} \left(\frac{\partial u}{\partial r} r \right) = \frac{\Delta p}{t}, \quad (1.3)$$

where ω is the angular frequency.

By solving Eq. 1.3 and defining the acoustic impedance of a short tube or a hole as the ratio between the space average pressure difference across the hole $\Delta \bar{p}$ over the space average velocity normal to the hole section \bar{u} , one has

$$Z_i = \frac{\Delta \bar{p}}{\bar{u}} = j\omega\rho t \left[1 - \frac{2}{K\sqrt{-j}} \frac{J_1(K\sqrt{-j})}{J_0(K\sqrt{-j})} \right]^{-1}, \quad (1.4)$$

where $K = \frac{d}{2} \sqrt{\rho\omega / \mu}$ is a parameter describing the ratio of the radius to the viscous boundary layer thickness inside the hole; d the hole diameter; J_1 and J_0 the Bessel functions of the first kind and first and zero order respectively. As the calculation of the Bessel function is difficult, historically, Eq. 1.4 has not been directly used to obtain the impedance of a hole. Instead, for $K < 1$ and $K > 10$, the formulae developed by Crandall [19] are used to get the approximate values of Z_i .

1.2.3 Impedance model of Micro-perforated panels without flow

In Eq. 1.4, K lies between 1 and 10 for MPPs. The approximation values are obtained by Maa [20], written as:

$$Z_i = \frac{32\mu t}{d^2} \sqrt{1 + \frac{K^2}{32}} + j\omega\rho t \left(1 + \frac{1}{\sqrt{9 + \frac{K^2}{2}}} \right). \quad (1.5)$$

Note that, only the air in the hole is considered in Eq. 1.4 or 1.5 without considering the end correction effects. However, for small holes, the hole diameter and the hole length are small compared to an acoustic wavelength. Under the incident acoustic excitation, the oscillating fluid would be more than that contained in the hole due to the mass inertia and the viscous effects. Therefore, for the case of small holes or tubes of finite length, an additional term must be added to Eq. 1.4 or 1.5. This additional term is called the end correction term.

The end correction effects of small holes were investigated experimentally and theoretically by Sivian [21] and Ingard [22]. The end correction for the resistance term accounts for viscous effects outside the hole at its both ends. The end correction for the reactance term accounts for the oscillation of the additional mass. After introducing the end corrections as suggested by Ingard [22], the normalized specific acoustic impedance (normalized by ρc with c being the speed of sound) of a hole for all ranges of K is proposed by Maa [20, 23] and expressed as:

$$Z_{hole} = \frac{32\mu t}{\rho c d^2} \left[\left(1 + \frac{K^2}{32} \right)^{\frac{1}{2}} + \frac{\sqrt{2}}{32} K \frac{d}{t} \right] + j \frac{\omega t}{c} \left[1 + \left(9 + \frac{K^2}{32} \right)^{-1/2} + 0.85 \frac{d}{t} \right]. \quad (1.6)$$

With the assumption that no interactions between the holes takes place, the acoustic impedance prediction formula of a Micro-perforated panel is established by Maa [20, 23] by dividing the acoustic impedance of a single hole (Eq. 1.6) by the perforation ratio of the panel δ , expressed as:

$$Z_{MPP} = R + j\chi, \quad (1.7a)$$

$$R = R_{in} + R_{out} = \frac{32\mu t}{\delta \rho c d^2} \left[\left(1 + \frac{K^2}{32} \right)^{\frac{1}{2}} + \frac{\sqrt{2}}{32} K \frac{d}{t} \right], \quad (1.7b)$$

$$\chi = \frac{\omega t}{\delta c} \left[1 + \left(9 + \frac{K^2}{32} \right)^{-1/2} + 0.85 \frac{d}{t} \right]. \quad (1.7c)$$

The real part R is called the acoustic resistance which is associated with the acoustic energy dissipation due to viscous effects. The first term R_{in} represents the viscous effects in the hole and the second one R_{out} describes the viscous effects outside the hole (end correction). The imaginary part χ is referred to as the acoustic reactance, which is the inertial in nature. It should be noted that Eq. 1.7 only applies to MPPs without flow under a low acoustic excitation.

1.2.4 Works on MPP without flow

Since then, research on MPPs has been flourishing and intensifying, as evidenced by the large amount of papers published on the topics, ranging from studies on the acoustic behavior of MPPs under different conditions to the exploration of their applications. Typically, a MPP is backed by a cavity to form a MPP absorber. The air gap between the panel and the backing cavity together with the micro holes produce the so-called Helmholtz effects to ensure effective sound absorptions. Except for the conventional cases, in which the depth of the backing cavity is constant and under normal incident acoustic excitation, MPPs backed by an irregular-shaped cavity [24-27] or under oblique sound incidence [28-33] have also been investigated. It was found that the sound absorption of MPP absorbers can be improved with an irregular-shaped backing cavity due to the fact that more complex acoustical modes in the backing cavity can be activated and are coupled with the MPP, leading to a stronger coupling between the MPP and the cavity. For MPPs under oblique sound incidence [28-33], it was

revealed that, with the backing cavity being partitioned, the locations of the absorption peaks were roughly insensitive to the variation of the incidence angle. However, for the non-partitioned backing cavity, increasing the incidence angle results in an increase in the frequency of the main absorption peaks and the appearance of additional absorption peaks. To improve the acoustic performance of a MPP absorber, many studies have been conducted, such as introducing suitable partitions in the backing cavity [34-37], utilizing multi-layer MPPs [38-42] and parallel arrangement of multiple MPPs [43-45] etc. These works indicate that, by employing extra MPPs, the acoustic resistance increases while the acoustic reactance decreases, which gives rise to a widened absorption bandwidth in a lower frequency range. Of course, when more MPPs are used, the total number of control parameters affecting the absorption performance also increases and the optimal design of systems with more MPPs becomes more challenging.

As a clean and efficient sound absorbing material, MPP absorbers have been widely used in many applications, such as construction equipment, building interiors, HVAC ducts and mufflers etc. Conventionally, MPPs found their early use in architectural and environmental acoustic problems. For example, the applications of MPPs on building ventilation window systems were investigated by Kang and Brocklesby [46] experimentally and Kang and Li numerically [47]. Asdrubali and Pispola [29] proposed a noise barrier using transparent polycarbonate MPPs. These works indicate that better noise insulation of the systems could be achieved by using MPPs. More recently, MPP

applications in compact mechanical systems start to draw more attention of the scientific community due to the increasing complexity of the problem related to system coupling. For example, Corin and Weste [48] utilized MPPs in an engine enclosure as an acoustical heat shield. Li and Mechefske [49] reported the utilization of MPP absorbers to reduce the noise of a magnetic resonance imaging (MRI) equipment. Yu *et al* investigated the application of MPPs in expansion chamber silencers [34] and ventilation systems in buildings [50]. It was shown that, being strongly affected by the surrounding acoustic environment, the acoustic behavior of MPPs is very different from the laboratory impedance tube condition. Results point at the need of considering MPPs as an integral part of the entire acoustic/vibro-acoustic system, which calls for the development of efficient modelling, analysis and optimization tools [51-53].

1.2.5 MPPs with grazing flow

Apart from the work on MPP sound absorptions in still acoustic media, another important category of problems involves flow to which MPPs are exposed, among which the case of the grazing flow is the most representative and practically important. Typical examples include cases such as vehicle exhaust silencers, attenuators in air-moving ducts, duct linings in jet engines or numerous domestic products.

Existing work relating to the flow passing through a perforated hole in a plate has been arousing wide interest of the scientific community. As reported in many works [54-56], above a certain flow velocity, the resistance of the acoustic impedance

increases with the flow velocity while the reactance decreases. To understand the mechanisms behind these changes in the impedance, flow visualizations near the mouth of a hole were carried out [57-60]. These works revealed that, under an acoustic excitation, fluid would flow into and then out of the cavity through the hole during one cycle of oscillation. Meanwhile, vortices are generated from the leading edge of the orifice under the acoustic excitation and are convected downstream by the mean grazing flow. When inflow and outflow occur, the effective area for the fluid passage is smaller than the area of the hole and the discharge coefficient (the ratio between the core inflow/outflow area and the hole area) is used to describe this phenomenon. In addition, the shear layer above the orifice would move up within one oscillation cycle. Based on these observations, the sound energy dissipation mechanism was interpreted in different ways by different researchers. For example, in many works [61-64], the grazing flow effects were simply described as a “blowing away” of the oscillation fluid across the hole and the stored kinetic energy. Also many researchers [58, 65] believed that the movement of the shear layer above the hole contributes to the acoustic sound energy dissipation. While the research [54, 55, 66, 67] showed that the amount of sound energy consumed is related to that of fluid flowing into and out of the cavity through the hole and thus is related to the value of the discharge coefficient, the acoustically induced vortex shedding was used to describe the grazing flow effects in many works [56, 68].

To predict the acoustic properties of the perforated holes in the presence of grazing flow, theoretical [56, 64, 65, 68, 69] or semi-theoretical models [54, 58] were developed

upon making different simplifications on the interactions between the acoustic waves and the flow field near the perforated holes based on different interpreted sound energy dissipation mechanisms. For example, Rice [69] modeled the acoustic excitation imposed on the grazing flow as a spherically symmetrical perturbation. Ronneberger [64] simplified the problem as wavelike disturbances of a thin shear layer over the orifice. Howe *et al.* [68] and Jing *et al.* [56] established their respective models based on the vortex shedding from the upstream lip of an orifice. Walker and Charwat [65] proposed a hinged-lid model according to the motion of the shear layer above the orifice caused by the inflow and outflow of the fluid. Hersh and Walker [54] and Rogers and Hersh [58] proposed their semi-empirical acoustic prediction models based on the discharge coefficient to which the grazing flow effects were attributed. In both works, the discharge coefficients were determined experimentally. While shedding light on the underlying physics, most of these theoretical or semi-theoretical models only consider inviscid flow for a hole size which is beyond the micro-perforated range. Meanwhile, due to the problem simplification, the predicted acoustic impedance only qualitatively agree with experimental data [70].

A continuous effort is to develop empirical models for the acoustic impedance prediction [70-79]. Through experimental data analyses, efforts were made to establish the flow parameters which can be intrinsically linked to the acoustic impedance of the MPP hole and that of the perforated panels. Various empirical models were proposed based on these flow parameters. Early attempts used the flow speed [71] or Mach

number [72-75] to characterize the grazing flow effects. These empirical models involve the assignment of some coefficient values in the proposed formula. It is noticed, however, that the problem is too complicated to be characterized only by a basic flow parameter such as Mach number [72-75]. Thus, many other studies then focused on exploiting other flow parameters which hopefully can better characterize the grazing flow effects. For example, Goldman and Chung [80] reported the effects of a stream-wise pressure gradient in the boundary layer on the hole impedance. Goldman and Panton [81] investigated a series of parameters and finally adopted the use of the friction velocity, which later on led to the proposal of the acoustic impedance prediction models [70, 76-78]. Despite the efforts made, the search for pertinent flow parameters which can determine the acoustic impedance of the MPPs is still of actuality. Most importantly, different prediction models are shown to give very different results even using the same flow parameter [70]. Nevertheless, these studies indicate the necessity of including some boundary layer parameters to characterize the grazing flow effects. When the boundary layer is thick compared to the orifice diameter, the inner boundary layer parameters need to be included as suggested by Cummings [77].

Most of the aforementioned studies considered perforations with a hole diameter typically around 1 mm or larger. This, in a strict sense, falls beyond the scope of the micro-perforation in the perspective of achieving sound absorption. Among the most relevant works, one may cite Allam and Abom [75] who proposed an set of impedance formulae based on the flow Mach number and the experimental work of Malmay *et al*

[55].

With the fast development of the computational capability, numerical methods such as DNS, LES and RANS are more frequently used to investigate these problems [66, 82-87]. Powerful numerical means allow scrutinizing the flow field around the MPP hole with much more details, thus warranting a better understanding of the sound energy dissipation mechanism and a more accurate description of the acoustic properties of the perforated holes in the presence of flow. For example, DNS was applied to a single Helmholtz resonator to understand its sound energy dissipation mechanism [82-84]. Results indicated a transition from the viscous-dominant dissipation in the shear layer near the hole to the chaotic vortex shedding dominant dissipation with increasing sound pressure level. It was shown that [85-87], without using the highly computationally costly methods like DNS or LES, more cost-effective tools like 3D URANS CFD could reasonably predict the acoustic behavior of the Helmholtz resonator [85] and that of the perforated panel silencers [86] in both no-flow and flow conditions.

1.3 Motivations and thesis layout

Existing work allowed a qualitative description of the acoustic behavior of MPPs in the presence of a grazing flow. The case with flow turns out to be much more complicated than its counterpart without flow. Different flow patterns could be seen near the orifice when configurations change, such as orifices with different dimensions,

sound pressure levels of the acoustic excitation, the flow velocity and its evolution. Despite the considerable progress made during the past decades, on the exploration and understanding of the interactions between the acoustic excitation and the grazing flow, there are still much unknowns, which are summarized as follows:

- 1) The sound energy dissipation mechanisms have been interpreted in many diverse or even contradictory ways, which up to now is still not fully understood.
- 2) Different from the no-flow condition, a universally accepted and consistent acoustic impedance formula to guide the practical design of MPPs in the presence of flow is still lacking.
- 3) The intrinsic flow parameters which can characterize the inherent grazing flow effects on the acoustic impedance of MPPs still need to be found.
- 4) Due to the aforementioned problems, research works pertinent to the applications of MPPs with grazing flow are fairly limited [35, 88, 89]. Consequently, the influences of parameters, such as flow velocities, panel dimensions, perforation ratios and hole diameters on the sound absorption of MPP absorbers are not clear when a flow is present.

- 5) With the increasing complexity due to the presence of the flow and the intimate interaction between the MPPs with the surrounding acoustic media, suitable modelling tools need to be developed. Among the required attributes are the efficiency, flexibility and versatility of the modelling method to cope with the need for system analyses and optimization.

Motivated by this, the present work investigates the acoustic behavior of MPPs under fully developed turbulent grazing flow conditions within the linear acoustic regime. Main focuses are put on four aspects.

- 1). The flow field around the holes of a MPP and the sound energy dissipation mechanism are scrutinized and investigated.

- 2). A new flow parameter which intrinsically relates the grazing flow effects with the acoustic impedance of the MPP is identified.

- 3). A new impedance prediction formula is proposed to supplement the one by Maa in the no-flow condition [23].

- 4). The applications of MPPs in complex acoustic environment with grazing flow are investigated to provide practical guidance for a few typical applications.

More specifically, in Chapter 2, numerical studies are carried out through 3D URANS CFD simulations. Computed results are then presented for validating the CFD model, analyzing flow field near the hole, exploring sound energy dissipation mechanism and identifying the new intrinsic flow parameter. Based on this, a new flow parameter, alongside a complete set of impedance prediction formula for MPPs with grazing flow, is established through numerical experiments in Chapter 3. Prediction results from the proposed formula are then compared with those from other existing formulae or experimentally measured data to show the accuracy and the improvement that the new impedance formula brings about. In Chapter 4, sound absorption properties of MPP absorbers in a relatively ideal and simple acoustic environment are investigated in terms of sound absorption coefficient by using the established impedance prediction formula. To cope with the need of modelling, analyzing and optimizing MPPs in a fully coupled acoustic system, a sub-structuring technique is then presented in Chapter 5. To provide practical guidance for the design of MPPs in complex acoustic environment with grazing flow, applications of MPPs in flow ducts and in a more complex noise control devices with grazing flow are investigated in Chapters 5 and 6, respectively. Concluding remarks along with future suggestions are finally given in Chapter 7.

Chapter 2. CFD Simulations and Energy Dissipation

Mechanism

In this chapter, numerical studies are carried out to investigate the flow field near the aperture of the MPP holes by solving the compressible three-dimensional (3D) unsteady Reynolds averaged Navier-Stokes equations (URANS). The finite volume based commercial CFD software FLUENT is used as the computational tool. The choice of the simulation tool is justified by the observations made in previous work on acoustic attenuators [85-87]. A single unit cell composed of a micro-perforated hole with a backing cavity, previously studied by Malmary *et al.* [55], is investigated. Computed results are then compared to the experiments to verify the accuracy of the CFD model. Studies on the flow field around the hole under different flow speeds and acoustic forcing are presented, which allow the exploration of the sound energy dissipation mechanism and the identification of a new flow parameter which is shown to be well correlated to the acoustic impedance in the next chapter.

2.1. Computational model and simulation method

2.1.1. Model

Consider a MPP panel with a honeycomb backing cavity as shown in Fig. 2.1. Each hole in the face plate and the cavity cell behind it form a Helmholtz resonator. The entire honeycomb MPP absorber can be regarded as an assembly of an array of

Helmholtz resonators. We assume a low perforation ratio (typically around 1%) so that each resonator would act independently and the interaction between the holes are therefore neglected. Under this condition, the acoustic impedance of the panel is equal to that of a single isolated MPP hole divided by the perforation ratio. The computational model will use a single Helmholtz resonator, shown in Fig. 2.1.

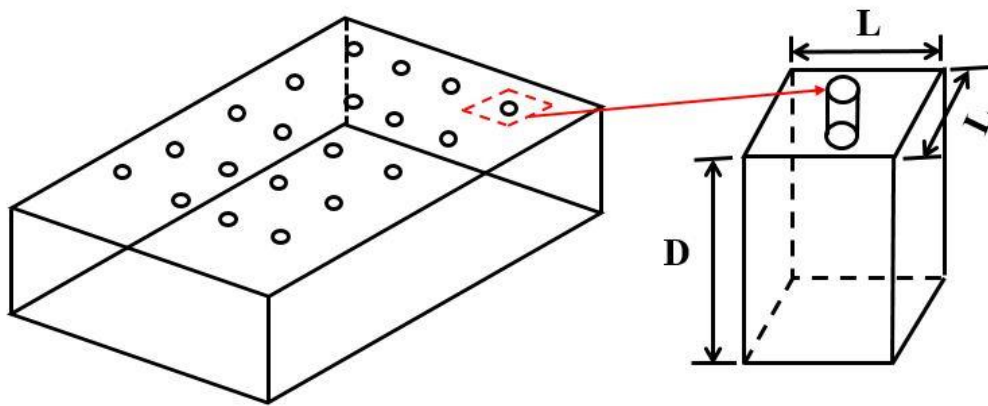


Figure 2.1. Perforated panel (left) modeled by a single Helmholtz resonator (right).

Geometrical parameters of the MPPs being investigated hereafter are listed in Table 2.1. All panels, to be used for simulations and comparisons, both numerically and experimentally, are typical Micro-perforated panels (with hole diameters smaller than 1mm). Note that, Panel 1, with cylindrical holes of a diameter $d = 0.68$ mm, is the configuration used by Malmay *et al.* [55]. All panels have the same size of 24 x 24mm, with a 10 mm deep backing cavity, same as [55]. The side length of each MPP cell, L_s , is determined based on the perforation ratio.

TABLE 2.1. Geometry parameters of MPPs. Plate 1 is taken from Malmary *et al.* [55].

Panel Number	Orifice diameter d (mm)	Panel thickness t (mm)	t/d	Perforation ratio δ
1	0.68	1.02	1.7	1.39%
2	0.5	1.02	2.04	1.39%
3	0.3	0.3	1	1.39%

The modelled system is shown in Fig. 2.2 (two-dimensional view). A MPP cell is flush-mounted on one sidewall of a square duct with a cross section of 24 x 24mm. The upstream portion of the duct is 1000mm long, which allows the flow to be fully developed. The downstream portion contains at least two acoustic wavelengths corresponding to the highest frequency of interest as suggested by [90].

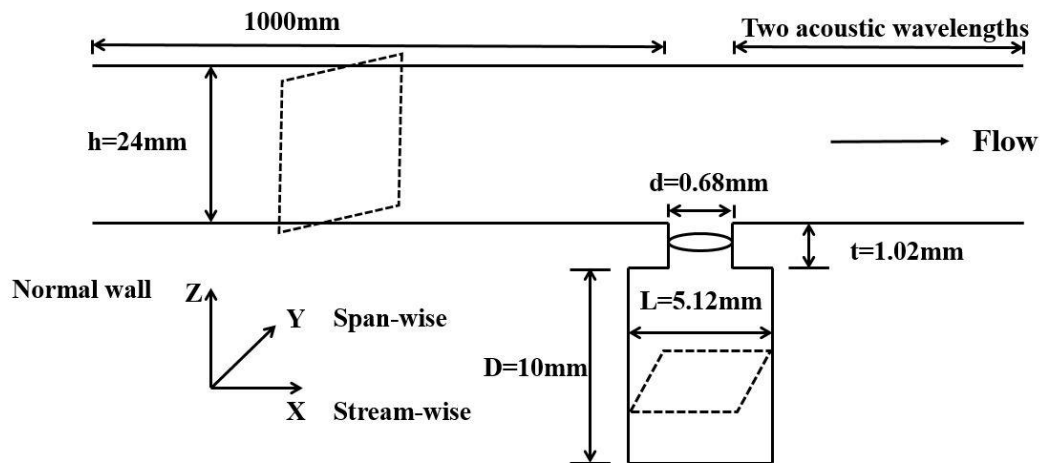


Figure 2.2. System model.

The computational domain is discretized by multi-size grids, by using structured and unstructured meshes for the duct and the backing cavity, respectively. Denser meshes are used in the region near the orifice and the wall of the duct. Away from these regions, the mesh size increases gradually. To ensure an accurate description of the flow field near the wall, the mesh size of the first layer adjacent to the duct wall was designed to ensure that $y^+ = z_{fl} U_\tau / \nu \leq 1$, in which U_τ is the friction velocity, z_{fl} is the distance from the first layer mesh to the wall in the normal wall direction and ν is the kinematic viscosity of the air.

Inside the hole, the average size of the elements is 0.015 mm. In the duct, the grid spacing in the stream-wise direction ranges from 0.015 to 1.6 mm upstream the resonator and from 0.015 to 2.4 mm downstream, which results in a minimum of about 65 and 43 grids per acoustic wavelength upstream and downstream the resonator respectively at the highest frequency considered in the study. The grid spacing in the normal wall and span-wise direction ranges from 0.0075 to 1mm and from 0.015 to 0.8mm respectively. This results in a total of about 3,000,000 elements. The convergence of the solution in relation to the meshing is conducted through investigating the time-domain variation of the acoustic pressure and that of the velocity at the hole inlet section, which are used to calculate the acoustic impedance of the hole. The original mesh contains about 1,800,000 nodes, while the refined mesh includes over 2,400,000 nodes, with most of the additional points located within the area near the hole. The time step is also reduced from 5e-6s in stable grazing flow and 5e-7s for

acoustic simulation to $2.5e-6$ s and $2.5e-7$ s, respectively. Calculations results are plotted and compared in Fig. 2.3. The comparison indicates that there are only minor differences between the two cases and the results converge to the accuracy needed for impedance prediction.

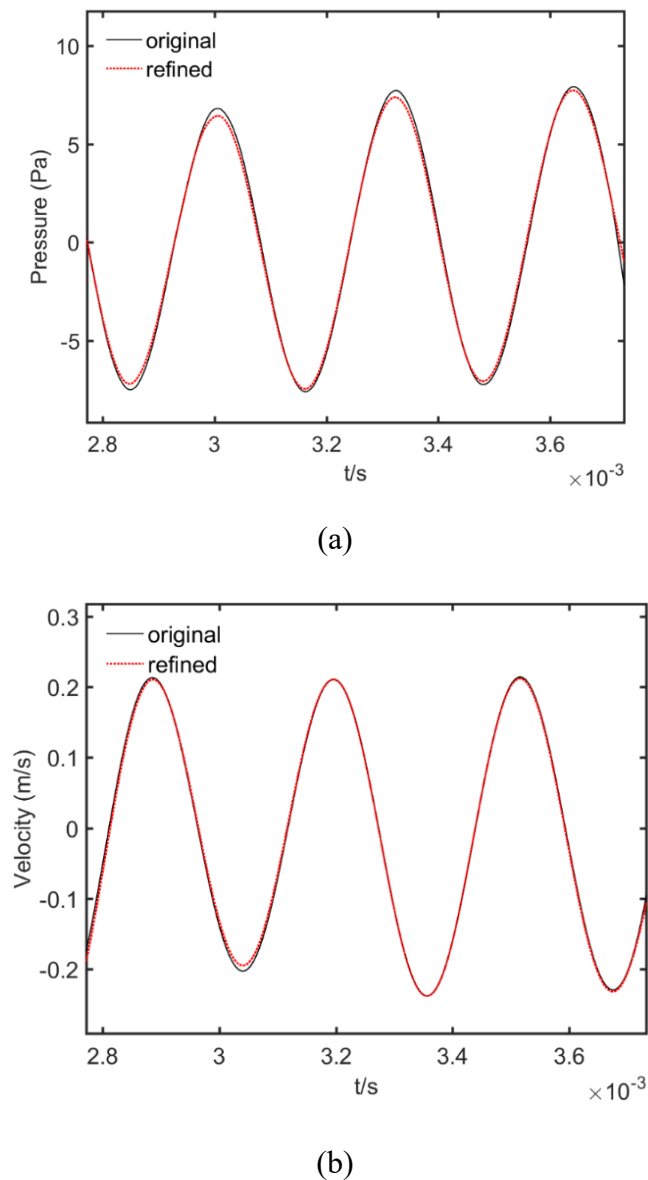


Figure 2.3. Acoustic pressure (a) and the corresponding normal velocity (b) at the hole

inlet section. $M=0.2$, 3.15 kHz, $|V_a| = 0.025$ m / s .

2.1.2. Computational method

The 3D URANS is adopted using the commercial CFD code, FLUENT. The equations of URANS are derived from instantaneous Navier-Stokes equations by separating the flow variables into the mean component and the fluctuating component. These equations allow for solutions to the mean flow field of the turbulent flow by time averaging the flow quantities. The number of the unknowns in the equations of URANS is more than that of the equations. These equations are unclosed. The Realizable k - ϵ turbulence model is adopted for this closure problem. Enhanced wall treatment is adopted for near wall treatment so that the near wall flow field until viscous sublayer region can be resolved and reasonably captured but not modelled. The mass flow rate boundary condition is applied to the inlet of the duct, which can be calculated as $m = U_{\infty} \rho S$, where U_{∞} is the free-stream grazing flow velocity and S the cross section surface area of the channel. The pressure at the outlet is set to be the atmospheric pressure. Solid wall boundary conditions with no slip are imposed to all wall surfaces. A pressure-based implicit solver is employed. The pressure-velocity coupling scheme PISO (Pressure-Implicit with Splitting of Operators) algorithm is applied for both the stable mean flow field and the aero-acoustic coupling simulation. The second order scheme is chosen for both the spatial discretization and time integration. We consider the situation in which the MPPs are exposed to a constant room temperature in this work. Notwithstanding of above, this effect can be easily investigated through the established CFD model by changing the values of the initial temperature of the entire simulation domain. In the current work, the temperature and the ambient pressure of

the entire simulation domain are always initially set at $T = 293K$ and $p = 101kPa$.

A two-step approach is used to deal with the interaction between the flow and the acoustic wave near the hole. The stable mean flow field is first computed. Harmonic acoustic wave with a given velocity amplitude $|V_a|$ is then added as the acoustic excitation $|V_a|\sin(2\pi ft)$, where f is the acoustic excitation frequency. The stable mean grazing flow is calculated by running the unsteady solver until flow properties stop changing. The time step size for the stable mean flow computation is $5e-6s$. That used in acoustic simulations is $5e-7s$.

More details on the model setting and calculation are listed as follows:

- In the General window, the pressure-based and transient time options are selected for the type of solver with the gravity effect for air being omitted.
- In the Models window, the energy equation is selected to be solved. For the viscous model Realizable $k-\varepsilon$ model is selected, and Enhanced wall treatment is selected for near-wall treatment. The model constants are set as default values.
- In the Material window, ideal-gas option is selected for the density of air, the default values are selected for other properties of air, such as specific heat,

thermal conductivity, viscosity and molecular weight.

- In the Boundary Conditions window, mass-flow-inlet and pressure-outlet are selected for the types of inlet and outlet conditions of the duct, respectively. In the Mass-Flow Inlet window, for Momentum, Mass Flow Rate is selected as the Mass Flow Specification Method. Without acoustic excitation, its value is $m = U_{\infty} \rho S$, otherwise $m = U_{\infty} \rho S + |V_a| \sin(2\pi ft)$. Initial Gauge Pressure is set as zero. The x-Component of Flow Direction is set to be 1, while the ones in y and z directions are both set to be zero. Non-Reflecting Boundary is not employed in the current study. The k and Epsilon option is selected for Specification Method for turbulence, the Turbulent Kinetic Energy and Turbulent Dissipation Rate are set to be 1, the default values. The Total Temperature in the Thermal window is set as 293k. In the Pressure Outlet window, for Momentum, the Gauge Pressure is set to be zero. The option Normal to Boundary is selected as Backflow Direction Specification Method. The settings of Specification Method, Backflow Turbulent Kinetic Energy and Backflow Turbulent Dissipation Rate for Turbulence are the same as those in Mass-Flow Inlet window. The Radial Equilibrium Pressure Distribution, Average Pressure Specification, Target Mass Flow Rate and Non-Reflecting Boundary are not employed. The Backflow Total Temperature in the Thermal window is set as 293k. In the Wall window, the Stationary Wall and No Slip options are selected for Wall Motion and Shear Condition, respectively. The

setting in the Thermal window are set as default.

- In the Solution Methods window, PISO is selected as the Pressure-Velocity Coupling Scheme. Skewness-Neighbor Coupling is selected with both Skewness Correction and Neighbor Correction being one. Green-Gauss Cell Based option is chosen for Gradient, and the Second Order or Second Order Upwind scheme is selected for the spatial discretization of Pressure, Density, Momentum, Turbulent Kinetic Energy, Turbulent Dissipation Rate and Energy. The Second Order Implicit scheme is selected for Transient Formulation. The options like Non-Iterative Time Advancement, Frozen Flux Formulation and High Order Term Relaxation are not selected.
- The values of Under-Relaxation Factors in Solution Controls window are all set as default values.
- In the Monitors window, 0.001 is chosen as the residuals for the continuity equation, the velocities, the energy equation, k and epsilon.
- In the Solution Initialization window, the Standard Initialization is selected as the Initialization Methods. The Reference Frame is selected to be Relative to Cell Zone. After clicking Initialize, the Initial Values for Gauge Pressure, velocities, Turbulent Kinetic Energy, Turbulent Dissipation Rate and

Temperature can be obtained based on the above settings.

- In the Run Calculation window, at the beginning of the calculation, a small value, like $5e-08s$, is assigned as the Time Step Size and a larger value, like 30 is assigned to Max Iterations/Time Step to overcome the convergence difficulties. After the calculated results start to stabilize, the Time Step Size is changed to be $5e-6s$ for stable flow field simulation and $5e-7s$ for acoustic simulation and the number of Max Iterations/Time Step is adjusted to be 20 for both cases.

2.2. Validation of the CFD model

The viscous sub-layer region which is adjacent to the flow field in the hole plays a key role in determining the acoustic impedance of the hole. The velocity gradient in this layer and the friction velocity are important parameters in this near-wall region. They are first investigated to ensure a truthful description of the physical phenomena by the CFD model.

2.2.1. Mean stream-wise velocity

To check the quality of the flow simulation, the mean stream-wise velocity profiles at two upstream locations at $M=0.25$ are shown in Fig. 2.4. The origin of the coordinates

is set at the center of the inlet surface of the MPP cell. The same flow velocity profiles observed for these two upstream positions demonstrate that the flow is fully developed before reaching the MPP cell.

The corresponding semi-log plots of the mean stream-wise velocity at $x = -50\text{mm}$ is shown in Fig. 2.5, along with the well-known logarithmic law [91]. In the figure, $U^+ = \langle U \rangle / U_\tau$, with $\langle U \rangle$ being the mean stream-wise velocity. It can be seen that the predicted data agree well with the empirical equation [91], including the viscous sublayer region ($y^+ \leq 5$) where the CFD data follow quite well with the well-known trend $U^+ = y^+$.

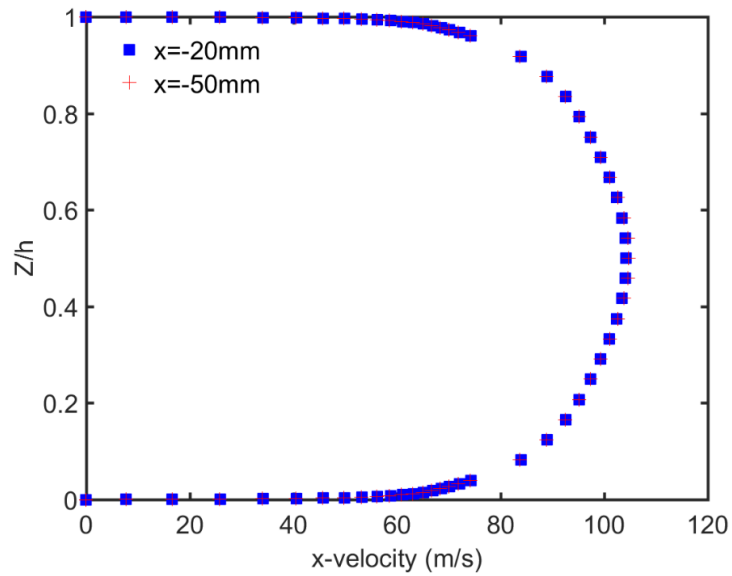


Figure 2.4. Mean x-velocity profiles at different locations upstream the resonator, through the $y=0$ cross section. $M=0.25$.

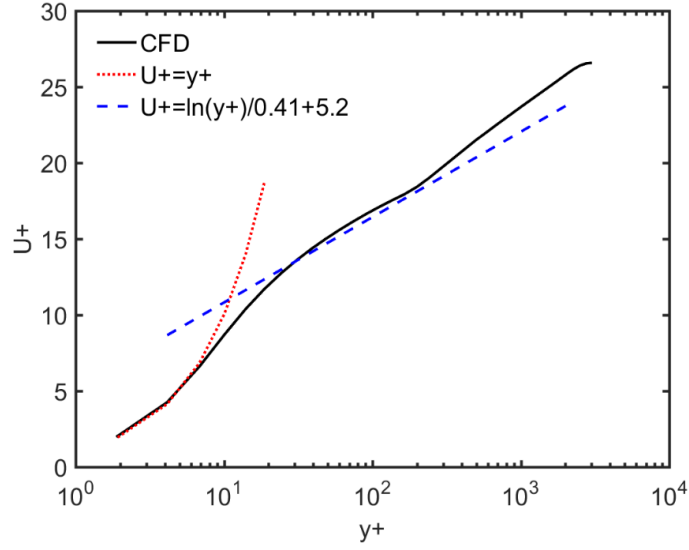


Figure 2.5. Semi-log plots of the mean stream-wise velocity profile upstream the resonator at $x = -50mm$, through $y=0$ cross section. $M=0.25$.

2.2.2. Friction velocity

As to be demonstrated later, the acoustic impedance of the MPPs under grazing flow is well correlated to the velocity gradient in the viscous sublayer over the duct wall, G , defined as

$$G = \frac{U_\tau^2}{\nu}, \quad (2.1)$$

with the friction velocity, U_τ , calculated by

$$U_\tau = \sqrt{\frac{\tau_w}{\rho}}, \quad (2.2)$$

where τ_w is the wall shear stress, which can be determined from the free-stream grazing flow velocity U_∞ and the Darcy friction factor as

$$\tau_w = \frac{\rho U_\infty^2 \lambda}{8}, \quad (2.3)$$

The expression developed by Fujita [92] is used to calculate λ whose accuracy is shown to be within engineering accuracy [70]:

$$\lambda = \frac{0.178}{R_e^{1/5}}, \quad (2.4)$$

where $R_e = \frac{hU_\infty}{\nu}$ is the Reynolds number with h being the height of the square duct.

The numerically calculated friction velocity is compared with the prediction by the empirical equation [92] in Fig. 2.6. The agreement between the two sets of results demonstrates the validity of the computational model.

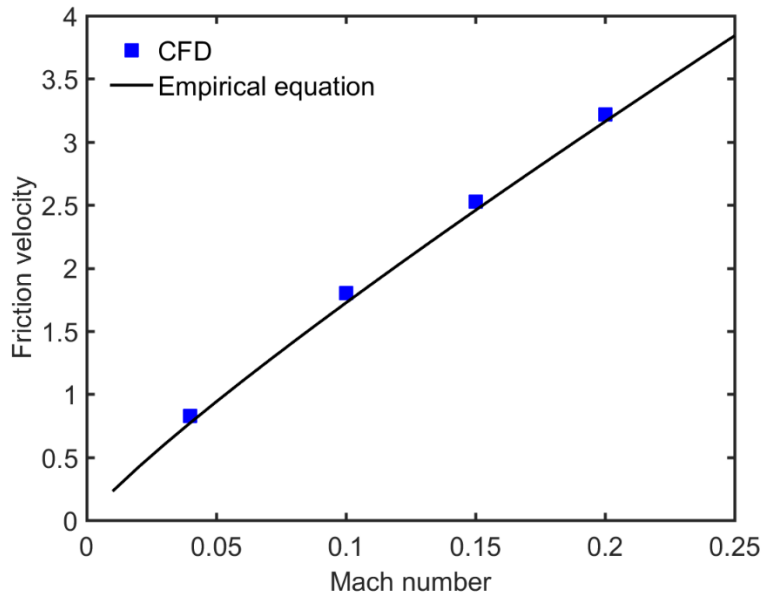


Figure 2.6. Comparison of the friction velocity between CFD and the empirical equation [92].

2.2.3. Acoustic impedance simulation and comparisons with experiments

The accuracy of the CFD model to predict the acoustic impedance of MPPs in the presence of grazing flow is validated through comparisons with experimental data reported in the literature.

According to the definition of the normalized acoustic impedance of a MPP hole (Eq. 1.5), the following equation is used for its calculation.

$$Z_{hole} = \frac{1}{\rho c} \frac{\bar{P}_{in} - \bar{P}_{out}}{\bar{u}}, \quad (2.5)$$

where \bar{P}_{in} and \bar{P}_{out} are the space-averaged acoustic pressure over the inlet and outlet surfaces of the hole, respectively, \bar{u} is the space-averaged acoustic velocity normal to the hole cross-section. Since the acoustic wavelength is much larger than the thickness of the hole, the normal acoustic velocities at both sides of the hole can be assumed to be the same.

The normalized acoustic impedance of the entire MPP can then be obtained by

$$Z_{MPP} = \frac{Z_{hole}}{\delta} = R + j\chi, \quad (2.6)$$

where R and χ are the normalized acoustic resistance and reactance, respectively.

Fast Fourier transform (FFT) is performed on the stable cycles of the related time signals, and their complex values at the acoustic frequency are determined [90]. Using Eqs. 2.5 and 2.6, the normalized acoustic impedance of MPP is then deduced.

The acoustic behavior of Panel 1 under different flow speeds is first investigated, for a Mach number varying from 0.04 to 0.25 and an acoustic excitation at 111 dB at 3150 Hz. Note this frequency is chosen to enable comparisons with the data provided in reference [55]. The Mach numbers alongside the corresponding Reynolds numbers of the computation cases are listed in Table 2.2.

TABLE 2.2. Computational cases.

Mach number	0.04	0.08	0.1	0.15	0.16	0.2	0.25
R_e	21108	43271	52769	79153	84430	105538	131923

The acoustic impedance of Panel 1, obtained from the CFD simulations and from experimental measurements [55], is compared in Fig. 2.7. Both sets of results show that the acoustic resistance increases with the Mach number, while the reactance decreases. It can also be seen that the experimentally observed trend and the magnitude of the impedance terms are reasonably well reproduced by the CFD simulations.

Note that, in the no-flow case, an end correction term appears in the reactance part in Eq. 2.6 to count for the effective mass flowing through the hole. This, however, is difficult to be precisely determined in the present case, which apparently depends on the flow conditions. The end-correction, however, is not necessary to the resistance part with flow, since dissipation mainly takes place inside the hole. It is also pertinent to note that previous work [90] has shown that, with grazing flow, the acoustic resistance is insensitive to frequency variations (also confirmed in the following analyses in Chapter 3). Therefore, the comparison, though at only one frequency, is deemed representative enough.

The above validations confirm the validity of the acceptable accuracy of the proposed CFD model, which is to be used for flow analyses and the development of the

acoustic impedance prediction formula.

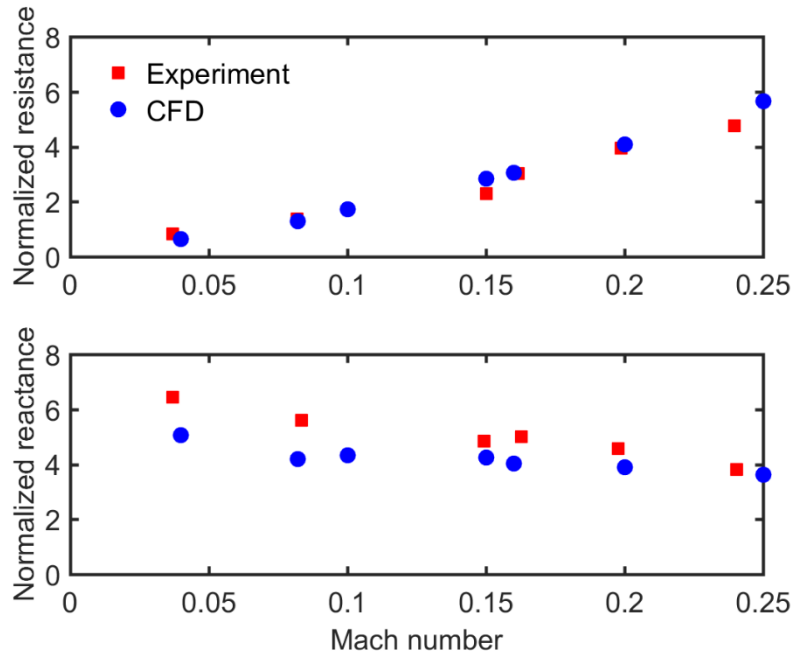


Figure 2.7. Comparison of the normalized acoustic impedance of panel 1 between CFD and experiments.

2.3. Flow field visualizations and analyses

In this section, the flow field near the MPP hole under different flow speeds and acoustic forcing is investigated and presented in detail with the aim to better understand the sound energy dissipation mechanism, the mechanisms behind the changes in impedance with grazing flow and find the intrinsic flow parameters which can better describe the grazing flow effects on the impedance.

2.3.1. Flow field at different Mach numbers

Analyses on the flow field near the MPP aperture and inside the hole would help better understand the physical process of the flow-acoustic-MPP interaction. To this end, the case without acoustic excitation is first examined. Fig. 2.8 shows the velocity streamlines of the mean grazing flow near the hole of the resonator at different Mach numbers. It can be seen that the flow passes over the hole with no visible fluid flowing into or out of the cavity through the hole, along with the formation of a shear layer above it. The grazing flow induces an additional flow motion inside the hole by the shear stress transmitted through the hole in the wall. At a low Mach number, *i.e.* $M=0.04$, two vortical flow regions in the hole are observable. In the upper region, a big vortex with clockwise rotation is formed, entraining a smaller one in the lower area with counterclockwise rotation. The vortices together with the small hole would prevent the fluid entrainment through the hole. When the flow velocity increases, the smaller vortex in the lower part of the hole disappears while the upper vortical flow region grows, leading to an increase in the contacting area between the vortical flow and the wall of the hole.

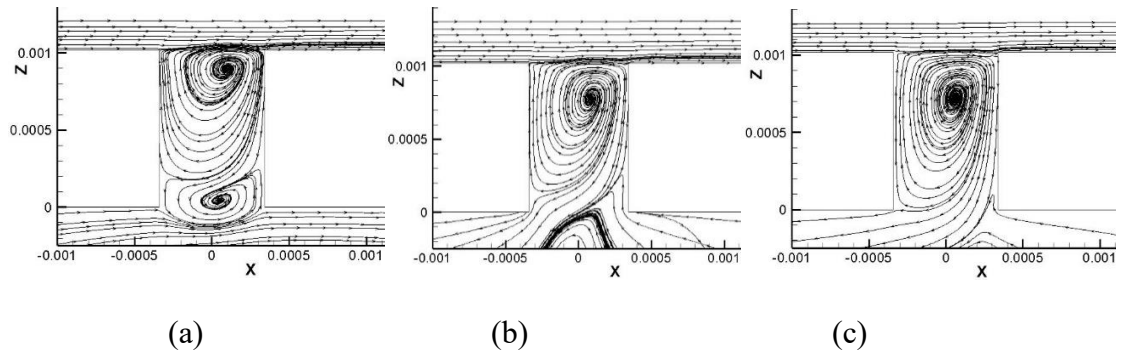


Figure 2.8. Velocity stream-lines of mean grazing flow near the hole of the resonator through $y=0$ cross section at different flow Mach numbers. (a) $M=0.04$, (b) $M=0.1$, (c) $M=0.25$.

Acoustic excitation is then added. As an example, the velocity streamlines near the hole with an acoustic excitation are shown in Fig. 2.9. It can be seen that, at a very low Mach number of $M=0.04$, different from the sole mean grazing flow case (Fig.2.8), fluid is entrained into the cavity. Meanwhile, the vortex in the upper area of the hole becomes smaller and the small vortex in the lower area of the hole with counter clockwise rotation disappears, as compared with the case without acoustic excitation (Fig. 2.8). However, the effect of the acoustic excitation on the global flow field is not obvious at other flow velocities. This can be explained by the fact that the size of the vortex in the hole gradually grows with the flow speed, along with an increase of the resistant effect of the vortex in the hole. In the present case, the acoustic energy is not strong enough to overcome the resistant effect of the vortex in the hole at high flow velocities. As a result, unlike the case of $M=0.04$, there is no fluid flowing into the cavity, and the streamline pattern near the hole is almost the same as the case without

acoustic excitation.

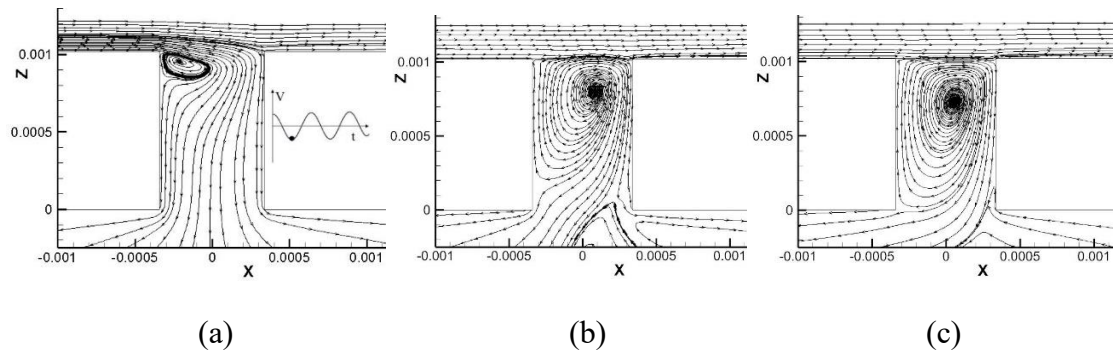


Figure 2.9. Velocity streamlines near the hole of the resonator through $y=0$ cross section at different flow velocities. $f=3.15$ kHz, $|V_a|=0.025$ m/s. (a) $M=0.04$, (b) $M=0.1$, (c) $M=0.25$.

2.3.2 Flow field at different SPLs

Figure 2.10 shows the velocity streamlines near the orifice at different instants within one cycle at different sound pressure levels (SPLs). At 111 dB, the results shown in Fig. 2.9b have indicated that the fluid flows across the orifice with no obvious air flowing into the cavity through the orifice. At 120 dB, it can be seen that a portion of fluid starts to flow into and then out of the cavity through the orifice at different instants of one acoustic cycle. When the sound pressure level becomes even higher, the amount of fluid flowing into and out of the cavity through the orifice increases correspondingly. Meanwhile, the size of the vortex formed in the hole continuously shrinks and finally disappears. The inflow and outflow pattern together with the interactions between the

acoustic wave and the grazing flow field become more obvious, resulting in an increase in the movement of the shear layer above the orifice, larger effective areas for fluid flow through the orifice as well as the discharge coefficient.

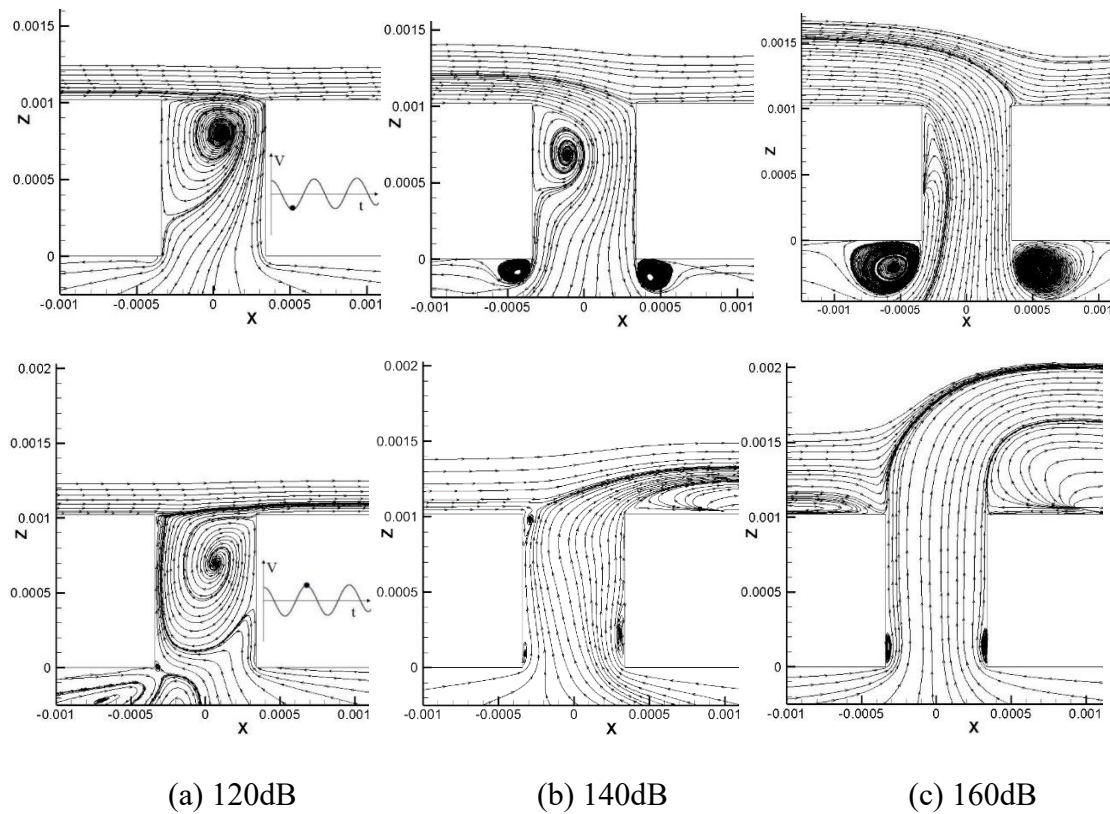


Figure 2.10. Velocity streamlines near the orifice of the resonator through $y=0$ cross section at different sound pressure level. $M=0.1$, $f=3.15$ kHz.

The vorticity fields near the orifice at different SPLs are shown in Fig. 2.11. It can be seen that below 140 dB the excitation energy is not high enough to generate the shear layer separation from the wall of the orifice. Acoustic induced vortex shedding starts to appear at 140 dB, though not very obvious. At an even higher sound pressure level 160 dB, the vorticity activity becomes much stronger.

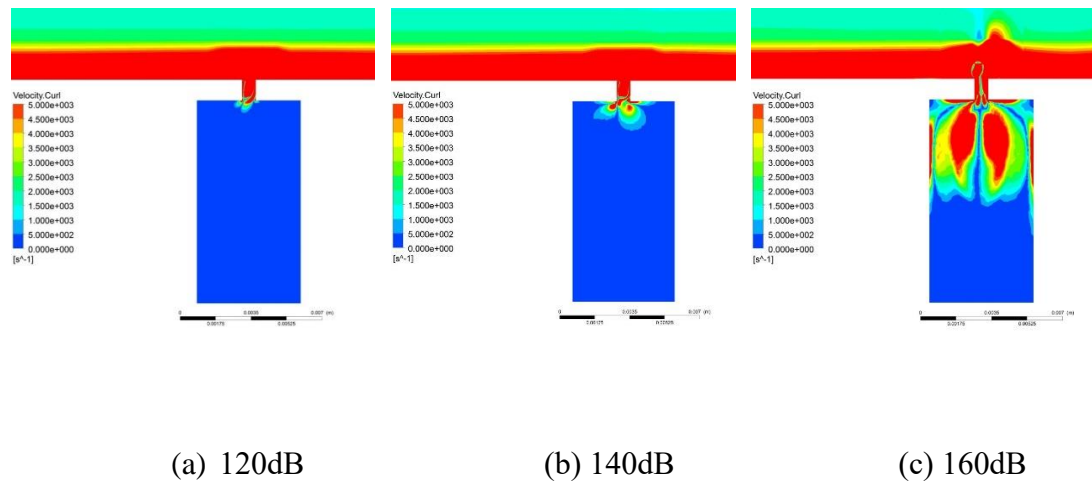


Figure 2.11. Vorticity field near the orifice through $y=0$ cross section at different sound pressure level. $M=0.1$, $f=3.15$ kHz.

2.3.3 Sound energy dissipation mechanism

It is believed that the vortex in the hole induced by the steady grazing flow can prevent fluid from going into and out of the cavity. When inflow and outflow occur, part of the sound energy is dissipated to overcome the resistant effects of the vortex in the hole. In addition, the shear layer above the hole would move up. This movement would contribute to the sound energy dissipation as well. Consequently, the sound energy consumed increases with the amount of fluid flowing into and out of the cavity as interpreted by many researchers [54, 55, 58, 65, 66]. As the discharge coefficient and the movement of the shear layer are related to the rate of the fluid reaching the cavity, some impedance models [54, 58, 65, 66] are proposed based on the discharge coefficient and the movement of the shear layer above the orifice.

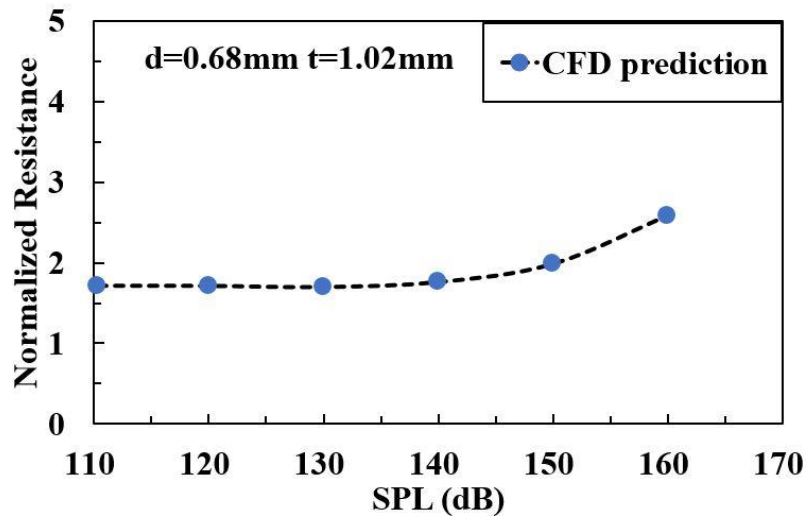


Figure 2.12. Normalized resistance of panel 1 at different SPLs predicted by CFD.

$$M=0.1, f=3.15 \text{ kHz.}$$

The acoustic resistance of panel 1 at different SPLs, predicted by CFD simulations, is plotted in Fig. 2.12. As can be seen, below 140 dB the resistance is almost constant, independent of the SPL, typical of linear behavior. Starting from 140 dB, it starts to increase. The above flow field analyses show that below 140dB, in its linear region, the phenomenon that fluid flows into and out of the cavity intensifies with the increase of the SPL and above 140 dB acoustic induced vortex shedding takes place. The result that the resistance remains nearly constant when inflow and outflow intensify and change until vortex shedding takes place clearly indicates that the enhancement of the inflow and outflow does not generate more sound energy dissipation and it is therefore plausible that the sound energy dissipated by overcoming the resistance of the vortex and the movement of the shear layer is much smaller than the viscous effects near the

hole. Thus, before vortex shedding takes place, the dominant acoustic energy dissipation mechanism should be the viscous effects. The effects of the resistance to the vortex in the hole as well as shear layer movement can be neglected compared to the viscous effects for the micro small-scale holes.

Based on the above discussions, it is clear that the sound energy of MPPs is dissipated mainly due to the viscous effects and vortex shedding with a grazing flow. In the linear SPL region, most of the acoustic energy is dissipated through viscous dissipation in the shear layer near the orifice, irrespective of the amount of inflow and outflow fluid. At extremely high SPL, vortex shedding should be the dominant contributing factor to the energy dissipation. Between the high and linear sound pressure level range, the acoustic dissipation mechanism transits from viscous dissipation in the shear layer near the orifice to the chaotic vortex shedding dominated dissipation.

2.3.4 Increase of the acoustic resistance with flow velocity

It is well established that the resistance part of the acoustic impedance increases with flow velocities. Based on the analysis of flow field near the orifice, the reasons behind this phenomenon could be explained as follows.

As shown in Fig. 2.8, with the increase of the flow velocity, the vortex in the hole

becomes larger, resulting in an increase of the contact area between the vortical flow in the hole and the wall of the hole. Meanwhile, the velocity near the wall of the hole also increases, generating a larger velocity gradient at the wall. Since the viscous force is proportional to the gradient of the flow velocity and the contacting area, the viscous force near the wall of the hole would also increase with the flow velocity. Thus, under acoustic excitation, more energy could be dissipated through viscous effects due to the increase of the viscous effects near the wall of the hole. This can explain why the resistance increases with the flow velocities. This explanation is quite different from reasons given by previous researchers, such as, the “blowing away” process [61-64], the increase movement of the shear layer above the hole [58, 65] and the discharge coefficient [54, 55, 66, 67].

2.3.5. Intrinsic flow parameters for acoustic impedance prediction

The flow field near the hole can be seen as a superposition of the oscillating flow field caused by the acoustic excitation and the grazing flow. It can be surmised that the flow parameter which can best determine the flow field near the hole would influence the acoustic impedance of the MPP holes. An enlightening example is the case of a linear shear flow passing over a plane wall with a circular hole, generating the so-called Stokes flow near the hole [93-97], in which case the local Reynolds number based on the diameter of the orifice is smaller than 1. The exact solution by Davis [97] suggests that the velocity gradient of the linear shear flow might be the key parameter which determines the distribution of the velocity and pressure near the hole. Enlightened by

the work of Davis [97], we propose the flow velocity gradient in the viscous sublayer as the new flow parameter, and subsequently establish its link to the acoustic impedance of the MPP hole in Chapter 3. The choice of the velocity gradient is also supported by the flow field analyses, reported in Section 2.3.1. With the viscous sublayer being adjacent with the flow field in the hole, the velocity gradient in this layer produces the shear stress, responsible for the flow pattern in the hole as well as the acoustic energy dissipation.

2.4. Summary

The acoustic behavior of micro-perforated panels, exposed to a fully developed grazing turbulent flow, is investigated through numerical simulations. Grazing flow- and acoustic wave-excited flow field near the orifice of the MPP under different flow conditions is scrutinized through 3D URANS CFD simulations.

Based on the analyses of the flow field near the orifice, the following conclusions can be drawn.

1. Flow pattern near the orifice of micro-perforated panels

- Without an acoustic excitation, the fluid flows across the hole of the MPP to form a thick shear layer above it. At a low flow speed, two vortical flow regions appear in the orifice. In the upper area, a big vortex with clockwise rotation is formed due

to the shear stress transmitted through the hole. It then entrains a smaller vortex with a counter clockwise rotation in the lower area of the hole. With the increasing flow speed, the smaller vortex disappears and the big vortex in the upper area of the hole becomes larger, creating an increasing resistance effect.

- Acoustic excitation promotes the flow passing through the hole at a low flow speed. This is due to the relatively smaller size of the vortex formed in the hole and relatively weak resistant effects.

- Because of the resistance effect of the vortex in the MPP hole, when the sound pressure level of the acoustic excitation is not high enough, the flow field near the hole is almost the same as the one with only grazing flow and the influence of the acoustic excitation on the flow field is insignificant. While increasing the sound pressure level, fluid starts to flow into and out of the cavity through the orifice. This inflow and out flow pattern becomes stronger with the increase of the sound pressure level.

- Acoustic induced vortex shedding happens near the hole at high sound pressure levels.

2. Sound energy dissipation mechanism

- The resistance effects of the vortex, as well as the movement of the shear layer

above the hole, is negligible compared to the viscous effects and vortex shedding inside the hole and at its exit. The dominant sound energy mechanism is basically the viscous effects and vortex shedding effect with grazing flow.

- In linear sound pressure level region, most of the acoustic energy is dissipated through viscous dissipation in the shear layer near the wall of the hole, irrespective of the flow pattern.
- Between high and linear range sound pressure levels, the acoustic dissipation mechanism transits from viscous dissipation in the shear layer near the hole to the chaotic vortex shedding.
- When SPL far exceeds the linear sound pressure level region, vortex shedding dominates the energy dissipation.

3. Explanation on the increase of the acoustic resistance with the flow velocity

The increase of the viscous force near the wall of the hole with flow velocities leads to the increase of the sound energy being dissipated through the viscous effects in the shear layer near the hole wall.

4. Flow parameters determining the acoustic impedance

The velocity gradient in the viscous sublayer over the duct wall is identified as the

intrinsic flow parameter which is inherently correlated to the acoustic resistance of the MPPs with grazing flow.

The numerical analyses conducted in this Chapter reveal the underlying physics of the flow-MPP interaction, the dominant energy dissipation mechanism and the intrinsic flow parameter to be used for the acoustic impedance prediction of MPPs. This paves the way forward to the establishment of prediction model for acoustic impedance of MPP in grazing flow, which will be reported in Chapter 3.

Chapter 3. Impedance Prediction Formula and Validation

In this chapter, the relationship between the velocity gradient in the viscous sublayer region over the duct wall and the acoustic impedance of the MPP orifice under a grazing turbulent flow is investigated through numerical experiments. The excellent agreement of the acoustic resistance between the CFD and experimental data along with the relatively low computation cost of the URANS, as detailed in Chapter 2, establish the fact that the CFD is a reliable tool to be adopted. Based on a large amount of numerical simulations, a new acoustic impedance model of MPPs in grazing flow is to be proposed in this Chapter after identifying a new flow characteristic parameter. Measurements based on an inverse impedance derivation method are then carried out to experimentally obtain the acoustic impedance of a MPP under the low-speed grazing flow condition within a linear acoustic excitation region. Finally, the accuracy of the acoustic impedance prediction model and the improvement it brings about are demonstrated through comparisons with the measured data, as well as the experimental data published in the literature.

3.1. Acoustic impedance prediction formula

3.1.1. Relationship between the velocity gradient and the acoustic resistance of MPPs

To establish the relationship between the velocity gradient in the viscous sublayer over duct wall, denoted by G , and the acoustic resistance of MPPs under a grazing

turbulent flow, numerical experiments are carried out. Panel 1, the same one used in [55] is firstly investigated . After finding the relationship between the velocity gradient in the viscous sublayer and the acoustic resistance of this panel, other panels will be used for further verifications. For each panel, additional computational cases are considered with details tabulated in Table 3.1. In each case, the panel is exposed to the same flow speed range and acoustic excitation level as Chapter 2, but at different frequencies.

TABLE 3.1. Computational cases used to find the relation between G and the acoustic resistance.

Velocity amplitude of the incident acoustic wave (m/s)	Frequency (Hz)	Mach number	R_e
$ V_a = 0.025$	3150, 3000, 2800, 2600, 2400	0.1	52769
	3300, 3150, 3000, 2800, 2600,	0.15	79153
	3300, 3150, 3000, 2800, 2600,	0.2	105538
	3300, 3150, 3000, 2800, 2600,	0.25	131923

In the presence of the grazing flow, we replace R_{out} in Eq. 1.7b (representing the viscous loss outside the hole for MPPs without flow) with a new term, θ , to account

for the changed viscous loss. Therefore, the normalized acoustic resistance of the MPP,

R_{flow} , writes

$$R_{flow} = R_{in} + \theta. \quad (3.1)$$

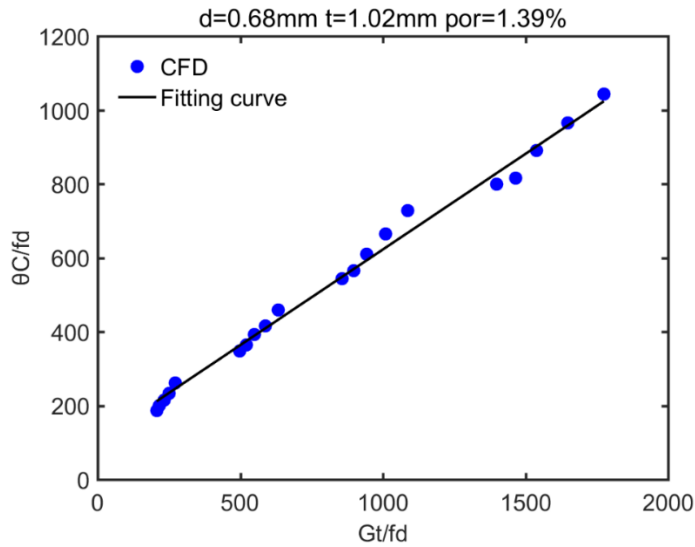


Figure 3.1. Relationship between θ and G for Panel 1. $|V_a|=0.025\text{m/s}$.

Both θ and G are non-dimensionalized as θ_c / fd and Gt / fd , respectively.

Fig. 3.1 displays the CFD results using Panel 1 at different excitation frequencies ranging from 2400 to 3300 Hz at different flow velocities. The plot is regrouped into four groups, each having the same Mach number but different frequencies. The corresponding Mach number varies from 0.1 to 0.25. As observed in Fig. 3.1, although each group of results seems to have a slightly different slope, there seems to exist a rather linear relationship between the two parameters (θ_c / fd and Gt / fd) which can be reasonably well represented by a straight line. This also confirms that the

amended term in the acoustic resistance formula under grazing flow is related to the velocity gradient in the viscous sublayer region.

To further confirm the generality of the observed linear relationship, two other MPPs (Panels 2 and 3 in Table 2.1) with different hole dimensions are also examined through CFD simulations (with cases listed in Table 3.1). Results are shown in Fig. 3.2, which show that, though following a different slope, the previously observed linear relationship between θ_c / fd and Gt / fd still holds reasonably well, confirming the general nature of the observations made on Panel 1.

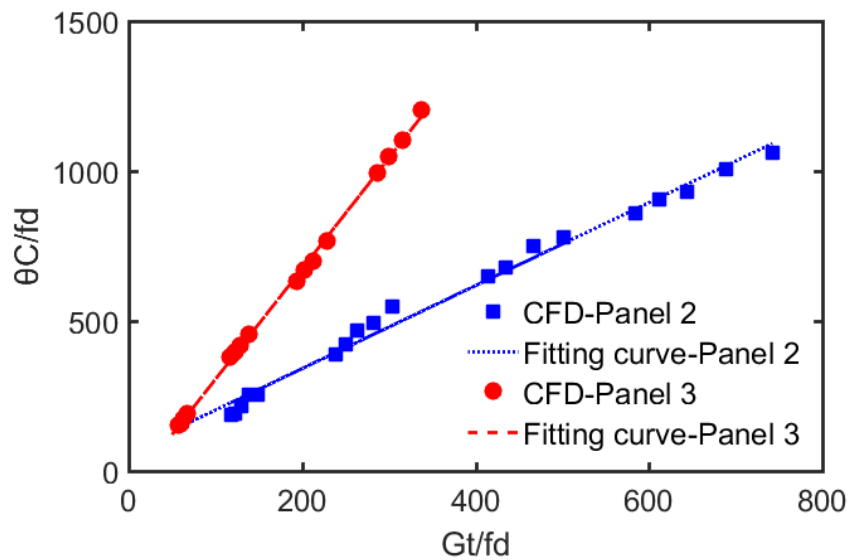


Figure 3.2. Relationship between θ and G for panel 2 and 3. $|V_a|=0.025\text{m/s}$.

A linear regression analysis is then conducted to establish the observed linear relationship as:

$$\frac{\theta c}{fd} = A \frac{Gt}{fd} + B, \quad (3.2)$$

where A and B, as a function of t/d , are to be determined. Curve-fitting the CFD calculated resistance data for panel 1, 2 and 3 leads to the following expression:

$$\frac{\theta c}{fd} = \left[0.0356 \left(\frac{t}{d} \right)^{-3.236} + 0.0157 \right] \frac{Gt}{\delta fd} + \left[1.369 - 2.331 \left(\frac{t}{d} \right)^{-2.195} \right] \frac{1}{\delta}. \quad (3.3)$$

3.1.2. Impedance prediction model of MPPs and validations

Combining Eqs. 3.1 and 3.3, a normalized acoustic resistance formula for MPPs under grazing turbulent flow is established as follows:

$$R_{flow} = R_{in} + \theta = R_{in} + \left[0.0356 \left(\frac{t}{d} \right)^{-3.236} + 0.0157 \right] \frac{Gt}{\delta c} + \left[1.369 - 2.331 \left(\frac{t}{d} \right)^{-2.195} \right] \frac{fd}{\delta c}, \quad (3.4)$$

with G calculated by Eqs. 2.1 to 2.4 for square flow ducts.

This new acoustic resistance prediction formula replaces the Maa's formula [23], to be applied when a grazing flow is present. As discussed in Chapter 2, the presence

of grazing flow affects the viscous effects near the hole. Therefore, the only flow-related term θ can be interpreted as the one to account for the changes in the flow-induced viscous effects. This acoustic prediction formula also indicates that with the grazing flow, the acoustic behavior of MPPs is not only dependent on the traditional panel related parameters, such as the hole diameter d , perforation ratio δ and panel thickness t , but also the parameters which can change its surrounding flow field such as the size of the duct and the flow velocity, since the velocity gradient is determined by these parameters. The above analysis also demonstrates that the case with flow is much more complicated than the case without flow.

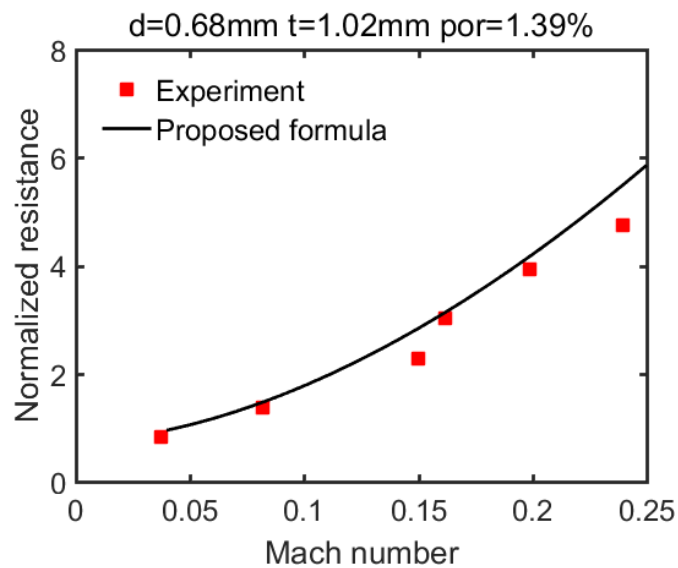


Figure 3.3. Normalized acoustic resistance comparisons between proposed formula and experimental data for panel 1. $f=3.15$ kHz, $|V_a|=0.025\text{m/s}$.

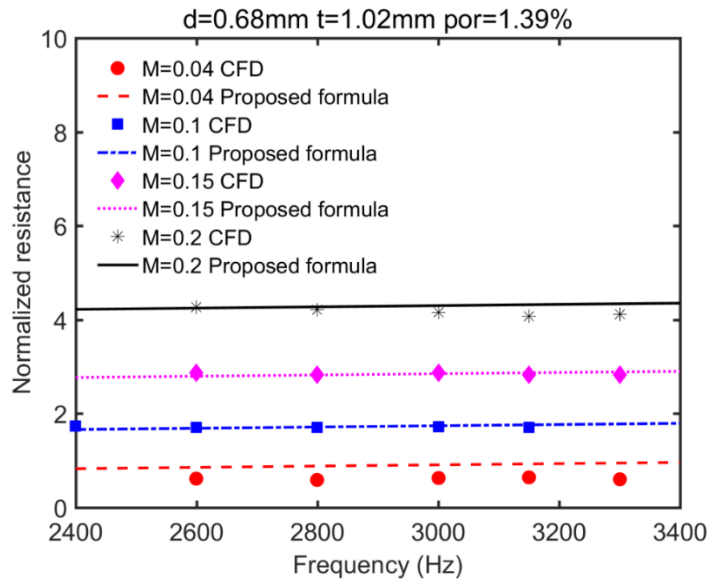


Figure 3.4. Normalized acoustic resistance comparisons between proposed formula and CFD for panel 1. $|V_a| = 0.025\text{m/s}$.

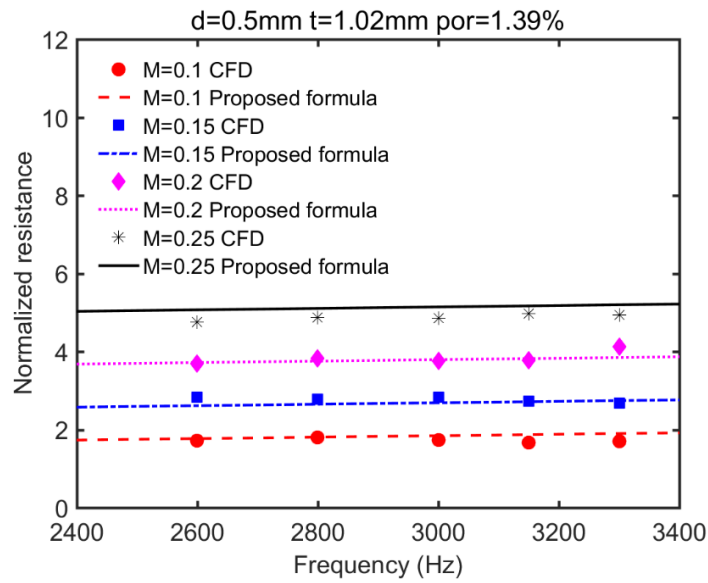


Figure 3.5. Normalized acoustic resistance comparisons between proposed formula and CFD for panel 2. $|V_a| = 0.025\text{m/s}$.

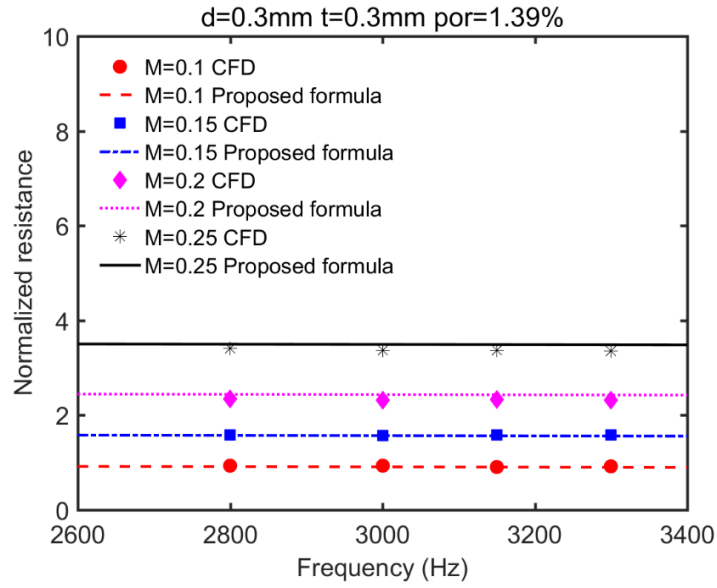


Figure 3.6. Normalized acoustic resistance comparisons between proposed formula and CFD for panel 3. $|V_a| = 0.025m/s$.

For validation purposes, Fig. 3.3 shows a comparison of the normalized acoustic resistance between the proposed formula (Eq. 3.4) and the experimental data for Panel 1, reported in [55]. Meanwhile, the same comparisons with the CFD data for Panel 1, 2 and 3 at other frequencies are also given in Figs.3.4-3.6, respectively, with different Mach numbers. These comparisons clearly show that the proposed formula can not only capture the trend but also agree well with both the experimental data and CFD simulations. They also confirm the fact that the resistance is nearly constant and insensitive to frequency variations.

It should also be pointed out that the above analyses and the proposed acoustic resistance formula are based on a number of selected cases. Therefore, the validity range, as verified in the present study, is limited to the variation range of the parameters

used in the simulation, e.g. $R_e \leq 131923$ (corresponding to $M \leq 0.25$ for current cases), $1 \leq \frac{t}{d} \leq 2$ and under linear acoustic excitation range.

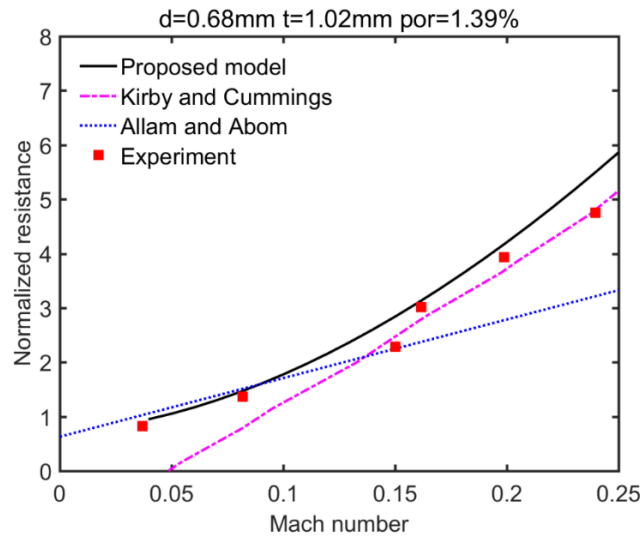


Figure 3.7. Comparisons between the proposed formula with that of Kirby and Cummings [70] and that of Allam and Abom [75] for panel 1. $f=3.15$ kHz, $|V_a|=0.025$ m/s.

Additional comparisons with other existing models reported in the literature are finally conducted. To this end, Kirby and Cummings' model [70] and Allam and Abom's model [75] are used, with results shown in Fig. 3.7. To facilitate comparisons, experimental data [55] are also provided on the same figure. It can be seen that the prediction results by the present formula seem to fit the measured data better than the other two models. More specifically, compared with Kirby and Cummings' model, the present model seems to work better, especially at low Mach number range before 0.1. In the higher Mach number region, the proposed formula follows better experimental

data than Allam and Abom's model. Over the entire region, the proposed model can capture the nonlinearly increasing trend of the acoustic resistance.

As a final remark, it should be noted that the above analyses heavily focus on the acoustic resistance part of the impedance formula. To complete the acoustic impedance prediction, the proposed resistance formula (Eq. 3.4) can be combined with the acoustic reactance prediction model proposed by Cummings [77], which was tested to show rather good consistency against the experimental results on Panel 1 as plotted in Fig. 3.8. Casting Cummings' reactance formula by using parameter G proposed in this paper is straightforward. Combined with Eq. 3.4, a complete set of the acoustic impedance prediction formula for MPPs with grazing flow within the linear acoustic regime is established and written as,

$$Z_{flow} = R_{flow} + j\chi_{flow}, \quad (3.5)$$

where R_{flow} and χ_{flow} are the normalized acoustic resistance and reactance of the MPPs, respectively, detailed as

$$R_{flow} = R_{in} + \left[0.0356 \left(\frac{t}{d} \right)^{-3.236} + 0.0157 \right] \frac{Gt}{\delta c} + \left[1.369 - 2.331 \left(\frac{t}{d} \right)^{-2.195} \right] \frac{fd}{\delta c},$$

$$\chi_{flow} = \frac{\omega}{\delta c} \left[t + \varepsilon \frac{8d}{3\pi} \right] \quad (3.6)$$

$$\varepsilon = (1 + 0.6t/d) \exp \left[-(\sqrt{Gv}/ft - 0.12d/t)/(0.25 + t/d) \right] - 0.6t/d$$

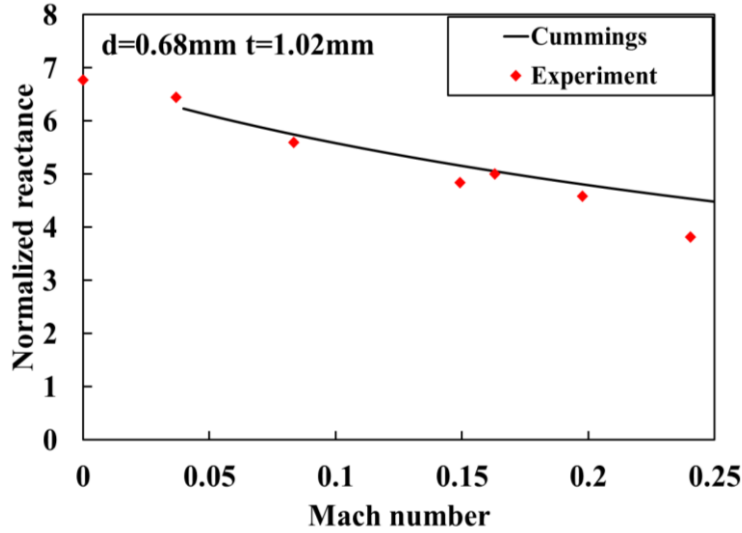


Figure 3.8. Normalized acoustic reactance comparisons between Cummings' [77]

model and experimental data for panel 1. $f=3.15$ kHz, $|V_a|=0.025$ m/s.

As mentioned before, both previous work [58, 65, 75] and the CFD simulations in Figs. 3.4-3.6 show that, with grazing flow, the acoustic resistance is roughly independent of frequency. Therefore, the experimental data found in literature, though at one frequency, is rather representative. Similarly, the limited cases being investigated in this section, actually cover a much wider scope and applicable for a range of different frequencies. However, considering the very scarce experimental research on MPPs with low grazing flow velocity under linear acoustic excitation region, the proposed formula has only been compared with a very limited amount of experimental data reported in

the literature [55] up to now. Meanwhile, in a broader sense, it is felt that the lack of sufficient experimental data on MPPs under well-controlled testing conditions is a bottlenecking problem, hampering the development of the acoustic impedance prediction tools for the study of MPPs in flow.

Motivated by this, hereafter, experiments are conducted to educe the acoustic impedance data of a MPP under various flow velocities inside a flow duct using a previously developed impedance derivation technique [98]. The educed impedance data are then used to further validate the established impedance formulae.

3.2. Impedance derivation method

An inverse approach is used for the acoustic impedance derivation. The impedance of a liner, flushed mounted in a flow duct, can be inversely educed by minimizing the difference between the experiment results and a wave propagation model, as detailed in reference [98]. For the completeness of the study, the derivation method is briefly recalled here.

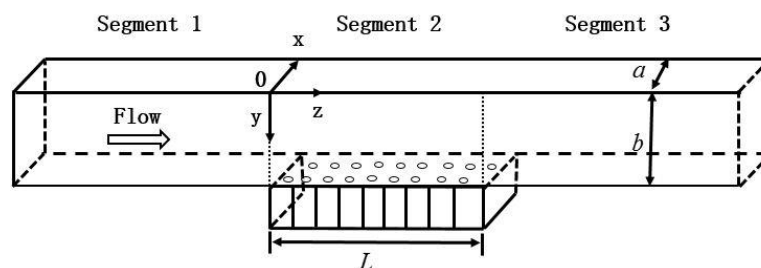


Figure 3.9. Sketch of the system.

Figure 3.9 describes the system under investigation along with the Cartesian coordinate system used in the model. Incident acoustic waves propagate along the duct with a grazing flow. A locally reactive MPP absorber, with a length of L , is flush-mounted on one of the side walls of the duct. The system is divided into three segments: a lined segment ($0 < Z < L$) with uniformly distributed surface impedance and two unlined ones, upstream ($Z < L$) and downstream ($Z > L$), denoted by segment 1, 2 and 3, respectively. It is assumed that the incoming grazing flow in the duct, with an average (bulk) Mach number M , is inviscid and uniform across the cross section of the duct. Harmonic acoustic waves propagating in the uniform mean flow are governed by the convected wave equation:

$$\nabla^2 p - (jk + M \frac{\partial}{\partial z})^2 p = 0, \quad (3.7)$$

where $j = \sqrt{-1}$ and $k = \omega / c$ is the free-space wave number.

Over the rigid and unlined portion of the duct walls, the normal particle velocity vanishes, yielding either

$$\frac{\partial p}{\partial x} = 0, \quad (3.8)$$

or

$$\frac{\partial p}{\partial y} = 0, \quad (3.9)$$

on the respective parts of the duct.

Over the lined duct portion in segment 2, Ingard-Myers boundary condition is imposed, which writes

$$jkv_y(x, b, z)Z_s = [jk + M \frac{\partial}{\partial z}]p_2(x, b, z), \quad (3.10)$$

where Z_s is the normalized surface acoustic impedance of the liner absorber.

The acoustic pressure $p(x, y, z)$ in different duct segments can then be expressed in the following form based on the classical mode-decomposition theory:

$$p_1(x, y, z) = \sum_N \varphi_N (A_N^+ e^{-j\alpha_N^+ z} + A_N^- e^{-j\alpha_N^- z}), \quad (3.11)$$

$$p_2(x, y, z) = \sum_N \phi_N (B_N^+ e^{-j\beta_N^+ z} + B_N^- e^{-j\beta_N^- z}), \quad (3.12)$$

$$p_3(x, y, z) = \sum_N \psi_N (C_N^+ e^{-j\gamma_N^+ z} + C_N^- e^{-j\gamma_N^- z}), \quad (3.13)$$

where φ_N , ϕ_N and ψ_N are the N th mode shape functions of the cross section of the duct in segments 1, 2 and 3, respectively, analytically expressed as

$$\varphi_N(x, y) = \cos(k_{m1}x) \cos(k_{n1}y), \quad (3.14)$$

$$\phi_N(x, y) = \cos(k_{m2}x) \cos(k_{n2}y), \quad (3.15)$$

$$\psi_N(x, y) = \cos(k_{m3}x) \cos(k_{n3}y), \quad (3.16)$$

with the wave numbers in x and y directions being

$$k_{m1} = m_1\pi/a, \quad k_{n1} = n_1\pi/b, \quad \text{and} \quad m_1, n_1 = 0, 1, 2, \dots, \quad (3.17)$$

$$k_{m2} = m_2\pi/a, \quad \text{and} \quad m_2 = 0, 1, 2, \dots, \quad (3.18)$$

$$k_{m3} = m_3\pi/a, \quad k_{n3} = n_3\pi/b, \quad \text{and} \quad m_3, n_3 = 0, 1, 2, \dots. \quad (3.19)$$

The wave number in the y -direction k_{n2} in segment 2 can be sought from the following eigenvalue problem:

$$-\frac{1}{Z_s} (k - M\beta_N^\pm)[k - M\beta_N^\pm] = jkk_{n2} \tan(k_{n2}b). \quad (3.20)$$

The axial wave numbers α_N , β_N and γ_N in the three segments and their corresponding wavenumbers in the x and y directions satisfy the dispersion relation:

$$(k_x)^2 + (k_y)^2 + (k_z^\pm)^2 = (k - Mk_z^\pm)^2, \quad (3.21)$$

where the plus and minus superscripts denote waves travelling in the positive and negative z directions, respectively. The axial wavenumbers α and γ in the unlined parts, segments 1 and 3, can be directly derived by using Eqs. 3.17, 3.19 and 3.21.

By defining $A_s = \frac{1}{Z_s} = A_f\eta$, considering both A_s and k_{n2} as functions of η

ranging from 0 (rigid) to 1 (absorber), and differentiating Eqs. 3.20 and 3.21 with respect to η , the following ordinary differential equation can be obtained

$$\frac{dk_{n_2}}{d\eta} = \frac{A_f(k - Mk_z)^2}{-jk_0 \tan(k_{n_2}b) - jbk_{n_2} \sec^2(k_{n_2}b) + 2\eta A_f MW(k - Mk_z) k_{n_2} / k}, \quad (3.22)$$

$$W = \mp 1 / \sqrt{1 - (1 - M^2)[(\frac{k_{m2}}{k})^2 + (\frac{k_{n2}}{k})^2]}. \quad (3.23)$$

Using the 4th order Runge-Kutta integration scheme by integrating Eq. 3.22 over η from 0 to 1, the positive and negative axial wavenumbers as well as their corresponding wave numbers in y direction in the lined part (segment 2) can then be extrapolated.

The acoustic fields in the three segments are coupled together by using the mode-matching method by ensuring the continuity of the acoustic pressure and axial particle velocity at the interface between each pair of segments and the unknown modal amplitudes A , B and C in Eqs. 3.11-3.13 can be readily obtained given that the incidence and the boundary condition at the termination of the duct are known.

The unknown liner impedance is then obtained through an iterative procedure by minimizing the following objective function,

$$F = \sum_n^N (P_{n,sim} - P_{n,exp})(P_{n,sim}^* - P_{n,exp}^*), \quad (3.24)$$

where the superscript * represents the complex conjugate; $p_{n,exp}$ and $p_{n,sim}$ are the measured and computed sound pressure in the duct, respectively.

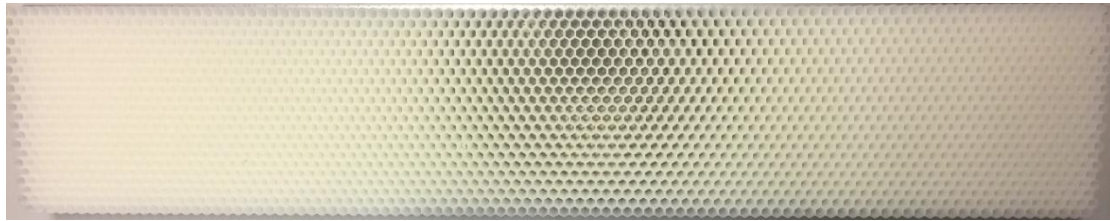
Considering only plane wave can propagate in the unlined downstream segment for the present study, the reflection effect of the termination of the duct is included by introducing the reflection coefficient only for the plane wave mode, as $R_0 = \frac{C_0^-}{C_0^+}$, which can be obtained by two microphones flushed mounted in the downstream unlined part of the duct.

3.3 Measurements

3.3.1 Test sample

The test sample, as shown in Fig. 3.10, is a single layer MPP absorber consisting of a micro-perforated panel, a honeycomb core and an aluminum backing plate. The edges of the absorber are carefully sealed to avoid acoustic leakage. The sample is designed to have a maximum sound absorption near 1200 Hz, below the cut-on frequency of the flow duct. The MPP, made of aluminum, has a dimension of 500 x 100 mm with cylindrical holes manufactured through chemical corrosion. The holes are manufactured to be uniformly distributed over the sample surface. The perforation ratio of the panel is 0.945%. Both the diameter of the hole and the thickness of the panel are 0.5mm. The honeycomb core is made of ABS resin, forming a backing layer of 25mm thick. It is designed and 3D printed to ensure that the center of each honeycomb cell is

coaxially aligned with a MPP hole. The honeycomb core is bonded to the MPP to rigidify the thin panel and make the MPP absorber locally reactive[53].



(a)



(b)

Figure 3.10. Test sample (a) Honeycomb core; (b) assembled honeycomb MPP absorber.

3.3.2 Experimental set-up

Measurements are conducted in a closed-loop low-speed acoustic wind tunnel with a background noise of around 82dB at the maximum flow speed considered in the current study. The working section is about 1.8m long with a cross section of 100 x 100 mm, corresponding to a cut-on frequency of 1700 Hz. As shown in Figs. 3.11 and 3.12, the honeycomb MPP absorber is flush-mounted on the upper wall of the square duct within its working section. Eleven $1/4$ -inch microphones (B&K 4935) are used to

measure the acoustic pressure at different locations along the duct. They are flush-mounted on the wall of the duct opposite to the absorber and connected to conditioning amplifiers (B&K Nexus 2691). The positions and the separation distance between the microphones are shown in Fig. 3.11. A single-tone acoustic excitation generated by a loudspeaker is used as the sound source within the frequency range below the cut-off frequency of the duct, thus allowing the sample to be exposed to a grazing plane wave excitation. Microphone 1 is used to monitor the sound pressure of the acoustic source. Preliminary tests are made to ensure the linear property of the MPP absorber by varying the incidence pressure levels up to 130dB. In the subsequent analyses, test cases using pure tone excitation at 110 dB, are used to make sure the results presented in this work are in a range where the MPP behave linearly. The middle span flow profile, upstream the absorber, is obtained by measuring the axial velocities at different positions in the normal wall direction through moving a pitot tube transversely across the duct.

Prior to the impedance derivation tests, microphones are calibrated to guarantee the quality of the measured data. As shown in Fig. 3.13, two microphones are closely mounted in the duct opposite to each other, whose outputs are used to calibrate the pressure amplitude and phase. For the calibration, the central portion of the duct are closed by rigid caps.

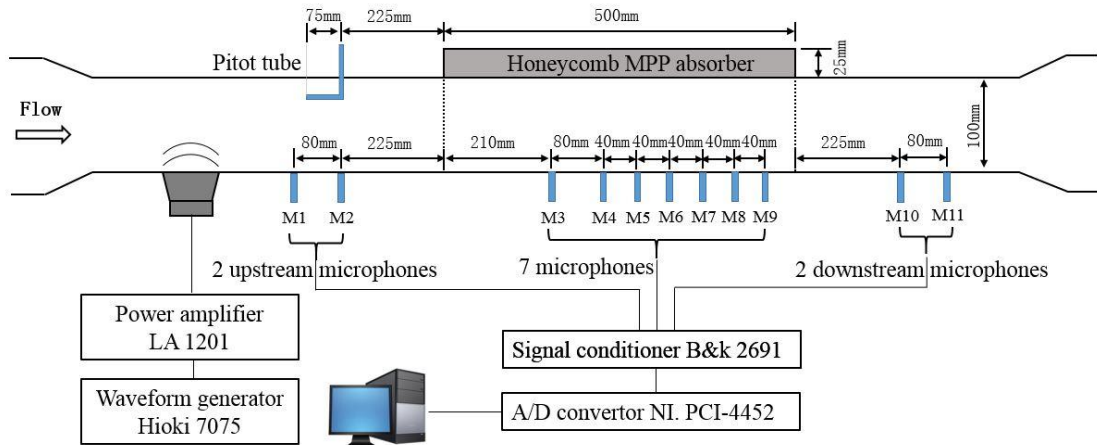


Figure 3.11. Sketch of the test setup for derivation of the acoustic impedance of a MPP liner.

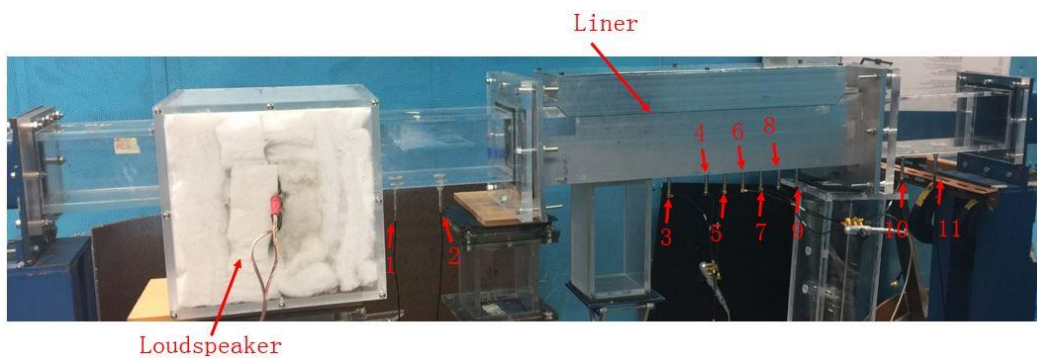


Figure 3.12. Experimental setup for derivation of the acoustic impedance of a MPP liner.

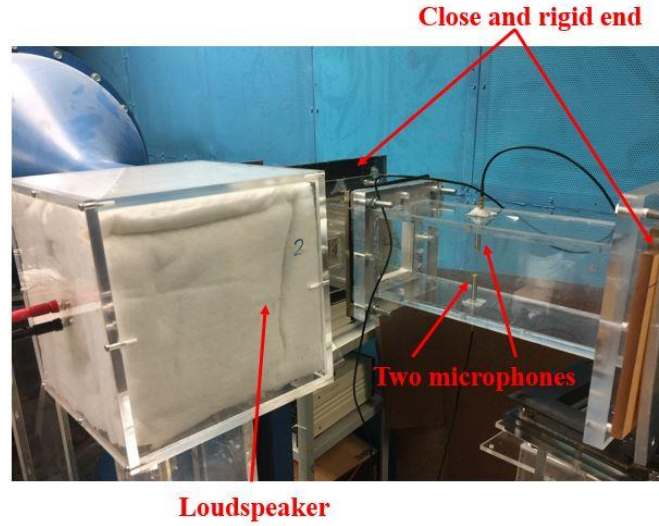


Figure 3.13. Setup for microphone calibrations.

3.4. Results and discussions

3.4.1 Mean flow profile in the duct

For a fully developed flow in a duct, the following well-adopted equations [91] can be used to calculate the mean stream-wise velocity.

$$U^+ = y^+ \quad \text{for } y^+ < 5 \text{ in viscous sublayer,} \quad (3.25)$$

$$U^+ = \frac{1}{0.41} \ln y^+ + 5.2 \quad \text{for } \frac{y}{e} < 0.1 \text{ in the inner flow region,} \quad (3.26)$$

$$\frac{\bar{u}_{cl} - \langle U \rangle}{u_\tau} = 0.008 \left(\frac{y}{e} \right)^{-2.76} \quad \text{for } \frac{y}{e} > 0.1 \text{ in the outer flow region,} \quad (3.27)$$

where \bar{u}_{cl} is the centerline velocity and e the half channel height. The friction velocity U_τ can be calculated by using Eqs. 2.2-2.4 for square flow ducts.

The inner flow region described by Eqs. 3.25 and 3.26 is universal and independent of the channel geometry. However, the geometry of the channel is important to the outer flow region described by Eq. 3.27, which here is interpolated from the experimental data. The measured mean stream-wise velocity profiles, upstream the MPP absorber, for different average flow Mach numbers are shown in Fig. 3.14, along with the theoretically calculated profiles. The good agreement between the two sets of data confirms the full development of the flow and also verifies the averaged Mach numbers calculated from the measured data.

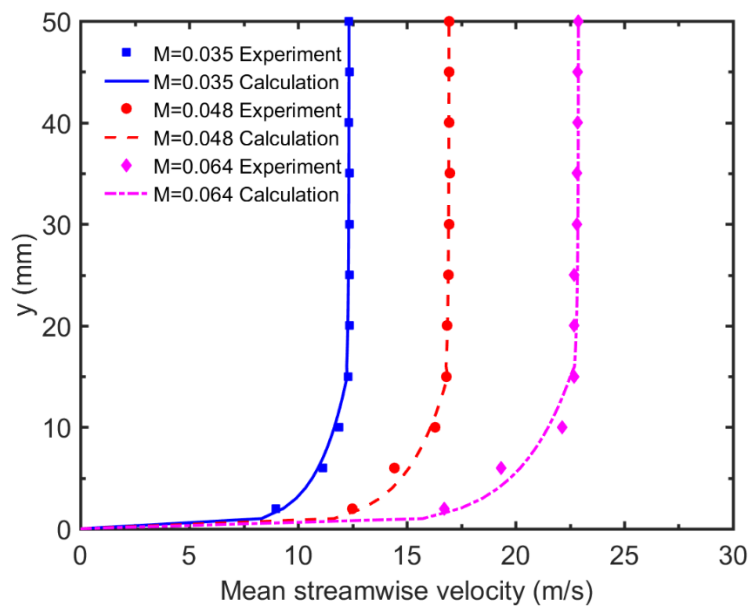


Figure 3.14. Mean flow profiles upstream the liner at different flow velocities.

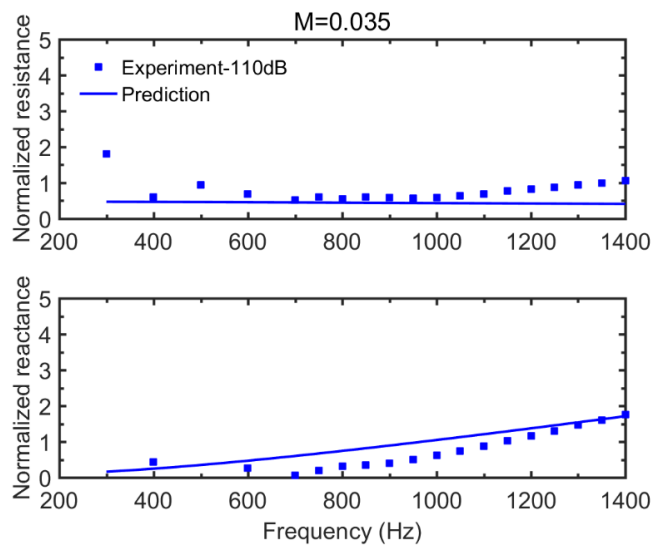
3.4.2 Measured and predicted MPP acoustic impedance

The proposed formulae Eq. 3.6, for the prediction of the acoustic impedance of

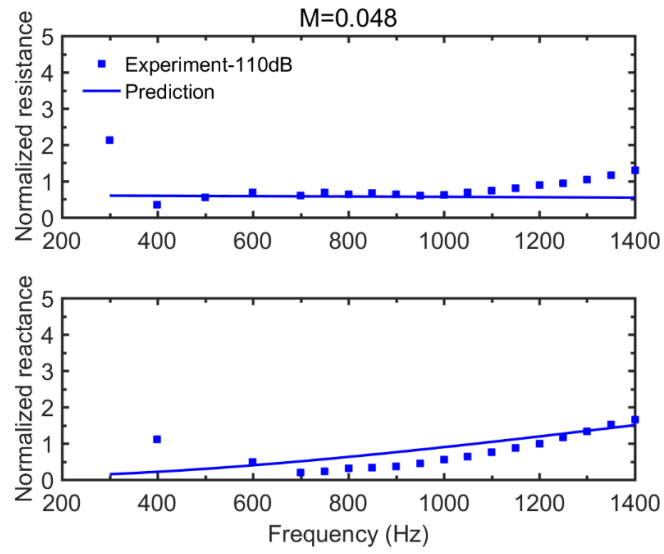
MPPs with grazing flow, are compared with the educed impedance data. The formulae have been validated in Section 3.1.2 through comparisons with the experimental data reported in reference [55]. However, as the published experimental data on MPPs with grazing flow are scarce and limited to some very specific test configurations, we will use the educed experimental impedance data under various flow velocities to provide further validation of the proposed impedance formulae.

Fig. 3.15 shows the comparison of the acoustic impedance between the results predicted by the proposed impedance formulae and the experimentally educed data at different flow speeds, corresponding to three different Mach numbers. The comparison shows acceptable agreement between the two sets of results. Discrepancies on the resistance observed at low frequencies are mainly due to the limited length of the liner with respect to the acoustic wavelength to support the impedance derivation process [99]. The distance between microphones, $L_{mic} = 80\text{mm}$ in the current study, actually determines the effective frequency range for measurement. Apparently, any frequency above $f_{limit} = (c + U_{\infty}) / 4L_{mic}$ cannot be reasonably measured. Meanwhile, when approaching the cut-on frequency of the duct, the non-planary nature of the acoustic waves start to gradually show, which may also partly explain the deviation at the high frequency end of the curves. Nevertheless, the comparison indicates that although the acoustic resistance prediction formula is established based on CFD generated data through numerical experiments in a relatively ideal environment, a reasonable agreement between the prediction results and experimental data at various flow speeds

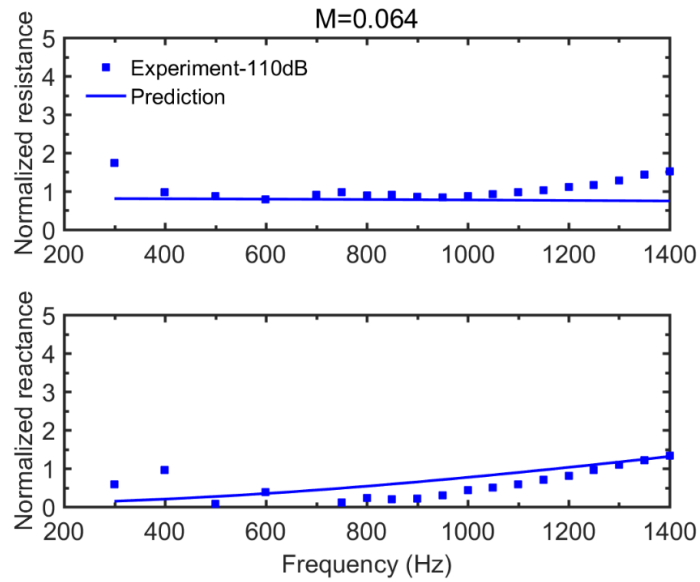
can still be observed. As to the reactance part, the formula developed by Cummings [77] can give reasonably good agreement with the experimental data as well. It is worth noting that the experiments were designed and carried out in accordance with the validation range of the proposed impedance formulae, specified in Section 3.1.2. As to other more complex cases which go beyond the flow-duct configuration or the pre-defined application range in Section 3.1.2, like flow with a higher Reynolds number over an open space, further investigations are needed to assess the applicability of the proposed impedance formula.



(a)



(b)



(c)

Figure 3.15. Comparisons of the acoustic impedance obtained from the prediction formulae and experiments at different flow velocities.

3.5. Summary

In this chapter, the acoustic impedance of Micro-perforated panels exposed to a fully developed grazing flow is investigated both numerically and experimentally. Numerical experiments are first carried out to find the relationship between the newly identified intrinsic flow parameter in Chapter 2, namely the velocity gradient in the viscous sublayer over the duct wall, and the flow-related part in the acoustic resistance formula. Numerical results reveal a linear relationship between them. Based on this, a new resistance formula is proposed, which is shown to be applicable at a certain Reynolds number under the linear acoustic excitation regime. Combined with Cummings' reactance model, a complete set of the acoustic impedance prediction formula for MPPs with grazing flow is established. Meanwhile, an inverse impedance derivation method is employed to experimentally obtain the acoustic impedance of a MPP under low-speed grazing flow within a linear acoustic excitation region. The accuracy and the superiority of the established prediction formula as compared with the existing ones are demonstrated through comprehensive comparisons with the data provided in the open literature and the measured data. It is shown that the proposed formula agrees well with the experimental data and outperforms existing models in terms of both prediction accuracy and application range.

Chapter 4. MPPs in Simple Acoustic Environment under a Grazing Flow

Typically, a MPP is backed by a cavity to form a MPP absorber as shown in Fig.4.1. The air gap between the panel and the backing wall of the cavity together with the micro holes produce the so-called Helmholtz effects, conducive to broadband noise absorption. Conventional applications of MPP absorbers consider a plane acoustic wave normally incident on an infinite MPP with an air gap of the same depth. In this case, MPPs are locally reacting and the coupling effects between the MPPs and their surrounding acoustic environment are usually ignored, thus forming a so-called simple acoustic environment. The absorption coefficient of such MPP absorber depends on multiple parameters such as the hole diameter, panel thickness, perforation ratio, cavity depth and grazing flow speed etc. Without flow, the influence of these parameters on the sound absorption coefficient has been well established. This, however, is not the case when a flow is present due to the very limited research on MPPs with grazing flow and in particular, the lack of the reliable acoustic impedance prediction tool. In this chapter, the effects of the associated system parameters on the absorption coefficient of an infinite MPP absorbers under normal acoustic excitation are revisited using the newly established acoustic impedance prediction formula with grazing flow, as shown in Fig. 4.1. The flow field that the MPPs are exposed to, in this case, can be considered as a flow in a duct with infinite width and length (high aspect ratio rectangular duct).

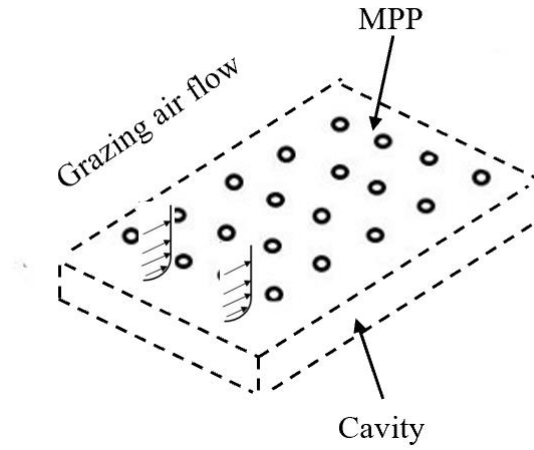


Figure 4.1. Sketch of a MPP absorber under a grazing flow.

4.1. Absorption coefficient calculations

For an infinite MPP absorber under normal acoustic excitation, without flow, the equivalent electric circuit method is employed to calculate the sound absorption coefficient as [23]:

$$\alpha = \frac{4R}{(1+R)^2 + (\chi - \cot(\omega D / c))^2} , \quad (4.1)$$

where D is the depth of the backing cavity.

By introducing the grazing flow effects on the acoustic impedance of a MPP, the sound absorption coefficient of the infinite MPP absorber under a grazing flow for the

uncoupled case, as shown in Fig.4.1, can be obtained by applying the impedance prediction formula Eq. 3.6 established in Chapter 3 considering grazing flow effects and Eq. 4.1.

4.2. Grazing flow effects

Figure 4.2 shows the effects of grazing flow on the sound absorption coefficient of the MPP absorber. Firstly, it can be observed that the absorption coefficient curves of the locally reacting MPP absorbers exhibit a bell-curve variation trend with one major peak, typical of one single degree of freedom behavior. This can be explained, since for the locally reacting case, the acoustic waves inside the backing cavity can only propagate in the direction normal to the panel. In this case, the micro holes and the backing cavity together generate the so-called Helmholtz effects and the peak is induced by the quarter-wavelength Helmholtz-type resonance in the backing cavity.

Considering the relatively simple variation trend of the absorption curve, the grazing flow effects can be described by the variations of the maximum value α_{\max} , the resonance frequency f_r and the half absorption bandwidth BW . Variations of these parameters are shown graphically in Fig. 4.2, where f_1 and f_2 are the lower and higher half-absorption frequencies, respectively. The half sound absorption bandwidth BW is defined as the frequency range between f_1 and f_2 , $BW = f_2 - f_1$. The comparison results in Fig. 4.2 clearly indicate that an increase in the

grazing flow speed shifts the absorption peak f_r to a higher frequency, while widening the absorption bandwidth BW and altering the maximum value of the absorption α_{\max} . The changes in the absorption coefficient curve are attributed to the change in both the resistance and the reactance of the MPP observed in Chapter 2, with the former one increasing and the latter one decreasing with the flow velocity. On one hand, the reduction in the reactance shifts the peak absorption to a higher frequency. On the other hand, the increase in the resistance generally yields a broader absorption band [23] and leads to the variations of the maximum absorption value.

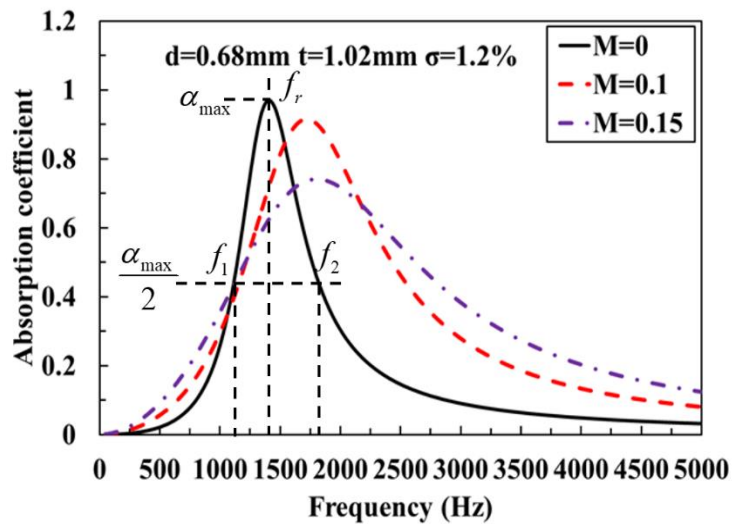


Figure 4.2. Absorption coefficient of a MPP absorber with different flow velocities.

To quantify the extent to which the grazing flow affects the absorption behavior of the locally reacting MPP absorbers in the current uncoupled simple acoustic environment, the absolute value of the difference in the absorption coefficient

maximum value α_{\max} , resonant frequency f_r and half absorption bandwidth BW between $M=0$ and other grazing flow velocities are quantified using the following definition:

$$\begin{aligned} |\alpha_{\max}^{dif}| &= |\alpha_{\max}^0 - \alpha_{\max}^M|, \\ |f_r^{dif}| &= |f_r^0 - f_r^M|, \\ |BW^{dif}| &= |BW^0 - BW^M|, \end{aligned} \quad (4.2)$$

where α_{\max}^0 , f_r^0 and BW^0 are the maximum absorption coefficient value, resonant frequency and the bandwidth of the absorption coefficient curve for $M=0$; α_{\max}^M , f_r^M , BW^M are their corresponding counterparts at other grazing flow velocities.

The above defined quantities with different hole diameters, perforation ratios and flow velocities are presented in Fig. 4.3, which describe the overall grazing flow effects in a more intuitive and comprehensive way. It is straightforward to see that for the maximum absorption value, the grazing flow mainly shows its effects when the hole size is large and the perforation ratio is low. As to the resonant frequency, the grazing flow mainly affects those panels with small holes. For the absorption bandwidth, the grazing flow mainly affects the panels with small holes and low perforation ratio. In another word, for panels with a large hole size and a low perforation ratio, the grazing flow mainly affects their maximum absorption value and for panels with small holes, the grazing flow mainly affects their resonant frequency and absorption bandwidth.

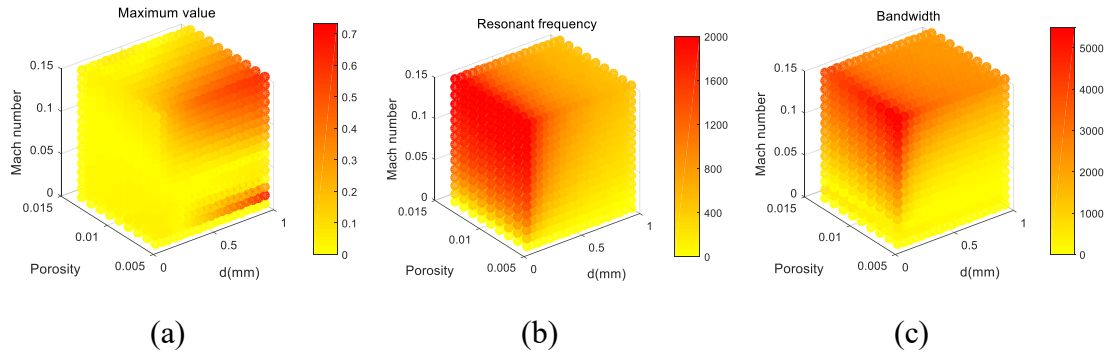


Figure 4.3. Absolute value of the difference in the maximum absorption value, resonant frequency and absorption bandwidth between no flow and other grazing flow conditions for different MPP absorbers with $t/d=1$.

The effects of the grazing flow on the absorption coefficient of MPPs with different t/d ratios are presented in Fig. 4.4. A reduced flow effects on resonant frequency and absorption bandwidth and an increased effects on the maximum absorption value with t/d ratios can be seen from these figures. Results indicate that MPPs with a small t/d ratio are more likely to be influenced by the grazing flow.

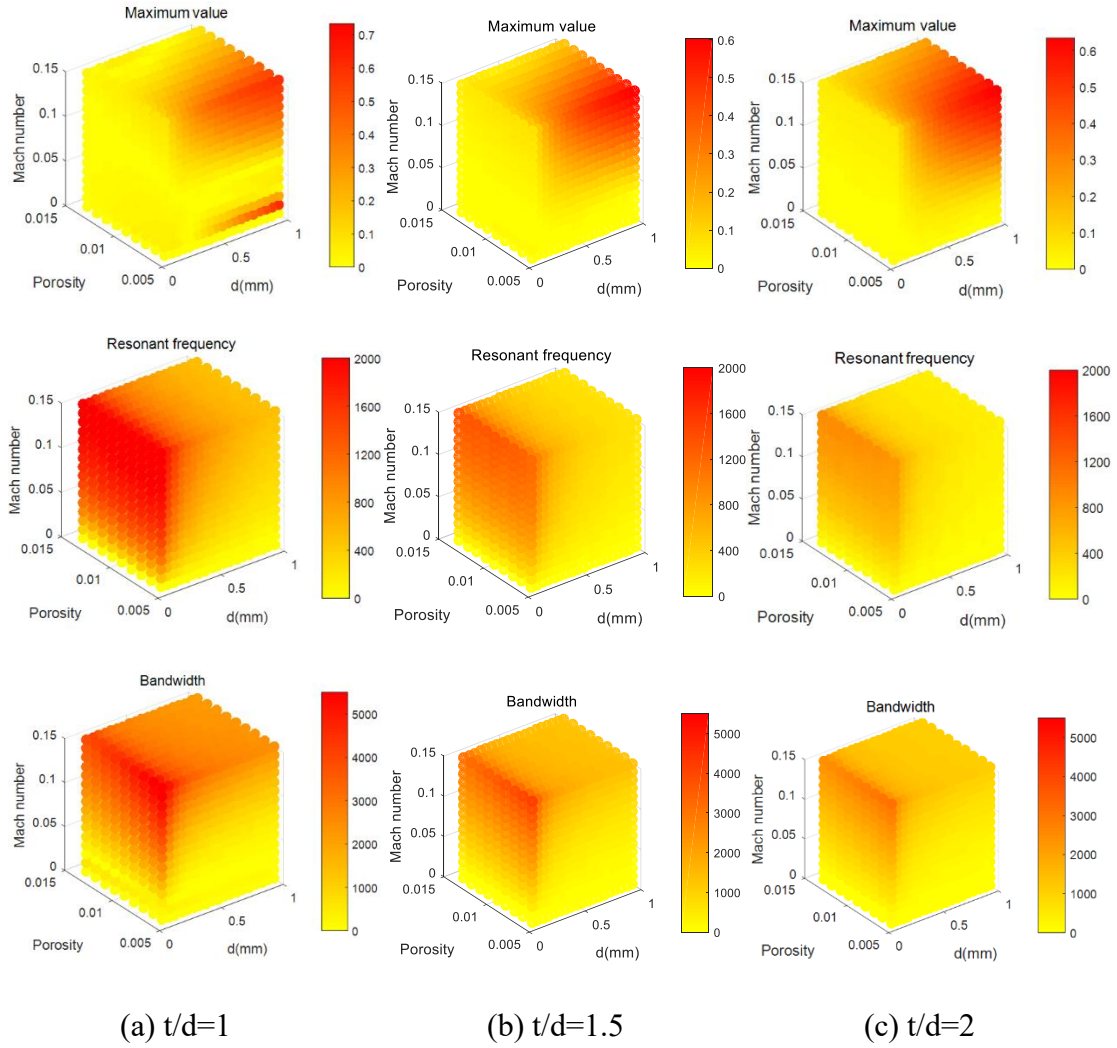


Figure 4.4. Absolute value of the difference in the maximum absorption value, resonant frequency and absorption bandwidth between no flow and other grazing flow conditions for different MPP absorbers with different t/d ratios.

4.3. Effects of the hole diameter

In the following analyses, the hole diameter and the panel thickness of MPPs are taken to be the same. In this case, to examine the influence of the MPP hole diameter

on the absorption coefficient with grazing flow, the resonant frequency f_r , maximum absorption coefficient α_{\max} and half absorption bandwidth BW of the locally reactive MPP absorbers having different hole diameters but same perforation ratio (1%) with and without grazing flow are presented in Figs 4.5-4.7.

It can be seen that, without flow, increasing the diameter of the hole shifts the resonant frequency f_r to a lower frequency; the maximum absorption coefficient α_{\max} increases first and then decreases; the half sound absorption bandwidth BW becomes narrower. With grazing flow, the same trend can be observed. These phenomena can be attributed to the fact that an increase in the hole diameter decreases the viscous effects and increases the air mass in the hole, which consequently shifts the maximum absorption to lower frequencies, narrows the absorption bandwidth and varies the maximum absorption value. As the results indicate that the panels with large holes have low resonant frequency and narrow sound absorption bandwidth with or without grazing flow, for broadband noise absorption, panels with small hole size are preferred, irrespective whether grazing flow exists or not.

These figures also show that the grazing flow effect on the maximum absorption value increases while the resonant frequency shifting decreases with hole diameters. The low flow velocity ($M=0.1$ for current case) could influence the resonant frequency and absorption bandwidth but has little effects on the maximum absorption value.

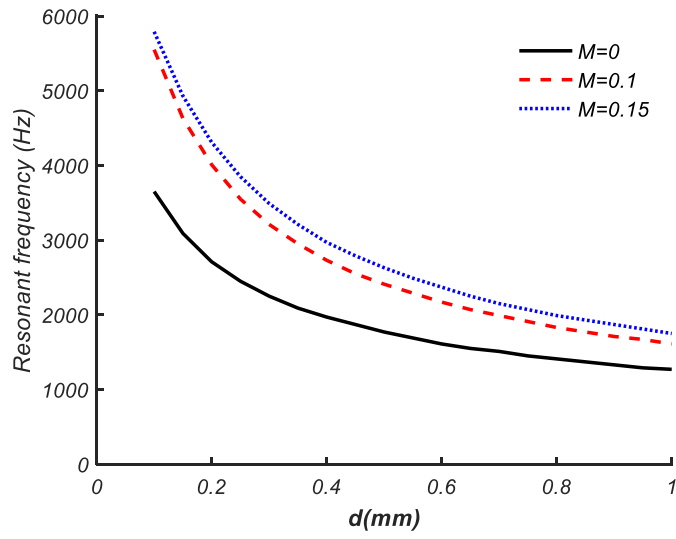


Figure 4.5. Resonant frequency of MPP absorbers with different hole diameters.

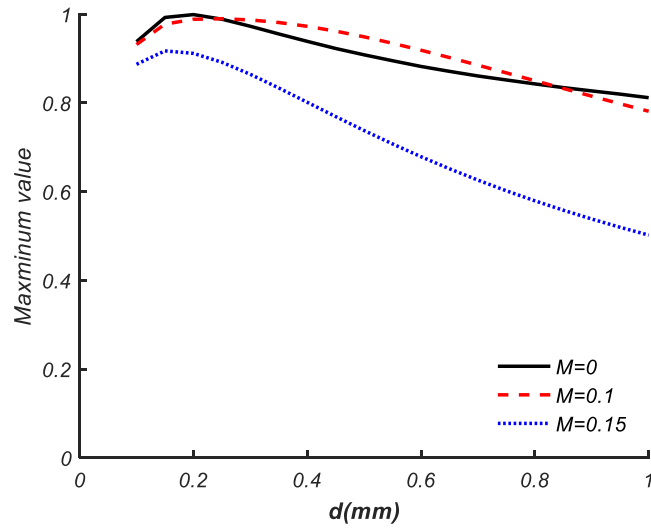


Figure 4.6. Maximum absorption coefficient of MPP absorbers with different hole diameters.

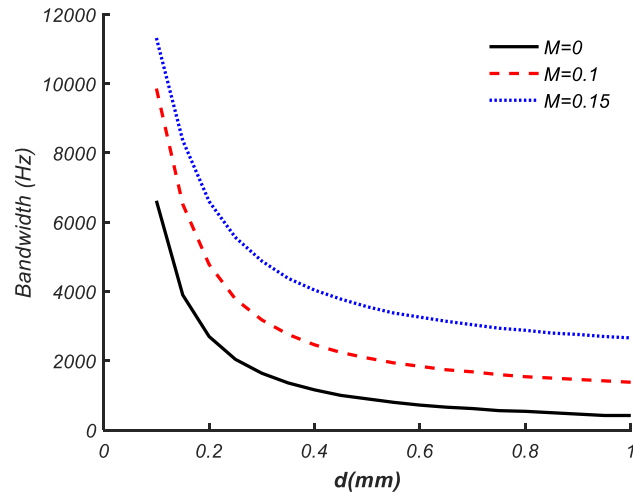


Figure 4.7. Bandwidth of MPP absorbers with different hole diameters.

4.4. Effects of the perforation ratio

The resonant frequency f_r , the maximum absorption coefficient α_{\max} and the half absorption bandwidth BW of the locally reacting MPP absorbers having different panel perforation ratios but the same hole diameters $d = 0.5\text{mm}$ with and without grazing flow are shown in Figs 4.8-4.10.

Without flow, it can be seen that, when increasing the perforation ratio, the resonant frequency of the absorber is shifted to a higher frequency, alongside a decrease in the maximum absorption value and an increase in the half sound absorption bandwidth. Thus, panels with a high perforation ratio have a high resonant frequency and a wide sound absorption bandwidth but a low maximum absorption value without grazing flow. The same trend can be seen for the resonant frequency with grazing flow. However,

different from the no-flow condition, the maximum value of the absorption coefficient increases, and the half sound absorption bandwidth remains almost constant with respect to the perforation ratio. Therefore, with the grazing flow, for panels with a high perforation ratio, both the location of the resonant frequency and the maximum absorption coefficient value are higher compared to the panels with a low perforation ratio.

These figures also show that the effects of the grazing flow on the maximum value of the absorption coefficient together with the half absorption bandwidth decrease with respect to the panel perforation ratio.

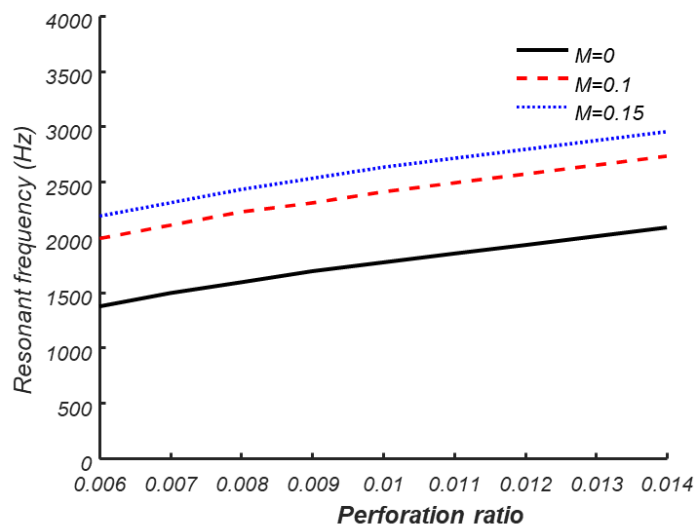


Figure 4.8. Resonant frequency of MPP absorbers with different perforation ratio.

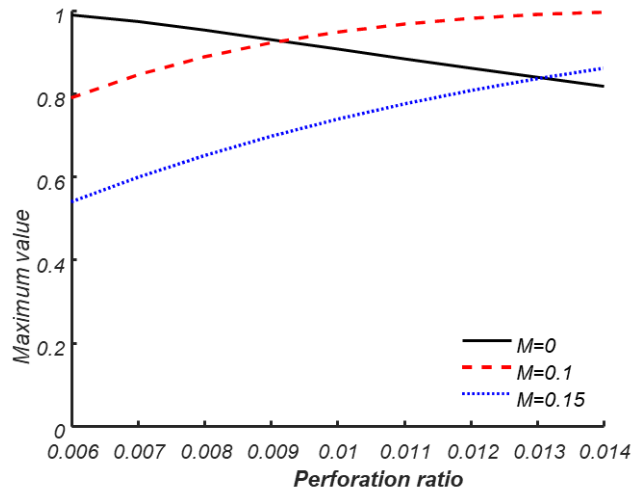


Figure 4.9. Maximum absorption coefficient of MPP absorbers with different perforation ratio.

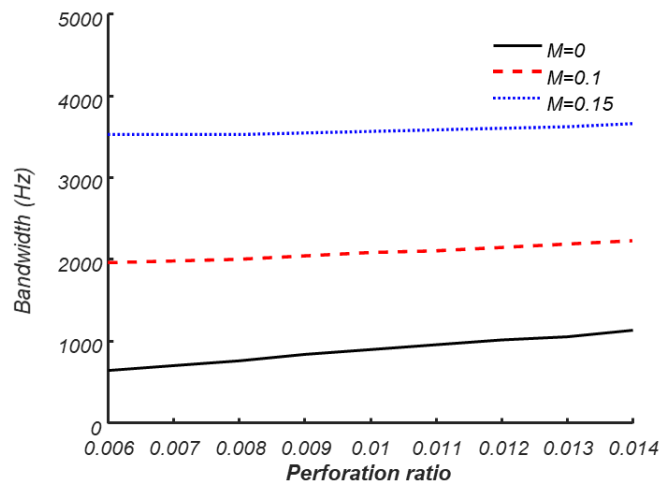


Figure 4.10. Bandwidth of MPP absorbers with different perforation ratio.

Overall speaking, the acoustic behavior of the infinite locally reacting MPPs with flow depends on the full set of MPP and flow parameters in a less intuitive manner even

in a simple uncoupled acoustic environment. The adjustment of these parameters can provide considerable rooms for the tuning of desired sound absorption performance of MPP absorbers based on need. As the grazing flow can broaden the sound absorption bandwidth, generally, with an appropriate panel thickness and perforation ratio, holes with a smaller diameter is helpful for achieving broader-band sound absorption in the presence of grazing flow.

4.5. Summary

Using the acoustic impedance prediction tools developed in the previous Chapter, the sound absorption properties of infinite locally reacting MPP absorbers are investigated. The analyses are performed by ignoring the acoustic coupling between the MPP and the surrounding environment upon assuming a normal incident acoustic excitation. The following conclusions can be drawn.

With increasing flow speed, the presence of the grazing flow affects the sound absorption coefficient curves in following ways:

- Resonant frequency (absorption peak) is shifted to a higher frequency.
- The maximum value of the absorption coefficient is varied.
- Half absorption bandwidth is broadened.
- For panels with a large hole size and a low perforation ratio, the grazing flow

mainly affects their maximum absorption value; while for panels with small holes, the grazing flow mainly affects their resonant frequency and absorption bandwidth.

- MPPs with a small t/d ratio are more likely to be influenced by the grazing flow.

Panels with a larger hole size exhibit a lower resonant frequency, a reduced maximum absorption value and a narrower sound absorption bandwidth with or without grazing flow. For broadband noise absorption, panels with a smaller hole size are preferred, irrespective whether grazing flow exists or not.

The panels with a high perforation ratio exhibit a high resonant frequency, wider sound absorption bandwidth but a lower maximum absorption value without flow. With the grazing flow, both the resonant frequency and the maximum absorption coefficient of panels with a high perforation ratio are higher compared to the panels with low perforation ratio.

Chapter 5. MPPs in Flow Ducts

The sound absorption coefficients of MPP absorbers in a relatively ideal and simple acoustic environment have been investigated in the previous Chapter 4. However, MPPs are usually coupled with the surrounding media and the coupling effects cannot be ignored as indicated by many research works [33, 51-53]. In what follows, the applications of MPPs in a coupled environment under grazing flow are investigated, aiming at providing practical guidance for the design of MPPs in applications such as flow ducts.

As one of such applications, MPPs are widely used in silencer design for duct noise control. An initial attempt to use MPPs in the duct was made by Wu [88], in which the acoustic performance of a micro-perforated panel silencer was investigated with grazing flow using theoretically derived sound attenuation prediction equations. However, due to the limitations of the assumptions made in the study, the prediction results only qualitatively agree with experiments and the discussions on the effects of silencer geometric parameters are restricted to the locally reacting case only. Recently, Allam and Abom [35, 89] investigated MPP silencers with grazing flow to show the effect of partitioning the backing cavity and that of the grazing flow without particular focus on other MPP geometrical parameters. By introducing MPPs, Wang *et al.* [100] proposed a hybrid non-locally reacting silencer, both dissipative and reactive, consisting of an expansion chamber with two side-branch cavities covered by two light

and moderately stiff MPPs, and demonstrated that, with MPPs, a wider acoustic attenuation bandwidth could be achieved compared to a flexible plate without micro-perforations. Shi *et al.* [101] investigated the acoustic attenuation of a periodically arranged array of micro-perforated tube mufflers and found that, by selecting an appropriate periodic distance, the periodic MPP silencers can be tuned for the control of lower frequency noise within a broader frequency range. Yu *et al.*[102] studied the hybrid noise attenuation mechanism of MPP silencers and analyzed the possible influences of the system parameters, without however considering the grazing flow effects like many other investigations reported in the open literature[100, 101, 103].

These works revealed useful physical insights for guiding the design of MPP silencers. However, in general, while cases without flow [100-103] have been extensively studied using classical acoustic impedance formulae proposed by Maa [23], research on MPPs in ducts considering grazing flow effects is fairly limited [35, 88, 89]. One possible explanation for the abovementioned situation is that the presence of flow inside a duct poses significant challenges. As previously reviewed in Chapter 1, due to the complex interaction between the acoustic waves and the flow field within and in the vicinity of the MPP holes, many fundamental issues arise and remain unanswered, among which is the realistic acoustic impedance prediction.

Meanwhile, MPPs in a flow duct are exposed to the surrounding acoustic environment so that the coupling of the MPPs with the duct and the backing cavity

needs to be considered. For predicting the acoustic attenuation performance of MPP silencers, the conventionally used modeling techniques face many numerical challenges. For example, one dimensional modeling techniques [88] are too simple to include these coupling effects and limited to only low-order acoustic mode propagation, while techniques like modal approach with interface matching technique [104, 105] or finite element method (FEM) [35] would become very tedious when coping with the increasing system complexity, for example, when the backing cavities are partitioned. Consequently, appropriate modeling tools are lacking and there is a need to seek more efficient and flexible prediction tools for the design of MPP silencers.

Motivated by this and capitalizing on the previously developed acoustic impedance prediction tool detailed in Chapter 3, a previously developed subsystem treatment technique, referred to as Patch Transfer Function approach (PTF) [102], is used to tackle the aforementioned numerical challenges, in the context of a flow duct. This modeling approach, in conjunction with the impedance prediction formulae established in Chapter 3, which consider the grazing flow effects, will be employed to investigate the acoustic performance of MPP silencers in a flow duct and provide guidelines for their practical design.

Following this, the principle of the PTF approach and its theoretical formulation to deal with MPP silencers with and without grazing flow are first presented. The established PTF model is then validated through comparisons with experiments in

terms of noise attenuation curves. Finally, the effects of various system parameters and the underlying physics are investigated and discussed through numerical simulations to provide guidelines for the practical design of MPP silencers in flow ducts.

5.1. Principle of the PTF approach

PTF method is a sub-structuring modelling approach [106]. Before illustrating all technical details pertinent to the PTF method, its essence is first summarized as follows.

The implementation of the PTF approach needs the global system to be firstly partitioned into several subsystems, along with the generation of the coupling interface between each pair of adjacent subsystems. Each coupling surface is then segmented into small elements, called patches. These coupling interfaces are considered to be flexible and the segmented patches on these interfaces can thus vibrate and be considered as the vibrating boundary of the corresponding subsystem. Once coupled, energy can then be transmitted from one subsystem to another through these coupling interfaces via the vibrations of the patches. Consequently, the subsystems are connected and assembled by applying the continuity condition on the patches, namely, the force balance and the velocity continuity on both sides of each patch. Previous studies [51, 106, 107] have shown that when the size of the patch is smaller than the half wavelength of the highest frequency of interest, the pressure or velocity at any given point on the patch can be reasonably approximated by the space-averaged pressure or velocity over

the patch. Considering this, the acoustic field in each subsystem can then be coupled together through patch-based interface matching technique by ensuring the dynamic balance of the mean pressure and the continuity of the normal velocity of each patch on its two sides.

Before coupling all of them together, each subsystem needs to be *a priori* characterized separately. This is achieved by calculating the so-called transfer functions between different patches, called patch transfer functions (PTFs). The patch transfer functions describe the relationship between the response on a receiving patch and the excitation on an excited patch, be it for an acoustic subsystem or a vibrating subsystem. Therefore, subsystems may comprise structural components such as flexible panels or acoustic components such as acoustic cavity or sound absorption material. For a mechanical structure, the PTFs are defined as the ratio of the mean velocity on a receiving patch over the mean force applied on an excitation patch, equivalent to patch structural mobility. For an acoustic component, the PTFs are defined as the ratio of the mean acoustic pressure on a receiving patch over the mean velocity, imposed on an excitation patch, which are the patch acoustic impedance. Upon obtaining these transfer function terms of each uncoupled subsystem, the superposition principle alongside the patch-based interface matching technique can be applied to describe the coupled system. This allows calculating the response of a global system by inverting a square symmetric matrix whose dimension corresponds to the number of patches.

The major portion of the computation incurred in the PTF approach is the calculation of the PTFs of each uncoupled subsystem. These calculations, however, are quite flexible, for which various methods can be employed depending on the subsystem. For example, when the geometry of the subsystem is regular, analytical approach can be used. For complex cases, FEM or even experimental methods can be adopted. It is relevant to recall that before all the subsystems are coupled together, the PTFs of each uncoupled subsystem are calculated separately. Benefiting from this modular nature, when optimizations are needed, only the PTFs of those subsystems subject to modifications need to be re-calculated. The patch-based interface matching technique, coarse meshing criteria ($\lambda_w / 2$), multiple options for PTF calculation and the modular nature of the method collectively empower the PTF approach with the flexibility and efficiency needed to deal with system complexity.

To further detail the implementation procedure of the PTF approach, let us consider a basic vibro/acoustic system presented in Fig. 5.1, in which two acoustic domains are connected by an elastic panel. The whole system is firstly divided into three subsystems: one elastic panel and two acoustic domains, one closed and another open. The coupling surface, occupied by the panel, is formed and segmented into N patches. The size of the patch should be smaller than the half wavelength of the highest frequency of interest, whether acoustic or structural [51, 106, 107].

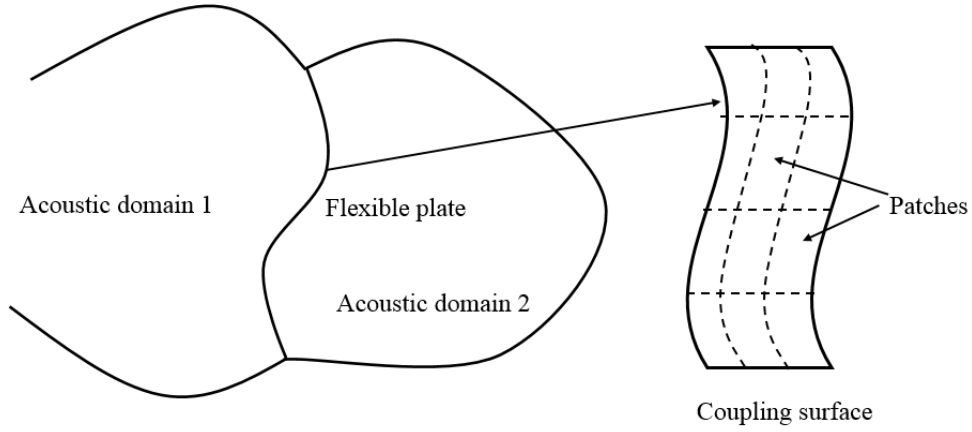


Figure 5.1. Sketch of a simple vibro/acoustic coupled system.

PTFs for each subsystem are then defined. For the vibrating structure, the PTF between patches writes,

$$Y_{re} = \frac{\bar{u}_r}{\bar{f}_e}, \quad (5.1)$$

where $\bar{u}_r = \frac{1}{S_r} \int_{S_r} u_{x,y,z} dS$ is the mean normal velocity on the receiving patch r resulted from the mean normal force excitation $\bar{f}_e = \frac{1}{S_e} \int_{S_e} f_{x,y,z} dS$ exerted on the excited patch e , while no forces being imposed on other patches, in which S_r and S_e are the surface area of the receiving and excited patch, respectively.

For the coupling surfaces in the acoustic domain, upon imposing a mean normal velocity $\bar{u}_e = \frac{1}{S_e} \int_{S_e} u_{x,y,z} dS$ on patch e , the mean acoustic pressure on the receiving patch r , $\bar{p}_r = \frac{1}{S_r} \int_{S_r} p_{x,y,z} dS$, yields the PTF between the two patches, written as,

$$Z_{re} = \frac{\bar{p}_r}{\bar{u}_e}. \quad (5.2)$$

When coupled, the mean acoustic pressure on each patch is the sum of the pressure resulted from the vibrations of all patches in this subsystem and the external pressure \bar{p}_r^{\sim} in this subsystem before coupling. Consequently, the linearity of the system finally leads to the equation below, describing the mean pressure on each patch on both sides:

$$\begin{aligned} \bar{p}_r^1 &= \bar{p}_r^{1\sim} + \sum_{e=1}^N Z_{re}^1 \bar{u}_e^1, \quad \forall r \in [1, \dots, N], \\ \bar{p}_r^2 &= \bar{p}_r^{2\sim} + \sum_{e=1}^N Z_{re}^2 \bar{u}_e^2, \quad \forall r \in [1, \dots, N]. \end{aligned} \quad (5.3)$$

Similarly, the normal force exerted on one single patch of a vibrating structure interface can result in the vibration of the patch itself and all other patches on this interface. Owing to the linearity of the system, the mean normal velocity of a single patch is thus the sum of the velocities induced by the force exerted on all the patches in the interface and the velocity $\bar{u}_r^{s\sim}$ resulted from the mechanical force exerted on this patch before coupling, which writes

$$\bar{u}_r^s = \bar{u}_r^{s\sim} + \sum_{e=1}^N Y_{re}^s \bar{f}_e^s, \quad \forall r \in [1, \dots, N]. \quad (5.4)$$

Finally, after applying the continuity condition on the patches, namely, the force

equilibrium and the normal velocity equality of each patch on its two sides, the subsystems are coupled together as

$$\begin{aligned}\bar{u}_i^1 &= \bar{u}_i^2 = \bar{u}_i^s, \quad \forall i \in [1, \dots, N], \\ \bar{f}_i^s &= (\bar{p}_i^1 - \bar{p}_i^2)S_i, \quad \forall i \in [1, \dots, N].\end{aligned}\tag{5.5}$$

Substituting Eqs. 5.3 and 5.5 into Eq. 5.4 yields

$$\bar{u}_r^1 = \bar{u}_r^{s\sim} + \sum_{e=1}^N Y_{re}^s S_e (\bar{p}_e^{1\sim} - \bar{p}_e^{2\sim}) + \sum_{e=1}^N Y_{re}^s S_e \left(\sum_j Z_{ej}^1 \bar{u}_j^1 - \sum_j Z_{ej}^2 \bar{u}_j^1 \right), \quad \forall r \in [1, \dots, N].\tag{5.6}$$

The above equation can be written in the following condensed matrix form, with \bar{u}_r^1 as unknowns:

$$U^1 = U^{s\sim} + Y^s S_e (P^{1\sim} - P^{2\sim}) + Y^s S_e (Z^1 - Z^2) U^1,\tag{5.7}$$

which can be further arranged as

$$U^1 = [I - Y^s S_e (Z^1 - Z^2)]^{-1} [U^{s\sim} + Y^s S_e (P^{1\sim} - P^{2\sim})],\tag{5.8}$$

where I is an $N \times N$ identity matrix. Upon solving Eq.5.8, the unknown patch velocities can be obtained. The acoustic pressure and other quantities can then be obtained based on the calculated patch velocities.

5.2. PTF calculations of conventional subsystems

In this section, the detailed formulation of the PTFs for several typical subsystems used in this thesis is summarized, including acoustic cavity, semi-infinite duct and MPP.

5.2.1 PTFs of an acoustic cavity

For a 3D rectangular cavity, shown in Fig. 5.2, based on the classical modal-decomposition theory, the acoustic pressure in the cavity can be written as

$$p(x, y, z) = \sum_i a_i \phi_i, \quad (5.9)$$

where a_i is the i th modal amplitude of the cavity and ϕ_i the corresponding i th mode shape function. The following rigid-walled acoustic mode shape function is used:

$$\phi_i(x, y, z) = \cos\left(\frac{r_x \pi}{L_x} x\right) \cos\left(\frac{r_y \pi}{L_y} y\right) \cos\left(\frac{r_z \pi}{L_z} z\right), \quad r_x, r_y, r_z = 0, 1, 2, \dots, \quad (5.10)$$

where L_x , L_y and L_z are the side lengths of the 3D rectangular cavity

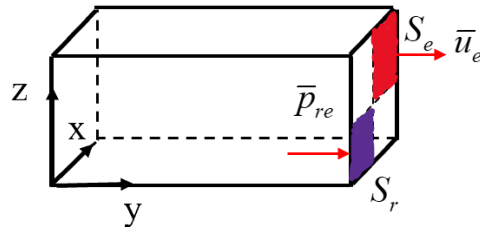


Figure 5.2. A 3D rectangular cavity with a vibrating boundary \bar{u}_e .

The distribution of the pressure field inside the cavity is governed by the Helmholtz equation:

$$\nabla^2 p + k^2 p = 0, \quad (5.11)$$

in which $k = \frac{\omega}{c}$ is the wave number; ω the angular velocity and c the sound speed.

The pressure field inside the cavity having a boundary S_c excited by one single vibration patch with a mean normal velocity \bar{u}_e can be described by the Green's function as

$$\int_{\Omega} (p \nabla^2 \phi_i - \phi_i \nabla^2 p) dV = \int_{S_c} \left(p \frac{\partial \phi_i}{\partial n} - \phi_i \frac{\partial p}{\partial n} \right) dS_c. \quad (5.12)$$

According to the momentum equation, the following boundary equations can be prescribed for the excited vibration patch and the rest of rigid surfaces, respectively.

$$\frac{\partial p}{\partial n} = -j\rho\omega\bar{u}_e, \quad (5.13)$$

$$\frac{\partial p}{\partial n} = 0, \quad (5.14)$$

where ρ is the density of the acoustic medium.

After substituting Eqs. 5.9, 5.11, 5.13 and 5.14 into Eq. 5.12 and applying the

modal orthogonality, the following equation can be derived:

$$a_i(k^2 - k_i^2)\Lambda_i = \int_{S_e} j\rho\omega\bar{u}_e\phi_i dS_e, \quad (5.15)$$

where $\Lambda_i = \int_{\Omega} \phi_i^2 dV_c$.

Substituting Eq. 5.15 into Eq. 5.9, the sound pressure field in the cavity is then obtained as

$$p(x, y, z) = \sum_i \frac{j\omega\rho}{\Lambda_i(k^2 - k_i^2)} \phi_i(x, y, z) \int_{S_e} \bar{u}_e \phi_i(x, y, z) dS_e. \quad (5.16)$$

Subsequently, the mean pressure on a receiving patch \bar{p}_{re} resulted from the vibration of one particular excitation patch is

$$\bar{p}_{re} = \bar{u}_e \sum_i \frac{j\omega\rho}{\Lambda_i(k^2 - k_i^2) S_r S_r} \int_{S_r} \phi_i(x, y, z) dS_r \int_{S_e} \phi_i(x, y, z) dS_e. \quad (5.17)$$

According to Eq. 5.2 the PTF between patches in the cavity is

$$Z_{re} = \sum_i \frac{j\omega\rho}{\Lambda_i(k^2 - k_i^2) S_r S_r} \int_{S_r} \phi_i(x, y, z) dS_r \int_{S_e} \phi_i(x, y, z) dS_e. \quad (5.18)$$

5.2.2 PTFs of a semi-infinite duct

In a semi-infinite duct with a rectangular cross-section sketched in Fig 5.3, the sound pressure at the end of the duct ($y = 0$) can be expressed as

$$p_d(x, z) = \sum_i a_i^d \phi_i^d, \quad (5.19)$$

where a_i^d is the i th modal amplitude of the duct; ϕ_i^d the corresponding i th mode shape function expressed as

$$\phi_i^d(x, z) = \cos\left(\frac{r_x^d \pi}{L_x^d} x\right) \cos\left(\frac{r_z^d \pi}{L_z^d} z\right), \quad r_x^d, r_z^d = 0, 1, 2, \dots, \quad (5.20)$$

where L_x^d and L_z^d are the side lengths of the duct.

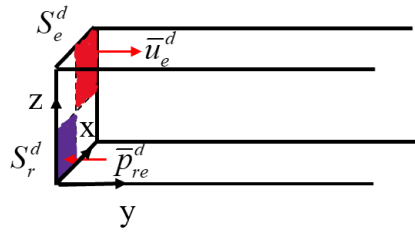


Figure 5.3. A rectangular semi-infinite duct with a vibrating boundary \bar{u}_e .

Assuming an excited patch at the end of the duct ($y = 0$) vibrating with the mean normal velocity \bar{u}_e^d , the modal amplitude can be calculated as [108],

$$a_i^d = \rho c \sum_i \frac{1}{N_i^d \sin \theta} \int_{S_e^d} \bar{u}_e^d \phi_i^d dS_e^d, \quad (5.21)$$

where S_e^d is the surface area of the excited patch in the duct; $N_i^d = \int_{S_e^d} \phi_i^d \phi_i^d dS_e^d$ and the modal phase angle

$$\sin \theta = -j \sqrt{\frac{\left[\left(r_x^d \pi / L_x^d \right)^2 + \left(r_z^d \pi / L_z^d \right)^2 \right]}{(\omega / c)^2}} - 1. \quad (5.22)$$

According to Eq. 5.19, the radiated sound pressure at the end of the duct excited by the vibration of a particular patch can then be written as

$$p_d(x, z) = \rho c \sum_i \frac{1}{N_i^d \sin \theta} \phi_i^d \int_{S_e^d} \bar{u}_e^d \phi_i^d dS_e^d. \quad (5.23)$$

The space averaged pressure on one receiving patch \bar{p}_{re}^d at the end of the duct resulted from the vibration of one particular excitation patch is

$$\bar{p}_{re}^d = \bar{u}_e^d \rho c \sum_i \frac{1}{N_i^d S_r^d \sin \theta} \int_{S_r^d} \phi_i^d dS_r^d \int_{S_e^d} \phi_i^d dS_e^d. \quad (5.24)$$

Therefore, the PTF between a receiving patch and an excitation patch in the semi-infinite duct, according to the definition defined in Eq. 5.2, can be written as,

$$Z_{re}^d = \rho c \sum_i \frac{1}{N_i^d S_r^d \sin \theta} \int_{S_r^d} \phi_i^d dS_r^d \int_{S_e^d} \phi_i^d dS_e^d. \quad (5.25)$$

5.2.3 PTFs of the MPP

Considering a flexible micro-perforated panel, the pressure difference across the panel, $p_1 - p_2$, generates the vibration of the air in the hole with a velocity u_h and the panel with a velocity u_p as shown in Fig. 5.4. Given the dimension of the hole is much smaller than the acoustic and flexural wavelengths of interests, the mean MPP vibration velocity can be approximated by [51]:

$$u_{MPP} = (1 - \delta)u_p + \delta u_h. \quad (5.26)$$

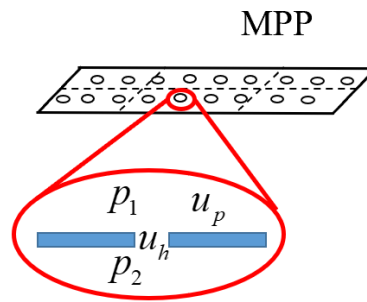


Figure 5.4. Pressure and velocity description for a MPP.

The viscous force in the hole along with the inertial force due to the air motion in the hole, contribute to the pressure difference across the MPP. Considering the vibration of the panel, the viscous force depends on the relative motion between the air in the hole and the structure, $u_h - u_p$. Therefore, one can write [51]:

$$\Delta p = p_1 - p_2 = \text{Re}\{Z_h\}(u_h - u_p) + j \text{Im}\{Z_h\}u_h, \quad (5.27)$$

where $\text{Re}\{\}$ and $\text{Im}\{\}$ denote the real and imaginary parts of the hole impedance. Without flow, the formulae established by Maa [23] are used to calculate the hole impedance Z_h , while in the presence of grazing flow, the formulae developed in Chapter 3 are adopted.

The vibration velocity of the panel is expressed as:

$$u_s = Y_p f_p = Y_p \Delta p S_{patch}^{MPP} (1 - \delta), \quad (5.28)$$

where Y_p is the mobility of the MPP plate base and S_{patch}^{MPP} the surface area of the segmented patch.

From Eqs. 5.26-5.28, the PTF between patches for MPP, Y_{MPP} , can be written according to Eq. 5.1 as,

$$Y_{MPP} = \frac{u_{MPP}}{\Delta p S_{patch}^{MPP}} = (1 - \delta) \left[(1 - \delta) + \delta \frac{\text{Re}\{Z_h\}}{Z_h} \right] Y_p + \frac{\delta}{Z_h S_{patch}^{MPP}}. \quad (5.29)$$

It can be seen that for a rigid MPP, $Y_p = 0$, the PTFs of the MPP retreats to:

$$Y_{MPP} = \frac{\delta}{Z_h S_{patch}^{MPP}}. \quad (5.30)$$

5.3. Formulations of the flow duct problem

The system under investigation is illustrated in Fig. 5.5. A MPP, backed by an acoustic cavity, is flush-mounted on one wall of a flow duct with a rectangular cross section. The PTF approach is employed here to simulate the acoustic behavior of this MPP silencer with and without grazing flow. In the present case, only low speed flow is considered. Therefore, the grazing flow effects are only incorporated into the acoustic impedance of MPPs and the convective effects of the flow on the wave propagation in the duct are neglected [35]. Based on the principle of the PTF approach, separated by the coupling surfaces C1, C2 and C3, the whole system is divided into five subsystems, namely, an inlet duct, a main cavity, an outlet duct, an MPP and a side branch cavity, as shown in Fig. 5.6. Each side of a coupling surface belongs to a different subsystem. Taking the coupling surface C3, occupied by the MPP, as an example, its upper side, donated as MC_3 , belongs to the main cavity while the lower side SC_3 belongs to the side branch cavity. Each coupling surface is then meshed and divided into patches, according to the half-wavelength rule described above[51, 106, 107].

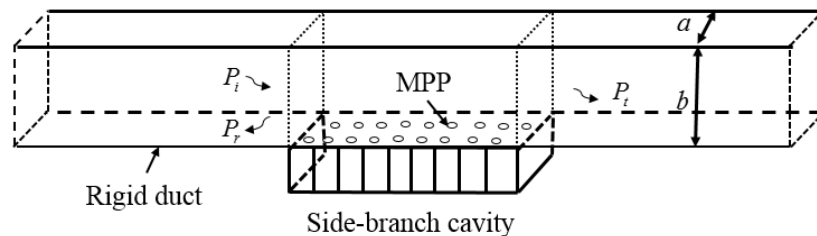


Figure 5.5. Sketch of the investigated flow duct system.

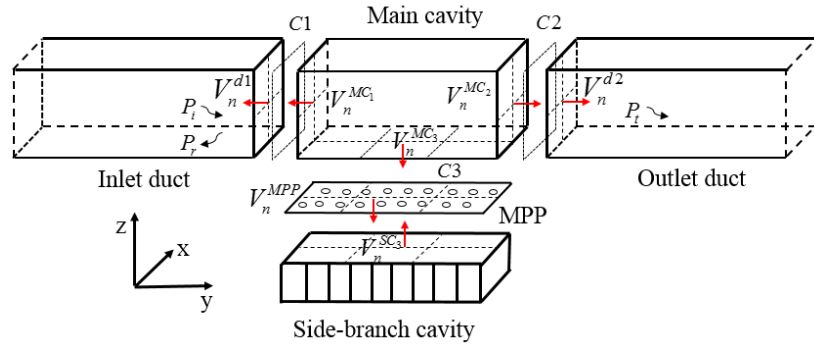


Figure 5.6. Sub-system treatment by using PTF approach.

The calculations of the PTFs of each subsystem, before it is coupled to the adjacent subsystems, are carried out. Both the main cavity and the side branch cavity without partition can be modeled as a 3D rectangular cavity using classical modal approach. The PTFs of these two subsystems are calculated by using Eq. 5.18. As to the rectangular inlet and outlet ducts, their PTFs can be obtained by using Eq. 5.25. In the current case, the vibration of the MPP is not considered, thus Eq. 5.30 is used for its PTF calculation.

After applying the continuity condition on the connecting patches of three coupling surfaces, namely the force balance of each patch and the equality of the normal velocity, the five divided individual subsystems are finally coupled together.

The force equilibrium of the patches at interface 1, 2 and 3 leads to the following expressions:

$$\bar{P}_1^{-d1} + \sum_e^{N_1} Z_{re}^{d1d1} \bar{u}_e^{d1} = \sum_e^{N_1} Z_{re}^{MC_1MC_1} \bar{u}_e^{MC_1} + \sum_e^{N_2} Z_{re}^{MC_1MC_2} \bar{u}_e^{MC_2} + \sum_e^{N_3} Z_{re}^{MC_1MC_3} \bar{u}_e^{MC_3} ,$$

$\forall r \in [1, \dots, N_1]$ at interface 1,

$$\sum_e^{N_2} Z_{re}^{d2d2} \bar{u}_e^{d2} = \sum_e^{N_1} Z_{re}^{MC_2MC_1} \bar{u}_e^{MC_1} + \sum_e^{N_2} Z_{re}^{MC_2MC_2} \bar{u}_e^{MC_2} + \sum_e^{N_3} Z_{re}^{MC_2MC_3} \bar{u}_e^{MC_3} ,$$

$\forall r \in [1, \dots, N_2]$ at interface 2,

$$\sum_e^{N_3} Y_{re}^{MPP} S_e \left(\sum_j^{N_1} Z_{ej}^{MC_3MC_1} \bar{u}_j^{MC_1} + \sum_j^{N_2} Z_{ej}^{MC_3MC_2} \bar{u}_j^{MC_2} + \sum_j^{N_3} Z_{ej}^{MC_3MC_3} \bar{u}_j^{MC_3} - \sum_j^{N_3} Z_{ej}^{SC_3SC_3} \bar{u}_j^{SC_3} \right) = \bar{u}_r^{MPP} ,$$

$\forall r \in [1, \dots, N_3]$ at interface 3, (5.31)

where N_1 , N_2 and N_3 are the total number of patches at the coupling interfaces 1, 2 and 3, respectively.

The equality of the normal velocity on each side of the patches at the three coupling interfaces writes:

$$\bar{u}_{n_1}^{-d1} = \bar{u}_{n_1}^{MC_1} , \quad \forall n_1 \in [1, \dots, N_1] \text{ at interface 1,}$$

$$\bar{u}_{n_2}^{-d2} = \bar{u}_{n_2}^{MC_2} , \quad \forall n_2 \in [1, \dots, N_2] \text{ at interface 2,}$$

$$\bar{u}_{n_3}^{-MC_3} = \bar{u}_{n_3}^{MPP} = -\bar{u}_{n_3}^{SC_3} , \quad \forall n_3 \in [1, \dots, N_3] \text{ at interface 3.} \quad (5.32)$$

The above equations can then be written in the following condensed matrix form:

$$P^{-d1} + Z^{d1d1} V_n^{d1} = Z^{MC_1MC_1} V_n^{MC_1} + Z^{MC_1MC_2} V_n^{MC_2} + Z^{MC_1MC_3} V_n^{MC_3} ,$$

$$Z^{d2d2} V_n^{d2} = Z^{MC_2MC_1} V_n^{MC_1} + Z^{MC_2MC_2} V_n^{MC_2} + Z^{MC_2MC_3} V_n^{MC_3} ,$$

$$Y^{MPP} S_e \left(Z^{MC_3MC_1} V_n^{MC_1} + Z^{MC_3MC_2} V_n^{MC_2} + Z^{MC_3MC_3} V_n^{MC_3} - Z^{SC_3SC_3} V_n^{SC_3} \right) = V_n^{MPP} ,$$

$$\begin{aligned}
V_n^{MC_1} &= V_n^{d1}, \\
V_n^{MC_2} &= V_n^{d2}, \\
V_n^{MC_3} &= V_n^{MPP} = -V_n^{SC_3}.
\end{aligned} \tag{5.33}$$

Equation 5.33 can be further condensed into the following form,

$$\{\mathbf{Z}\}\{\mathbf{V}\} = \{\mathbf{F}\}, \tag{5.34}$$

$$\text{where, } \mathbf{Z} = \begin{bmatrix} Z^{MC_1MC_1} - Z^{d1d1} & Z^{MC_1MC_2} & Z^{MC_1MC_3} \\ Z^{MC_2MC_1} & Z^{MC_2MC_2} - Z^{d2d2} & Z^{MC_2MC_3} \\ Y^{MPP} S_e Z^{MC_3MC_1} & Y^{MPP} S_e Z^{MC_3MC_2} & Y^{MPP} S_e (Z^{MC_3MC_3} + Z^{SC_3SC_3}) - I \end{bmatrix},$$

$$\mathbf{V} = \begin{bmatrix} V_n^{MC_1} \\ V_n^{MC_2} \\ V_n^{MC_3} \end{bmatrix} \text{ and } \mathbf{F} = \begin{bmatrix} P^{-d1} \\ 0 \\ 0 \end{bmatrix}.$$

If the side branch cavity is to be partitioned into smaller cavities, as shown in Fig. 5.6, the case can be seen as a combination of multiple unit cells, each comprising an MPP facing and an acoustic backing cavity. Assuming the unit cells are well separated from each other by solid partition walls, the side branch mobility Y^{MPP} and impedance $Z^{SC_3SC_3}$ can be constructed by combing all the unit cells as a common subsystem as [102]:

$$Y^{MPP} = \begin{bmatrix} Y_1^{MPP} & & & & \\ & Y_2^{MPP} & & & \\ & & Y_i^{MPP} & & \\ & & & \ddots & \\ & & & & \ddots \end{bmatrix},$$

amplitude of the incidence wave; V_2 and P_2 are the normal velocity and the sound pressure at interface 2; S_1 and S_2 are the total surface area of interface 1 and 2 and the superscript * represents the complex conjugate.

The sound reflection coefficient R_{ef} is defined as the ratio between the reflected sound power at interface 1, Π_r , and the incidence sound power, Π_{in} , which writes,

$$R_{ef} = \frac{\Pi_r}{\Pi_{in}} = \frac{\Pi_{in} - \Pi_t^1}{\Pi_{in}}, \quad (5.39)$$

where Π_t^1 is the transmitted sound power through interface 1, calculated by:

$$\Pi_t^1 = \frac{1}{2} \int_{S_1} \text{Re} \{ P_1 \times V_1^* \} dS_1, \quad (5.40)$$

in which V_1 and P_1 are the normal velocity and the sound pressure at the interface 1, respectively.

The sound absorption coefficient α is defined as the fraction of the sound power absorbed by the MPP absorber when an incidence plane wave propagates through the duct, which writes

$$\alpha = \frac{\Pi_t^1 - \Pi_{out}}{\Pi_{in}}. \quad (5.41)$$

5.4. Experimental validations

Experiments are first conducted to validate the PTF model and the implemented calculation scheme. The TL is measured by using the four-microphone-two-source method [109]. The same microphone (one downstream microphone, microphone 3) is used as reference for both upstream and downstream excitations. To ensure a good measurement quality, the signal from the reference microphone should be strong enough. However, it was observed that this can hardly be achieved when the acoustic source is put on the upstream the sample [109]. To tackle this problem, modifications proposed in [110] are adopted: for upstream source, microphones 1 or 2 is used as reference, while for downstream source, microphones 3 or 4 is used. Thus when microphone 1 is used as the reference, the transfer functions in reference [109] should be changed as follows, $H_{13} = 1/H_{31}$, $H_{23} = H_{21}/H_{31}$ and $H_{43} = H_{41}/H_{31}$. The sound absorption coefficient α can then be obtained through the following equations:

$$\alpha = \frac{\Pi_{in}^{\text{exp}} - \Pi_{out}^{\text{exp}} - \Pi_r^{\text{exp}}}{\Pi_{in}^{\text{exp}}}, \quad (5.42)$$

where

$$\Pi_{in}^{\text{exp}} = \frac{|p_i^{\text{exp}}|^2}{2\rho c} S_{duct}, \quad (5.43)$$

$$\Pi_r^{\text{exp}} = \frac{|p_r^{\text{exp}}|^2}{2\rho c} S_{duct}, \quad (5.44)$$

are the measured incident and reflected sound power in the inlet duct, respectively. In

Eqs. 5.43 and 5.44, S_{duct} is the cross-section area of the duct; $|p_i^{exp}|$ and $|p_r^{exp}|$ are the measured pressure amplitude of the incident and reflected wave in the inlet part of the duct, which can be obtained from two upstream microphones (M1 and M2 in Fig. 5.7) by using model-decomposition method. Π_{out}^{exp} is the measured transmitted sound power, which can be derived by using the following equation according to the definition of the TL.

$$\Pi_{out}^{exp} = \frac{\Pi_{in}^{exp}}{10^{TL/10}} \cdot \quad (5.45)$$

The experimental setup is sketched in Fig. 5.7. The cross section of the duct is 100 x 100 mm with a cut-on frequency of 1700 Hz. Four 1/4-inch. microphones are used here with two of them flush-mounted upstream the silencer and the two others flushed mounted in the downstream segment. The separation distance between the microphones is shown in Fig. 5.7.

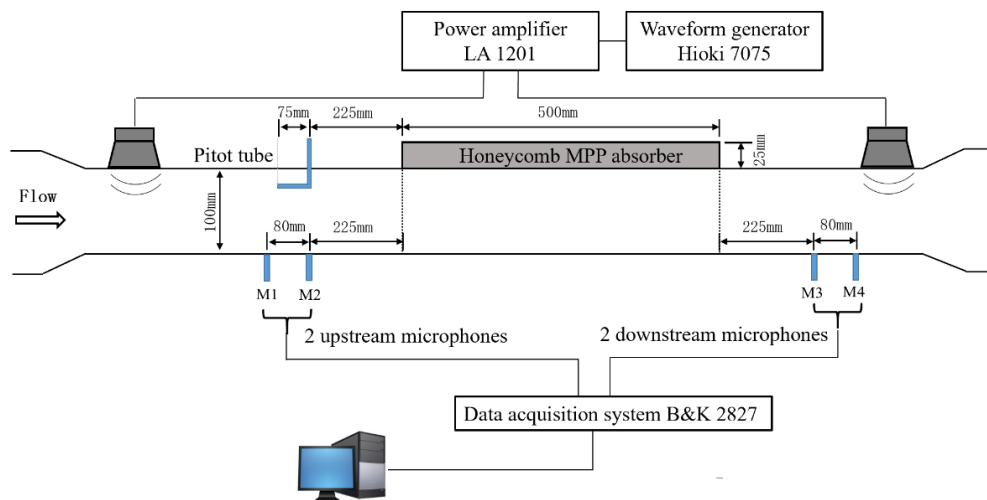


Figure 5.7. Sketch of the experimental setup.

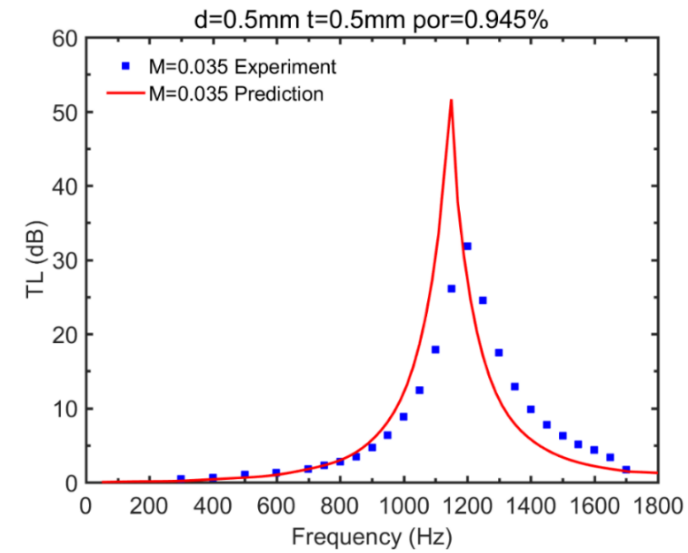
The test sample, shown in Fig. 5.8, is a single layer MPP backed by a honeycomb structure with a thickness of 25 mm, forming a honeycomb MPP silencer. The aluminum MPP is 100mm wide and 500mm long, with a perforation ratio of 0.945%. The diameter of the perforated hole and the thickness of the MPP are both 0.5mm.



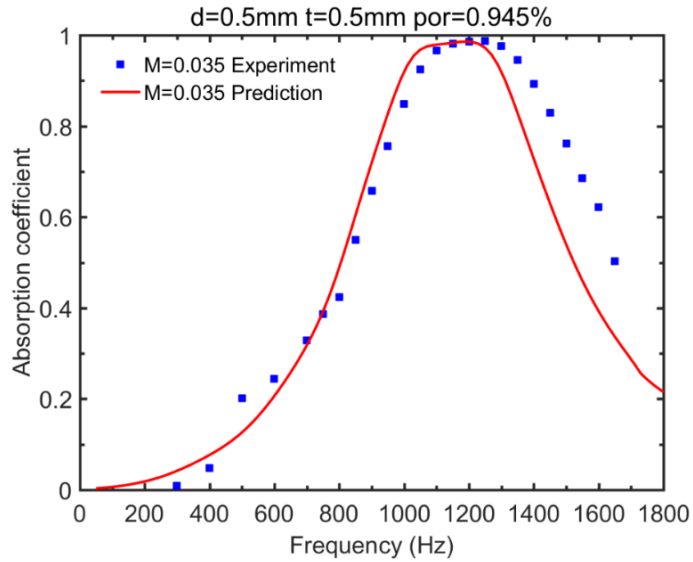
Figure 5.8. Test sample.

The accuracy of the PTF calculation is validated through comparisons with the measured data. The TL and the sound absorption coefficient of the honeycomb MPP silencer under various grazing flow velocities are presented and compared in Figs. 5.9-5.11. The comparison shows that the prediction results fit the experimental data reasonably well with a good agreement between them at various flow speeds in terms of the TL, absorption curve bandwidth as well as the location of their peak frequencies. The observed deviations of the predicted maximum values from the measured ones are mainly due to the venerable signal to noise ratio. Since with the presence of the flow, the background noise is increased due to the flow-induced noise. As the level of the imposed acoustic excitation should be limited to ensure the linear behavior of the MPP, the signal to noise ratio becomes worse. Therefore, the predicted high TL cannot be

measured during experiments. Nevertheless, overall speaking, the above validations confirm the validity of the PTF approach.



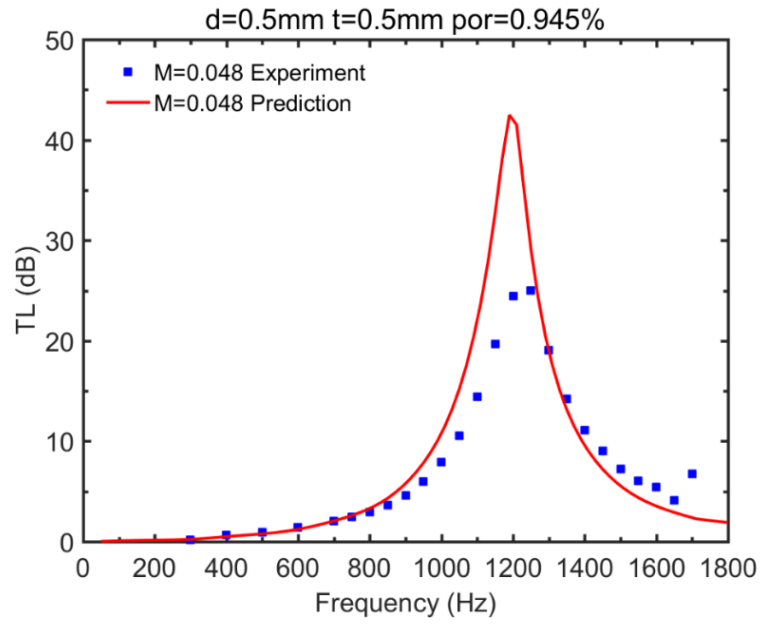
(a)



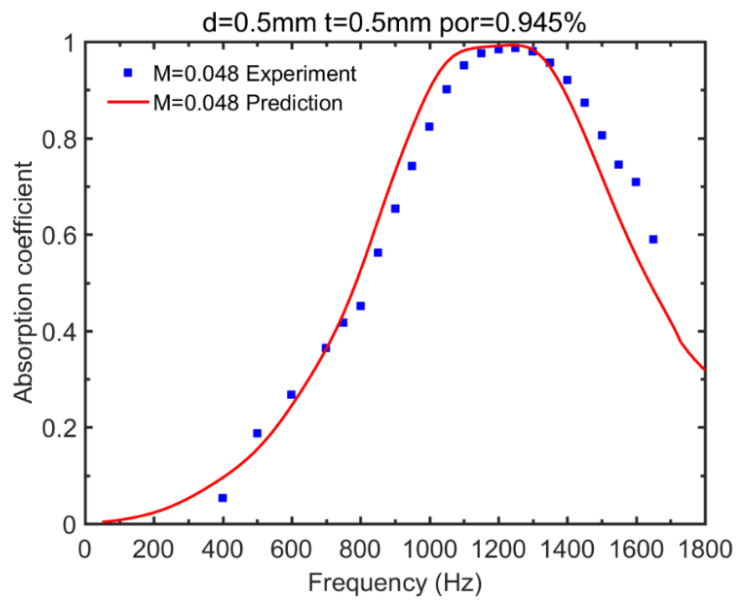
(b)

Figure 5.9. Comparisons between predictions and the experimental data at

$M = 0.035$, (a) TL, (b) sound absorption coefficient.



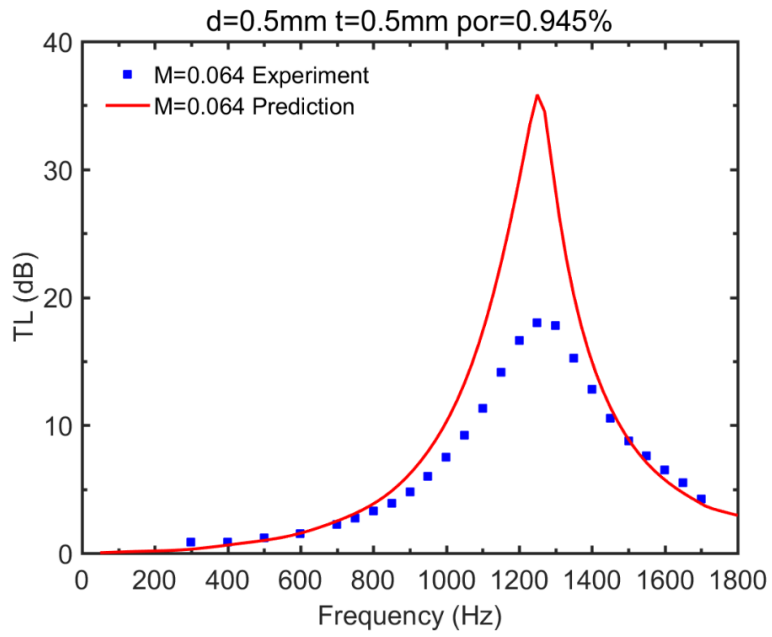
(a)



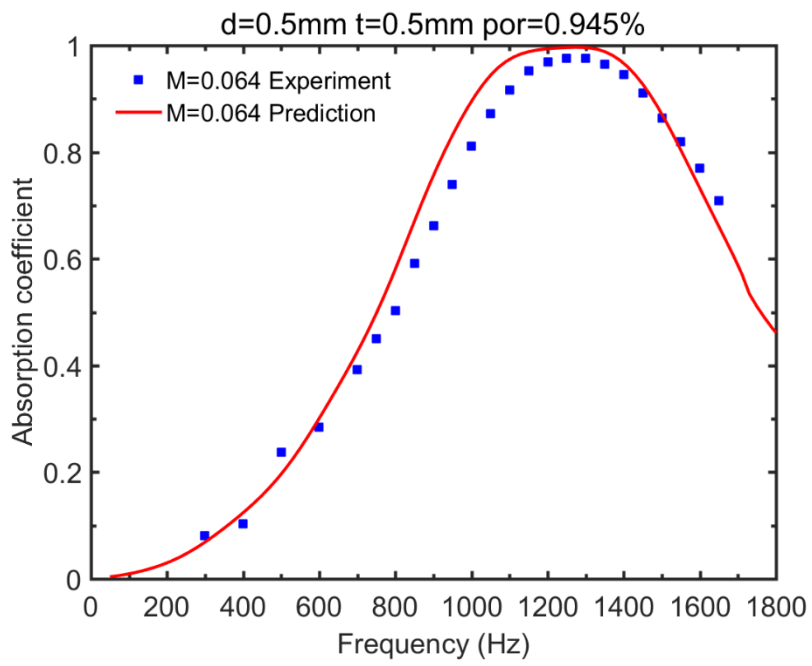
(b)

Figure 5.10. Comparisons between prediction and the experimental data at

$M = 0.048$, (a) TL, (b) sound absorption coefficient.



(a)



(b)

Figure 5.11. Comparisons between prediction and the experimental data at

$M = 0.064$, (a) TL, (b) sound absorption coefficient.

5.5. Numerical results and analyses

To gain understanding on the sound attenuation mechanism of the MPP silencers and provide guidelines for their design in flow ducts, various issues such as the influences of the flow velocities, solid partition arrangements in the backing cavity, panel dimensions, perforation ratios and hole diameters are investigated. By employing the validated PTF approach, their effects on the acoustic attenuation performance of MPPs in flow ducts are scrutinized. In the analyses, the hole diameter and panel thickness of MPPs are taken to be the same. The dimension of the investigated system (Fig. 5.5) is the same as the one used in experiment, described in Fig. 5.7.

5.5.1. Grazing flow effects

The TL curves of a non-partitioned MPP silencer under different flow velocities are compared in Fig. 5.12. A typical TL curve is first taken for analyses, for example, $M = 0.05$. It can be seen that for the non-partitioned case, several dips and peaks appear in the TL curves, resulting in relatively low peak value but broadband acoustic attenuation. The peaks on the TL curve are due to the coupling of the MPP with the backing cavity and main duct system, with their locations corresponding to the coupled system natural frequencies. With grazing acoustic wave incidence, the axial or grazing modes of the backing cavity are activated, which finally give rise to the appearance of these dips [28]. These axial modes occur at frequencies corresponding to $f_{A,n} = nc / 2L$, with L being the length of the backing cavity in the axial direction (500 mm in the

present configuration) and n corresponding to the number of half-wavelengths span the length of the backing cavity. The sound pressure distribution inside the silencer at one selected dip on the TL curve, at $M=0.05$ and $f = f_{A,4} = 1377\text{Hz}$, around one axial mode of the backing cavity, is presented in Fig. 5.13. It can be seen that the sound pressure features four nodal planes in the backing cavity, corresponding to four half-wavelengths. Meanwhile, the axial locations of these nodal planes in the backing cavity are coincident with those in the main duct. Consequently, the pressure across the MPP is almost the same and in-phase, thus resulting small pressure difference across the MPP. Under this circumstance, the vibration velocity of the air inside the hole of the MPP is trivial and eventually neutralized as expected, thus annulling possible energy dissipation, since the acoustic energy can only be dissipated by the vibration of the air inside the hole. In the present case, the MPP can hardly provide any sound energy dissipation. To enable effective MPP energy dissipation, the panel should be put into an acoustic environment with significant acoustic pressure difference across the MPP.

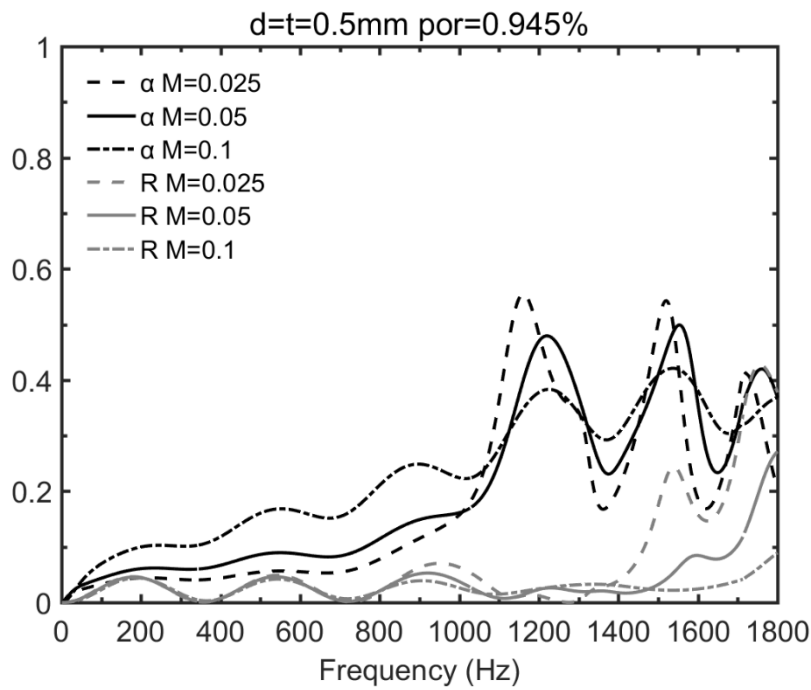
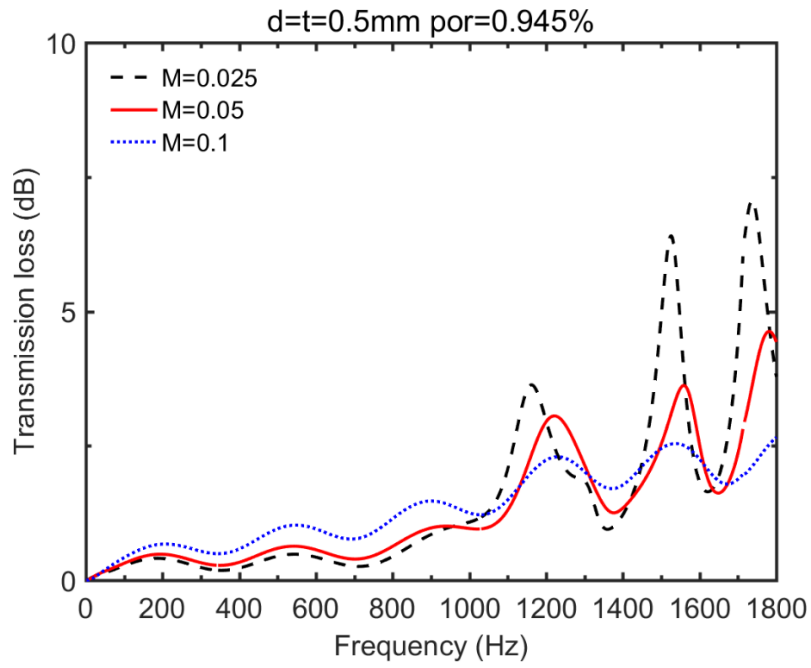


Figure 5.12. Silencing performance of MPP silencers without solid partitions under different flow velocities. (a) TL, (b) sound absorption and reflection coefficient.

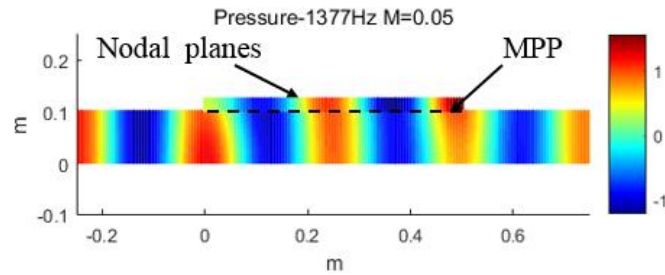


Figure 5.13. Sound pressure distribution inside the MPP silencer without solid partitions at $f = 1377$ Hz and $M = 0.05$.

The comparison in Fig. 5.12a also indicates that the presence of the grazing flow enhances the sound attenuation performance below roughly 1000 Hz. However, above this frequency, the grazing flow lifts up the troughs, smooths out the peaks while shifts them to higher frequencies, and finally results in a more flattened TL curve. It should be noted that the locations of the troughs do not seem to be affected by the grazing flow. As illustrated before, the troughs on the TL curves are due to the standing waves in the backing cavity occurred at axial resonance frequencies, which depend only on the axial length of the backing cavity, thus the flow cannot affect the locations of the troughs. As the peaks are induced by the coupling in the duct system, and the grazing flow alters the impedance of the MPP and thus the coupling effects, variations in the peak values and peak locations are thus observed.

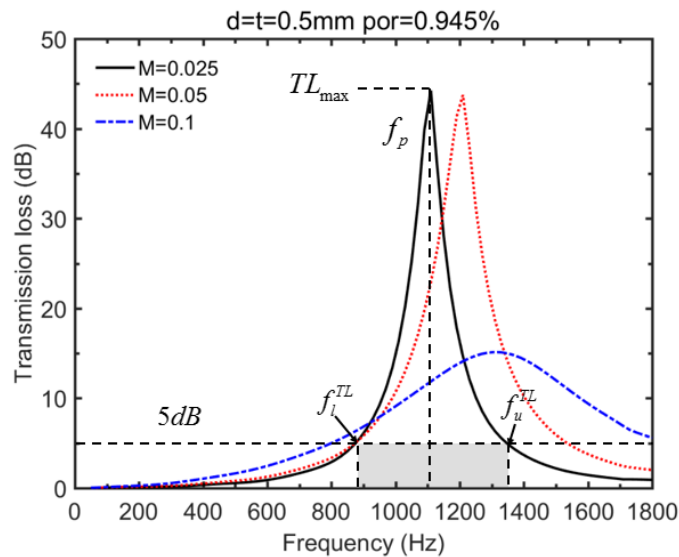
To better understand the underlying physical phenomena, the associated sound

absorption and reflection coefficient curves are plotted in Fig. 5.12b. It can be seen that both dissipation and reflection effects contribute to the observed overall sound attenuation. The acoustic attenuation mechanism of this non-partitioned MPP silencer is thus not purely dissipative or reflective, but their combination, thus being referred to as hybrid behavior. The overall effects of the grazing flow on the sound absorption coefficient are in line with the corresponding TL curve variation, i.e. the trough lifting up, peak smoothing out and higher frequency shifting. As to the reflection coefficient, the grazing flow reduces both the peaks and troughs and shifts them to higher frequencies.

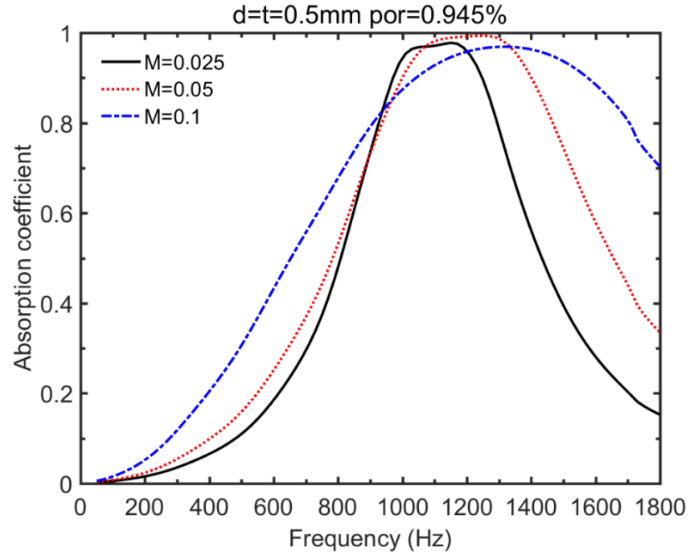
By adding partitions inside the backing cavity, the effects of the grazing flow on the silencing performance of honeycomb or locally reacting MPP silencers are presented in Fig. 5.14. Firstly, it can be observed that, different from the non-partitioned case with several dips and peaks, the TLs of the locally reacting honeycomb MPP silencers exhibit only one major peak and show one single freedom behavior. This can be explained, since with the honeycomb structure in the backing cavity, the acoustic waves inside the cavity can only move in the direction normal to the panel. In this case, the peak is induced by the quarter-wavelength Helmholtz-type resonance in the backing cavity.

Using the same configuration, the variations of the TL maximum value TL_{\max} , peak frequency f_p and 5dB TL bandwidth $W = |f_u^{TL} - f_l^{TL}|$ are used to describe the

grazing flow effects on the TL, where f_u^{TL} and f_l^{TL} are the lower and upper frequencies corresponding to 5 dB TL. Fig. 5.14a shows the variation of these defined parameters for three selected flow speeds. It can be seen that the grazing flow shifts the location of the peak frequency f_p to a higher frequency when flow speed increases, reduces the peak TL_{max} value and broadens the bandwidth W . Figure 5.14b shows that for locally reacting MPP silencers, the grazing flow affects the corresponding sound absorption coefficient in the way which is similar to TL in terms of the peak frequency shifting, peak value variation and bandwidth enlargement. It is worth noting that the presence of the grazing flow typically results in a wider acoustic attenuation bandwidth. Consequently, although the grazing flow can reduce the peak value, compared to the no-flow condition, better broadband acoustic attenuation performance could be expected provided that the MPP parameters are properly selected.



(a)



(b)

Figure 5.14. Silencing performance of honeycomb MPP silencers under different flow velocities. (a) TL, (b) sound absorption coefficient.

To quantify the extent to which the grazing flow affects the TLs of locally reacting MPP silencers, the absolute value of the difference in the TL maximum value TL_{\max} , peak frequency f_p and 5dB TL bandwidth W between $M=0.025$ and other grazing flow velocities are quantified using the following definition:

$$\begin{aligned}
 |TL_{\max}^{dif}| &= |TL_{\max}^{0.025} - TL_{\max}^M|, \\
 |f_p^{dif}| &= |f_p^{0.025} - f_p^M|, \\
 |W^{dif}| &= |W^{0.025} - W^M|,
 \end{aligned} \tag{5.46}$$

where $TL_{\max}^{0.025}$, $f_p^{0.025}$ and $W^{0.025}$ are the maximum TL value, peak frequency and

bandwidth of the TL curve for $M=0.025$; TL_{\max}^M , f_{\max}^M , W^M are their corresponding counterparts at other grazing flow velocities.

The above defined quantities with different hole diameters and perforation ratios are presented in Fig. 5.15. It is clear that, the grazing flow mainly affects the maximum value when the hole size of the panels is large and the perforation ratio is low. As to the peak frequency, more obvious effects can be observed for panels with a small hole. For the TL bandwidth, the panels with a high perforation ratio are more likely to be influenced by the grazing flow. In other words, for panels with a large hole size and low perforation ratios, the grazing flow mainly affects their maximum TL values and for panels with small holes, the grazing flow mainly affects their peak frequencies.

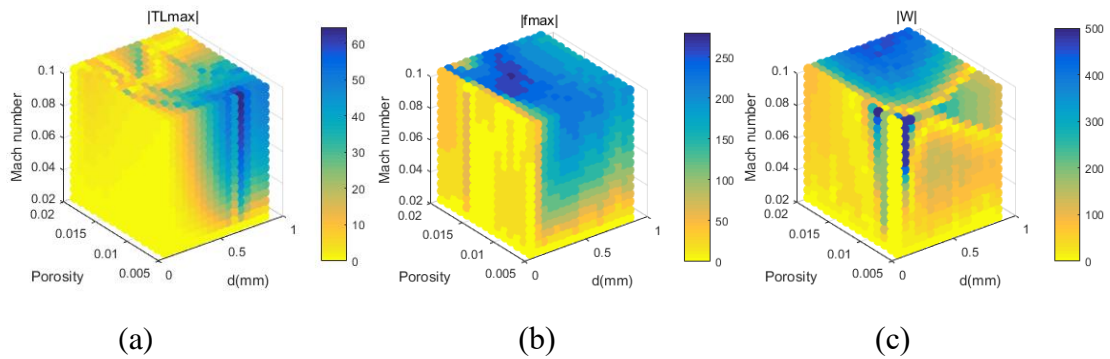


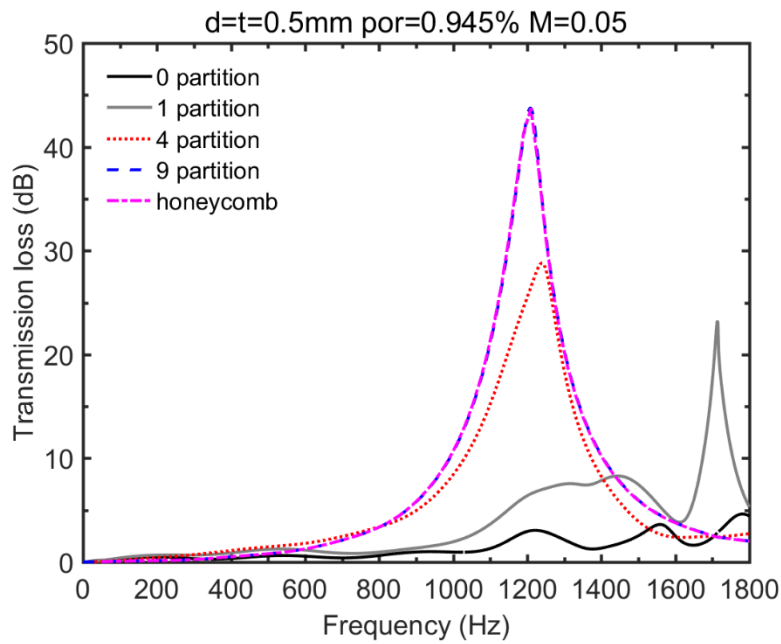
Figure 5.15. Absolute value of the difference in the TL maximum value, peak frequency and TL bandwidth between $M=0.025$ and other grazing flow velocities for different MPP silencers with $t/d=1$.

5.5.2. Effects of the partition inside the backing cavity

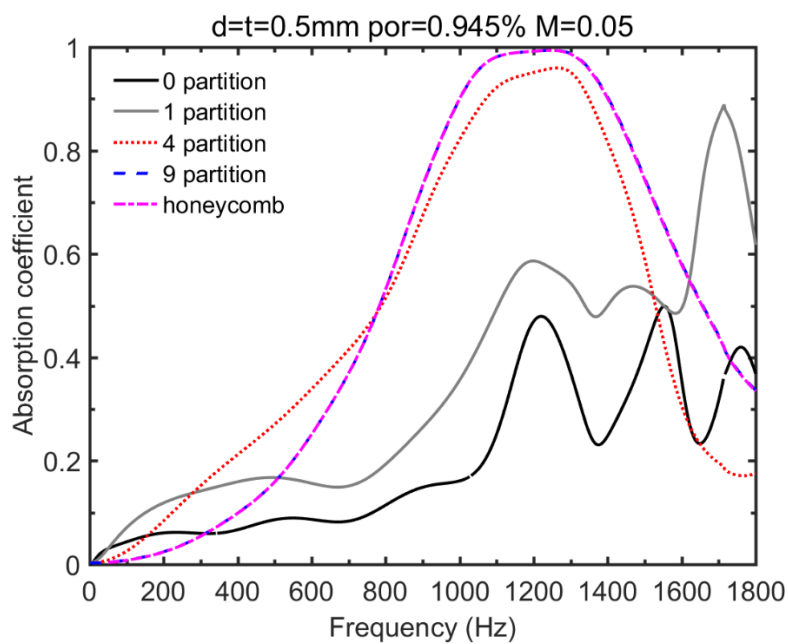
The TL, the absorption coefficient and the reflection coefficient of the MPP silencers with a backing cavity having different solid partitions are compared in Fig. 5.16. The results indicate that different partitions lead to quite different acoustic attenuation performance of the MPP silencers. Increasing the number of partitions reduces the number of ripples on both the TL curves and the absorption curves, giving rise to a narrower bandwidth but a higher peak value. Meanwhile, the reflection effect also decreases with the partitions and finally becomes negligible compared to the absorption effect. When further increasing the partitions, the acoustic behavior of the MPP silencer stops changing and approaches the locally reacting (honeycomb) MPP silencer with only one main peak. In a sense, to achieve the locally reacting effect, it is not necessary to employ a honeycomb structure which is usually designed to contain one hole in the panel by one cell in the backing cavity or a densely partitioned design. As long as the size of the divided sub-cavity is sufficient small as compared to the acoustic wavelength, wave motion in the sub-cavity is basically confined to the direction normal to the panel so that the surface impedance can be considered as locally reacting. Based on the discussion in Section 5.5.1, the length of the divided sub-cavity should be smaller than the half wavelength of the highest frequency of interest so that the axial modes of the divided sub-cavity cannot be activated and the acoustic wave would not propagate in the axial direction.

The increase of the absorption and the reduction in the reflection with increasing

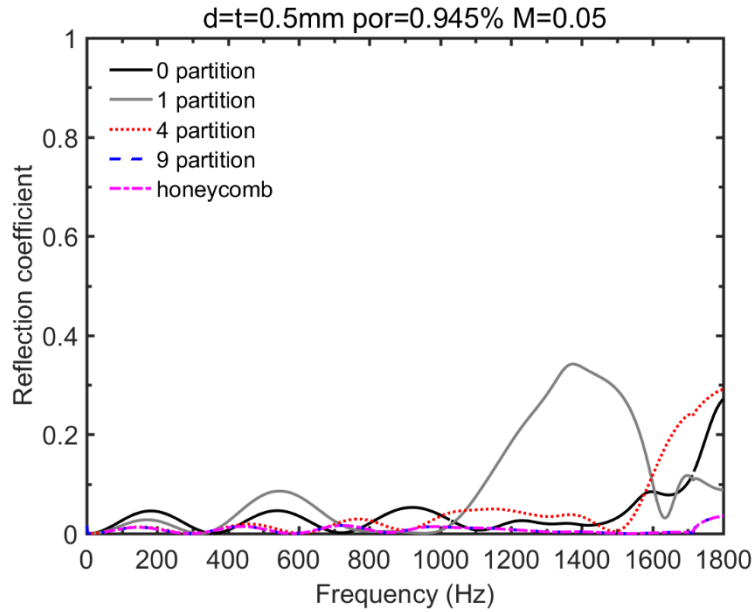
number of partitions indicate a transition in the acoustic attenuation mechanism from a hybrid mechanism (both dissipation and reflection) to almost a purely dissipative mechanism. Therefore, most of the attenuated acoustic energy are dissipated by MPP silencers with sufficient partitions or honeycomb MPP silencers.



(a)



(b)



(c)

Figure 5.16. Silencing performance of MPP silencers with different solid partitions.

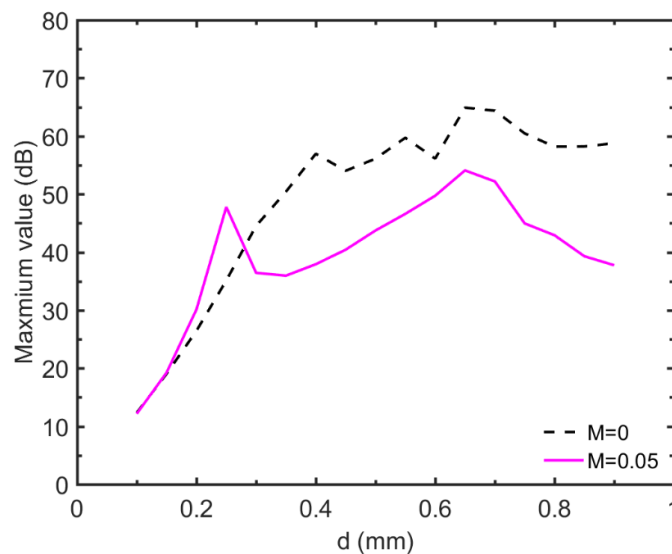
(a) TL, (b) sound absorption coefficient, (c) reflection coefficient.

5.5.3 Effects of panel parameters

5.5.3.1 Hole diameter

The maximum TL value TL_{\max} , peak frequency f_p and 5dB TL bandwidth W of the honeycomb MPP absorbers having different hole diameters, but the same perforation ratios (1%) with and without grazing flow are shown in Fig. 5.17. In the absence of the flow, it can be seen that increasing the diameter of the hole reduces the peak frequency. Meanwhile, the maximum TL value increases first and then decreases, while the TL bandwidth reduces. In the presence of grazing flow, the same trend can be

observed. Therefore, it can be expected that, to achieve a broadband acoustic attenuation for locally reacting case, the panels with small holes are preferred, irrespective of whether flow exists or not. This is understandable since for locally reacting silencer, the sound energy attenuation is predominantly due to the dissipation effects and smaller holes can usually provide wider absorption bandwidth. Therefore, to achieve broadband noise control, a locally reacting silencer with small holes is usually the best choice. This is different from the non-locally reacting case relying on hybrid sound attenuation investigated in Ref. [102], in which case, to achieve optimal broadband silencing performance, a balance between the dissipation and reflection effects needs to be struck. This explains why the comparison results for non-partitioned silencers shown in Fig. 5.18 show that the panel with smallest hole size $d = t = 0.2mm$ cannot provide the best acoustic attenuation performance.



(a)

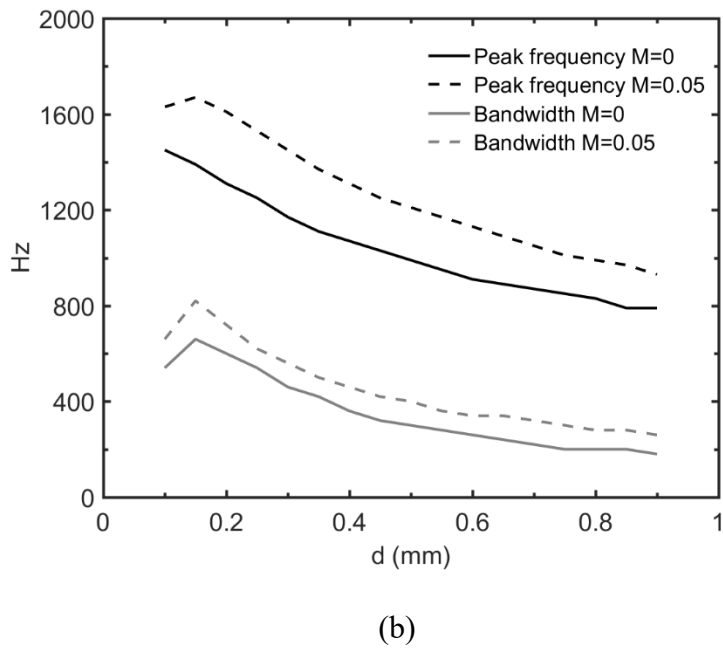


Figure 5.17. (a) TL peak value, (b) TL peak frequency and bandwidth of MPP silencers with different hole diameters.

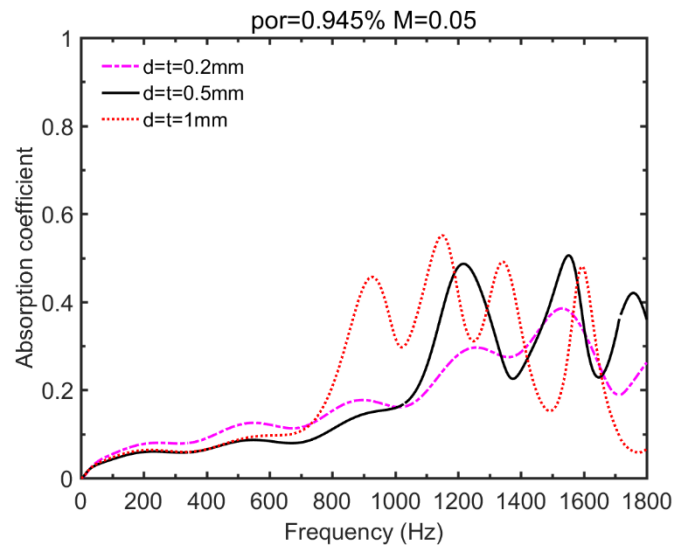
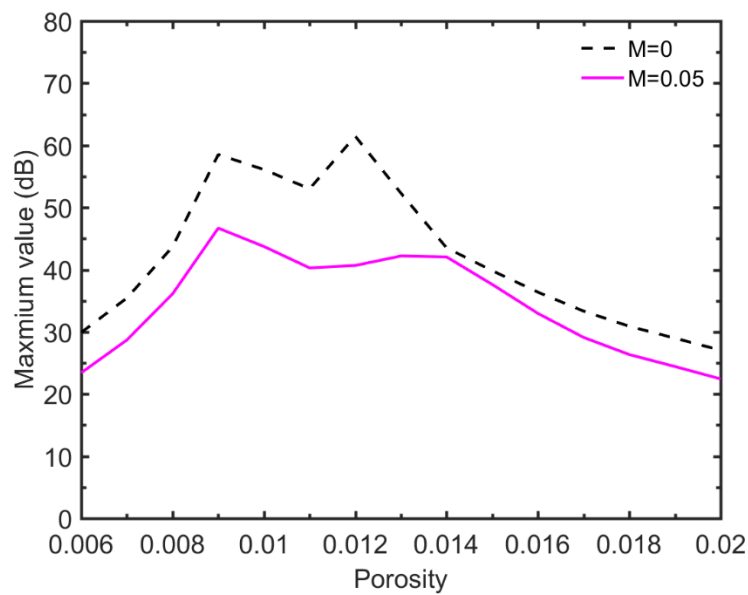


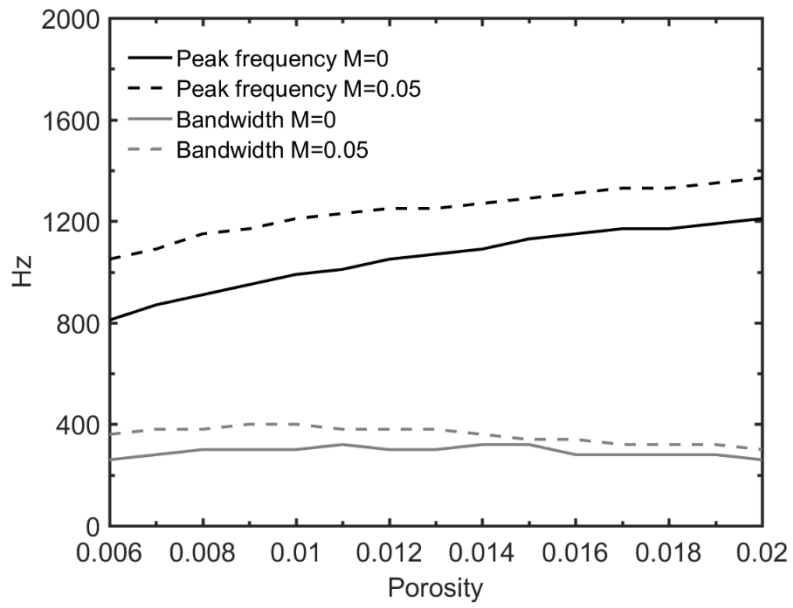
Figure 5.18. TLs of non-partitioned MPP silencers with different hole diameters.

5.5.3.2 Perforation ratio

The effects of the perforation ratio on the honeycomb MPP silencers with and without grazing flow are shown in Fig. 5.19. It can be seen that, without flow, when the perforation ratio of the panel increases, TL peak frequency is shifted to a higher frequency, whilst the peak TL value first increases and then decreases. However, the TL bandwidth keeps almost constant, seemingly unaffected by the perforation ratio. In the presence of grazing flow, the effects of panel perforation ratio on honeycomb MPP silencers are similar to the no-flow condition.



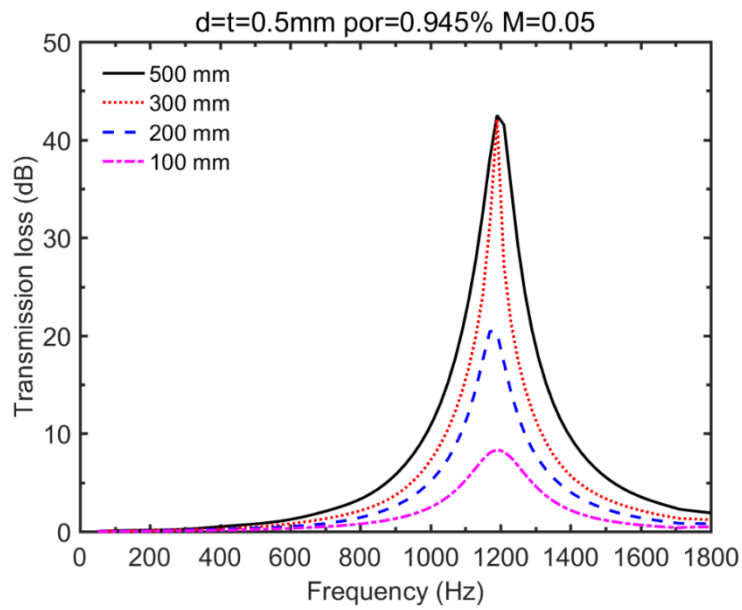
(a)



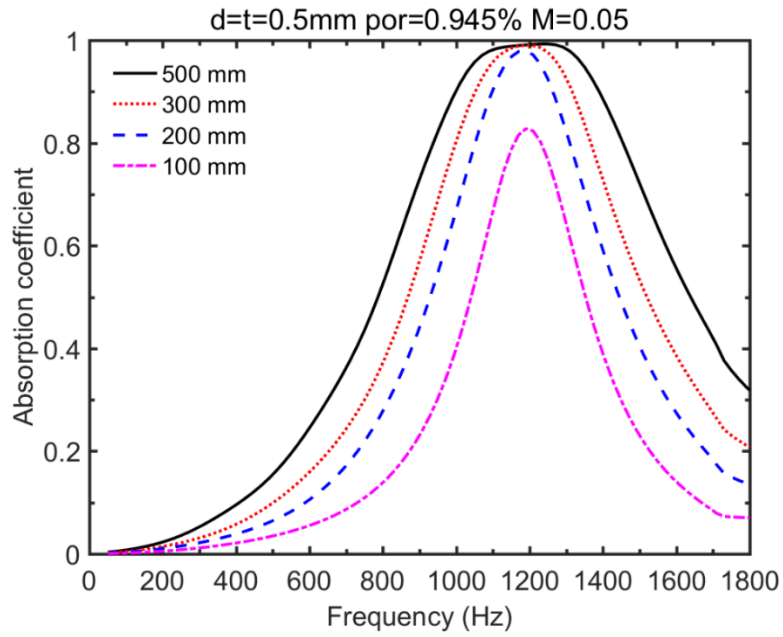
(b)

Figure 5.19. (a) TL peak value, (b) TL peak frequency and bandwidth of MPP silencers with different perforation ratio.

5.5.3.3 Panel dimension



(a)



(b)

Figure 5.20. Silencing performance of honeycomb MPP silencers with different panel lengths. (a) TL, (b) sound absorption coefficient.

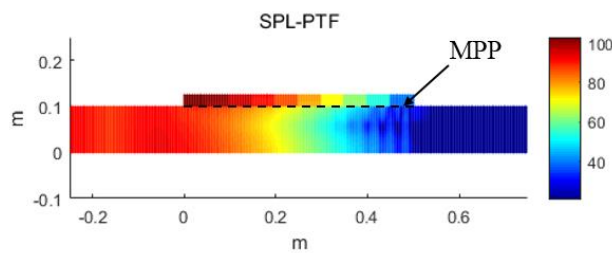


Figure 5.21. Sound pressure field of a MPP silencer with a backing cavity containing nine partitions at the peak frequency $f = 863$ Hz and $M = 0.05$.

The effect of the MPP panel dimension on the acoustic performance of MPPs is investigated. To this end, honeycomb MPP silencers with different panel lengths are

compared in terms of TL, as shown in Fig. 5.20. It is clear that the TLs of the locally reacting MPP silencers depend significantly on the size of the panel. More specifically, the maximum level and the bandwidth of both the TL and the absorption coefficient curves increase with the panel length, without, however, noticeable variations in the peak location. Meanwhile, increasing the panel length can actually enhance the acoustic performance of the silencers in a significant manner. The pressure field of an MPP silencer with a backing cavity containing nine partitions at the peak frequency $f = 863\text{Hz}$ and $M = 0.05$ is shown in Fig. 5.21. It can be seen that the energy intensity of the acoustic wave, propagating in the duct, decays continuously in the downstream direction so that more acoustic energy can be dissipated when the panel becomes longer. Therefore, a sufficiently large panel is needed when designing locally reacting MPP silencers for effective noise attenuation.

The same issue is revisited for non-partitioned MPP silencers, as shown in Fig. 5.22 at $M=0.05$. As the length of the panel can change the coupling of the entire system, in particular the frequencies at which the axial modes of the backing cavity appear, it is obvious that the number of dips and peaks on the TL curves as well as their locations are all affected by the dimension change of the panel. The variation trend, however, is much more complex than the case of locally reacting silencers. Consequently, unlike the case of locally reacting silencer, which always requires the use of the largest possible dimension, the optimal length of a non-partitioned silencer needs to be tuned to cope with a targeted frequency bandwidth.

To better understand the way to select the optimal value of the panel length for non-partitioned silencers, the pressure field of a non-partitioned MPP silencer with a panel length of 500 mm at one peak frequency $f = 1221\text{Hz}$ and $M = 0.05$ is plotted in Fig. 5.23. It can be observed that, the energy distribution of the acoustic wave, propagating in the duct, does not necessarily decay continuously in the axial direction in the lined part, which is different from the locally reacting case. The complex sound pressure distribution across the MPP panel also testifies the increasing complexity of the acoustic coupling in the non-partitioned silencer. In such cases, a system optimization, with the help of the PTF model developed in this Chapter, becomes possible and necessary.

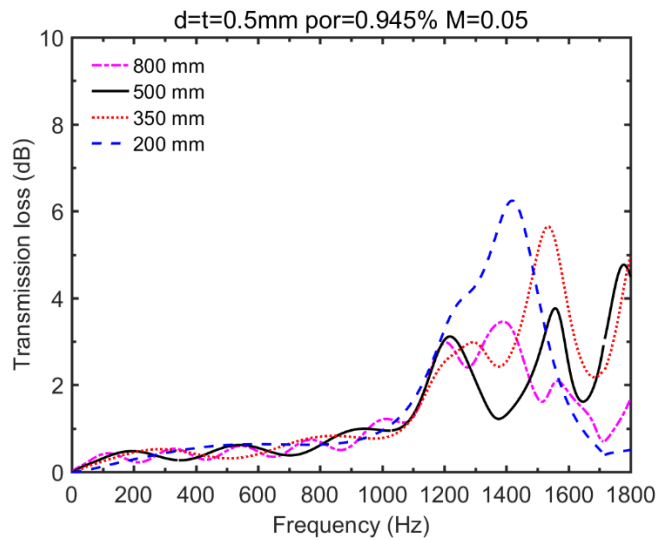


Figure 5.22. TLs of non-partitioned MPP silencers with different panel lengths at $M=0.05$.

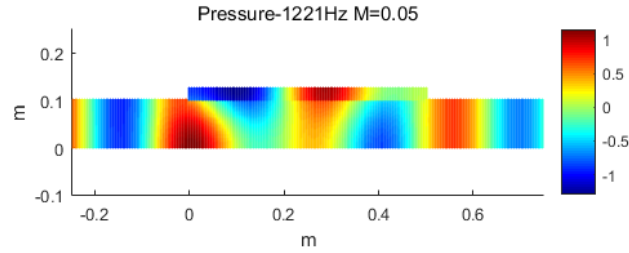


Figure 5.23. Sound pressure distribution inside a non-partitioned MPP silencer with panel length of 500mm at one peak frequency $f = 1221Hz$ and $M = 0.05$.

5.6. Summary

The acoustic behavior of micro-perforated panels in flow ducts is investigated numerically using a PTF model after experimental validations. The effects of solid partitions inside the backing cavity, as well as those of the grazing flow, the hole diameter, the perforation ratio and the panel dimension are systematically investigated to provide guidance for MPP silencer design.

The following conclusions can be drawn from the numerical analyses. Partitions inside the backing cavity can lead to quite different acoustic attenuation performance of the MPP silencers. The design of the backing cavity should be determined based on specific needs. Grazing flow typically shifts the TL peak to a higher frequency, alters its maximum level and flattens the TL curve with a wider bandwidth. The effects of the hole diameter and the perforation ratio on the silencing performance of MPPs under grazing flow are similar to cases without flow. The panel dimension actually

significantly affects the acoustic performance of the MPPs. While exhibiting a more intuitive influencing manner in the case of locally reacting case, the size of the MPP in a non-partitioned silencer, however, needs more meticulous consideration, which calls for a systematic system optimization to target a prescribed frequency range. In that sense, the model proposed in this Chapter could serve as a useful and indispensable tool.

Chapter 6. MPPs in Noise Control Devices with Complex Geometry

Different from the MPPs in a straight duct with a regular geometry studied in Chapter 5, the feasibility of integrating MPPs in a home appliance having a more complex geometry and being subjected to flow is explored in this Chapter. The PTF approach is again employed to tackle the aforementioned numerical challenges (Chapter 5) in terms of coping with the need to efficiently model systems with complex geometry. Two methods, the FEM method and coordinate transformation technique, are presented here to calculate the PTFs of the irregular subsystems. For the former, referred to as hybrid theoretical-numerical technique, analytical approach is adopted for PTFs calculations of subsystems with regular geometry and FEM for subsystems with complex geometry. For the latter, a coordinate transformation technique is proposed to treat the irregular subsystem, before being incorporated into the previously developed PTF framework. Meanwhile, the feasibility of implementing MPP absorbers in a practical industrial device to reduce acoustic noise is demonstrated. By the same token, the capability and the effectiveness of the PTF approach along with the impedance prediction formulae established in Chapter 3 are further demonstrated under a more practical context.

In what follows, the PTF-based hybrid theoretical-numerical implementation procedure is first presented in Section 6.1. The accuracy of the hybrid modeling

approach is then compared with experimental measurement. Through numerical analyses, presented in Section 6.3, the potential of using MPPs to improve the silencing performance of a home appliance is demonstrated. Influences of the grazing flow on the acoustic performance of the system and those of the MPP parameters are investigated, highlighting the necessity of performing parameter tunings to achieve desired silencing performance. Subsequently, optimizations are conducted. In Section 6.4, the formulation and the implementation procedure of the coordinate transformation technique are presented and validated. The improvement brought by this technique compared with the hybrid theoretical-numerical treatment is demonstrated through an optimization study. Meanwhile, the capability and the computational efficiency of the PTF approach are evidenced through these analyses.

6.1. Formulation of the problem

The PTF approach is employed to predict the *in-situ* acoustic performance of MPPs in the complex acoustic environment with grazing flow. A representative configuration, shown in Fig. 6.1 (left), is considered here. The model is inspired by a mock-up of the housing of a range hood for households, which can be simplified as two inter-connected cavities as shown in Fig 6.1. For noise reduction purposes, MPPs are placed on its inner wall surfaces. As an illustrative example, the case of a single MPP exposed to grazing flow is considered here. Similar as before, the assumption of low flow speed is used. Therefore, the effects of the grazing flow are introduced only via the acoustic

impedance of MPPs by using the impedance prediction formulae established in Chapter 3, and the medium is considered to be still provided that the convective effects on the wave propagation can be neglected. The module with MPP is put into a duct and the whole system is partitioned into six subsystems as illustrated in Fig. 6.2: an inlet duct, a main cavity above the MPP liner, a sub-cavity of a trapezoidal shape, an outlet duct, an MPP and its backing cavity. Four coupling interfaces are then formed, denoted by C1, C2, C3 and C4, respectively. These four interfaces are segmented into patches with a half-wavelength criterion [51], numbered as N_1 , N_2 , N_3 and N_4 , respectively. Before considering the coupling, the PTFs of each uncoupled subsystem are firstly calculated separately.

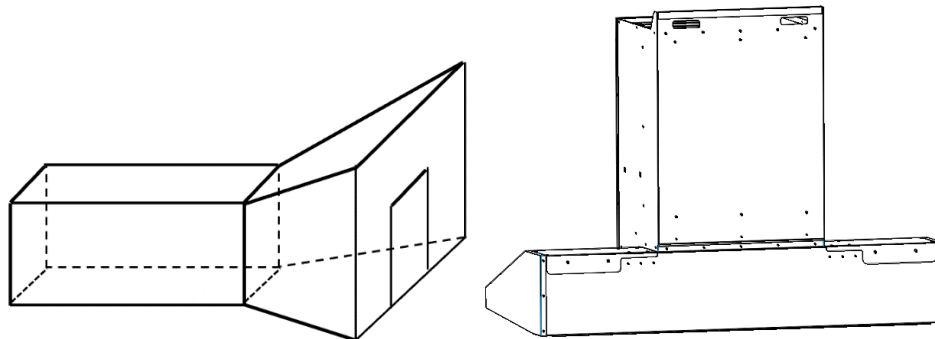


Figure 6.1. Housing of a range hood (right) and its mock-up (left).

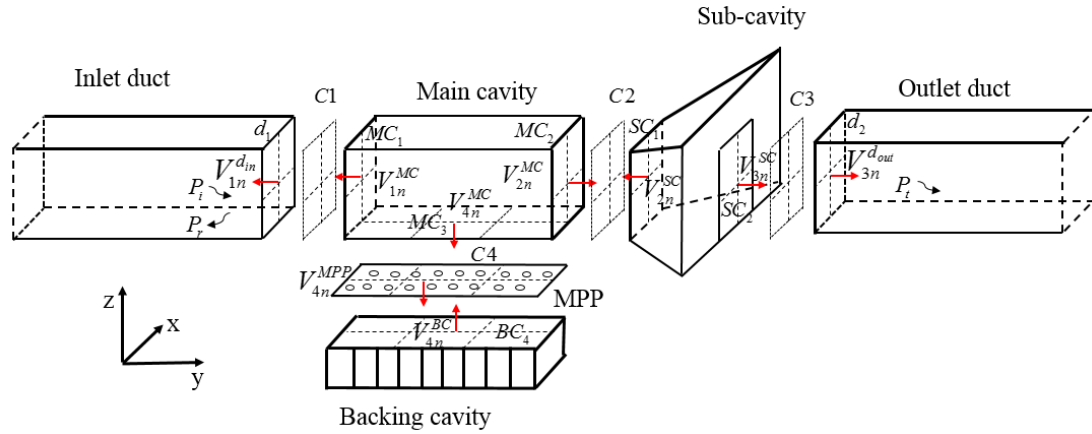


Figure 6.2. Sub-structure treatment of the whole system.

Both the main cavity and the backing cavity can be modeled as a 3D rectangular cavity. Therefore, their corresponding PTFs can be calculated by using Eq. 5.18. The PTFs of the inlet and outlet duct, both being treated as semi-infinite ducts, can be obtained by using Eq. 5.25. In the present case, the vibration of the MPP is not considered, thus Eq. 5.30 is used for the associated PTF calculations. For the trapezoidal sub-cavity, FEM is firstly employed for its PTF calculation. Consequently, with this sub-structure treatment, instead of purely relying on FEM, a hybrid theoretical-numerical model will be developed to deal with system with complex geometry.

After calculating the PTFs of all separated subsystems, by applying the continuity condition on the connecting patches of the four coupling surfaces, subsystems are finally coupled together. The force balance of the patches at four coupling interfaces leads to the following expressions:

$$\bar{P}_{r_1}^{-d_{in}} + \sum_{e_1}^{N_1} Z_{r_1 e_1}^{d_{in} d_{in}} \bar{u}_{e_1}^{-d_{in}} = \sum_{e_1}^{N_1} Z_{r_1 e_2}^{MC_1 MC_1} \bar{u}_{e_1}^{-MC_1} + \sum_{e_2}^{N_2} Z_{r_1 e_3}^{MC_1 MC_2} \bar{u}_{e_3}^{-MC_2} + \sum_{e_4}^{N_4} Z_{r_1 e_4}^{MC_1 MC_3} \bar{u}_{e_4}^{-MC_3},$$

$\forall r_1 \in [1, \dots, N_1]$ at interface 1,

$$\sum_{e_2}^{N_2} Z_{r_2 e_2}^{SC_1 SC_1} \bar{u}_{e_2}^{-SC_1} + \sum_{e_3}^{N_3} Z_{r_2 e_3}^{SC_1 SC_2} \bar{u}_{e_3}^{-SC_2} = \sum_{e_1}^{N_1} Z_{r_2 e_1}^{MC_2 MC_1} \bar{u}_{e_1}^{-MC_1} + \sum_{e_2}^{N_2} Z_{r_2 e_3}^{MC_2 MC_2} \bar{u}_{e_2}^{-MC_2} + \sum_{e_4}^{N_4} Z_{r_2 e_4}^{MC_1 MC_3} \bar{u}_{e_4}^{-MC_3},$$

$\forall r_2 \in [1, \dots, N_2]$ at interface 2,

$$\sum_{e_2}^{N_2} Z_{r_3 e_2}^{SC_2 SC_1} \bar{u}_{e_2}^{-SC_1} + \sum_{e_3}^{N_3} Z_{r_3 e_3}^{SC_2 SC_2} \bar{u}_{e_3}^{-SC_2} = \sum_{e_3}^{N_3} Z_{r_3 e_3}^{d_{out} d_{out}} \bar{u}_{e_3}^{-d_{out}},$$

$\forall r_3 \in [1, \dots, N_3]$ at interface 3,

$$\sum_{e_4}^{N_4} Y_{MPP} \left(\sum_{j_1}^{N_1} Z_{e_4 j_1}^{MC_3 MC_1} \bar{u}_{j_1}^{-MC_1} + \sum_{j_2}^{N_2} Z_{e_4 j_2}^{MC_3 MC_2} \bar{u}_{j_2}^{-MC_2} + \sum_{j_4}^{N_4} Z_{e_4 j_4}^{MC_3 MC_3} \bar{u}_{j_4}^{-MC_3} - \sum_{j_4}^{N_4} Z_{e_4 j_4}^{BC_4 BC_4} \bar{u}_{j_4}^{-BC_4} \right) = \bar{u}_{r_4}^{-MPP}$$

$\forall r_4 = e_4 \in [1, \dots, N_4]$ at interface 4. (6.1)

The equality of the normal velocity across the patches at the four coupling faces

writes:

$$\begin{aligned} \bar{u}_{e_1}^{-MC_1} &= \bar{u}_{e_1}^{-d_1}, & \forall e_1 \in [1, \dots, N_1] \text{ at interface 1,} \\ \bar{u}_{e_2}^{-MC_2} &= \bar{u}_{e_2}^{-SC_1}, & \forall e_2 \in [1, \dots, N_2] \text{ at interface 2,} \\ \bar{u}_{e_3}^{-SC_2} &= \bar{u}_{e_3}^{-d_2}, & \forall e_3 \in [1, \dots, N_3] \text{ at interface 3,} \\ \bar{u}_{e_4}^{-MC_3} &= -\bar{u}_{e_4}^{-BC_4} = \bar{u}_{r_4}^{-MPP}, & \forall r_4 = e_4 \in [1, \dots, N_4] \text{ at interface 4.} \end{aligned} \quad (6.2)$$

Equations 6.1 and 6.2 can be written in the following condensed matrix form:

$$P^{-d_1} + Z^{d_1} V_{1n}^{d_1} = Z_{11}^{MC} V_{1n}^{MC} + Z_{12}^{MC} V_{2n}^{MC} + Z_{13}^{MC} V_{4n}^{MC},$$

$$\begin{aligned}
Z_{11}^{SC}V_{2n}^{SC} + Z_{12}^{SC}V_{3n}^{SC} &= Z_{21}^{MC}V_{1n}^{MC} + Z_{22}^{MC}V_{2n}^{MC} + Z_{23}^{MC}V_{4n}^{MC}, \\
Z_{21}^{SC}V_{2n}^{SC} + Z_{22}^{SC}V_{3n}^{SC} &= Z^{d_2}V_{3n}^{d_2}, \\
Y(Z_{31}^{MC}V_{1n}^{MC} + Z_{32}^{MC}V_{2n}^{MC} + Z_{33}^{MC}V_{4n}^{MC} - Z_{44}^{BC}V_{4n}^{BC}) &= V_{4n}^{MPP}, \\
V_{1n}^{MC} &= V_{1n}^{d_1}, \\
V_{2n}^{MC} &= V_{2n}^{SC}, \\
V_{3n}^{d_2} &= V_{3n}^{MC}, \\
V_{4n}^{MC} &= V_{4n}^{MPP} = -V_{4n}^{BC}.
\end{aligned} \tag{6.3}$$

Eq. 6.3 can be further condensed into the following form as,

$$\{\mathbf{Z}\}\{\mathbf{V}\} = \{\mathbf{F}\}, \tag{6.4}$$

$$\text{where } Z = \begin{bmatrix} Z_{11}^{MC} - Z^{d_1} & Z_{12}^{MC} & 0 & Z_{13}^{MC} \\ Z_{21}^{MC} & Z_{22}^{MC} - Z_{11}^{SC} & -Z_{12}^{SC} & Z_{23}^{MC} \\ 0 & Z_{21}^{SC} & Z_{22}^{SC} - Z^{d_2} & 0 \\ YZ_{31}^{MC} & YZ_{32}^{MC} & 0 & Y(Z_{33}^{MC} + Z_{44}^{BC}) - I \end{bmatrix},$$

$$V = \begin{bmatrix} V_{1n}^{MC} \\ V_{2n}^{MC} \\ V_{3n}^{d_2} \\ V_{4n}^{MC} \end{bmatrix} \text{ and } F = \begin{bmatrix} P^{d_1} \\ 0 \\ 0 \\ 0 \end{bmatrix}.$$

If the backing cavity is to be partitioned into smaller cavities, as shown in Fig. 6.2, the case can be seen as a combination of multiple unit cells, each comprising an MPP facing and an acoustic backing cavity. Assuming the unit cells are well separated from each other by solid partition walls, the mobility matrix Y of the coupling surface C4 and the backing cavity impedance matrix Z_{44}^{BC} can be constructed by combing all the unit

$$\Pi_{out} = \frac{1}{2} \int_{S_3} \text{Re}\{P_3 \times V_3^*\} dS_3, \quad (6.7)$$

where V_3 and P_3 are the normal velocity and the sound pressure at interface 3, respectively, S_3 is the total surface area of interface 3.

The reflection coefficient R_{ef} and sound absorption coefficient α can be obtained by using Eqs. 5.39 and 5.41, respectively.

6.2. Experimental validations

Experiments are conducted to validate the model. Same as before, the TL is measured by the four-microphone-two-source method [109]. The sound absorption coefficient α is experimentally obtained through the method described in Section 5.4 by using Eq. 5.42.

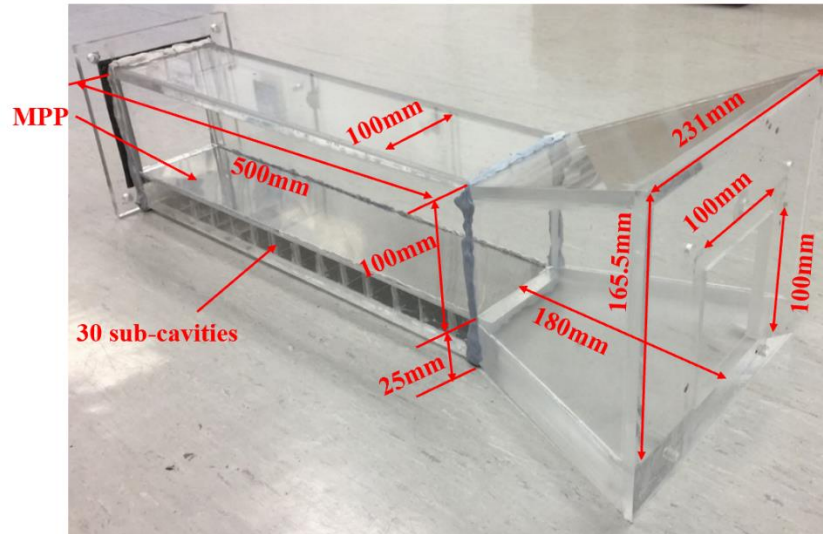


Figure 6.3. Test sample.

A sample, as shown in Fig. 6.3, is constructed and tested. An aluminum MPP is placed on one surface of the main cavity with a width and a length of 100 and 500 mm, respectively. The perforation ratio of the MPP is 0.945%. The diameter of the MPP hole and thickness of the panel are both 0.5mm. The depth of the backing cavity behind the MPP is 25 mm, which is partitioned into 30 cells. The MPP absorber in this case can be regarded as locally reacting. The detailed dimension of the model is also illustrated in Fig. 6.3.

The experimental setup is sketched in Fig. 6.4. Measurements are conducted in the same closed-loop low-speed acoustic wind tunnel described in Chapter 3. Four 1/4-inch., microphones are used here with two of them flush-mounted upstream the testing sample and the two others flushed mounted in the downstream segment. The separation distance between a pair of the microphones is 80mm. Figure 6.5 shows a photo of the

test set-up.

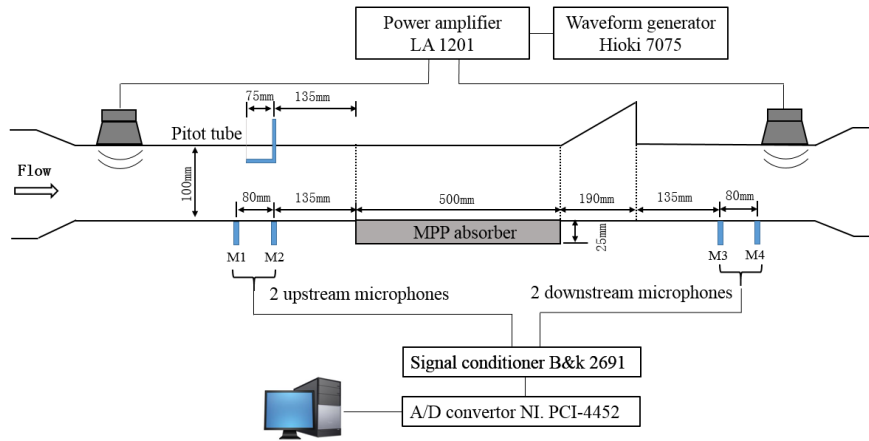


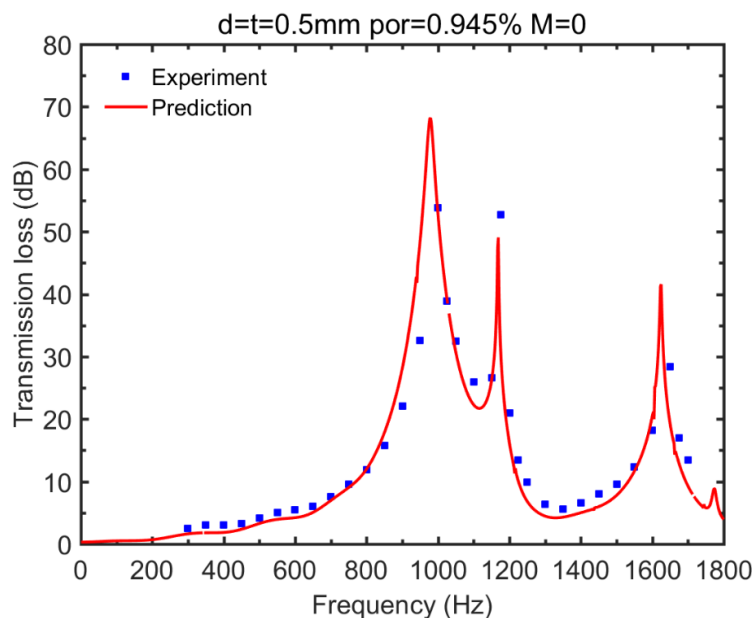
Figure 6.4. Sketch of the test set-up.



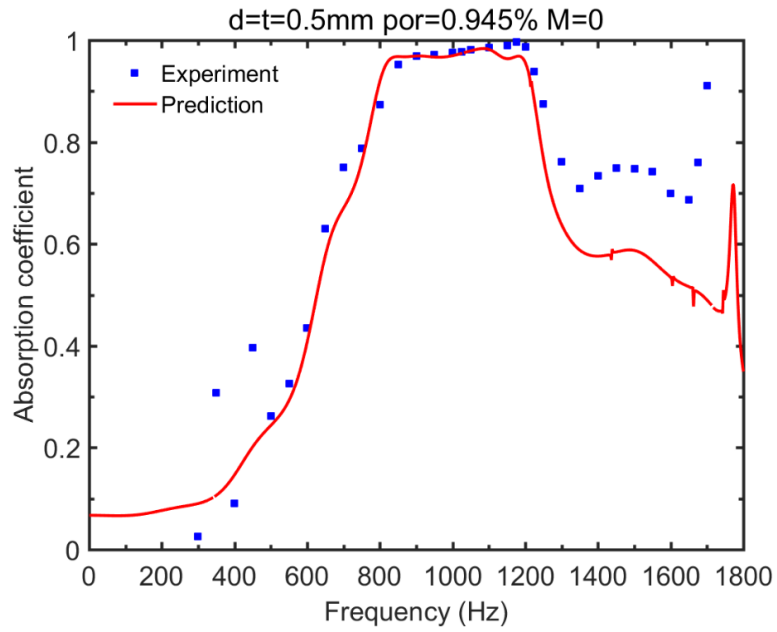
Figure 6.5. Photo of the experimental setup.

The accuracy of the PTF model is validated through comparisons with measured data. The TL, sound absorption coefficient and reflection coefficient curves correspond to various grazing flow velocities are compared in Figs. 6.6-6.8. The comparisons show

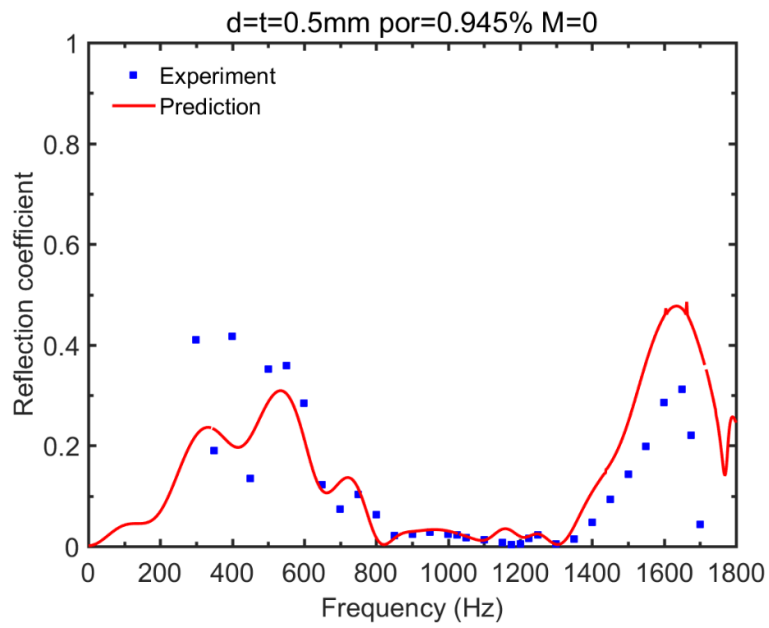
that the prediction curves can fit the experimental data reasonably well and a good agreement between the prediction and the measured data is observed for various flow speeds. However, same as before, with flow, an obvious deviation of the predicted maximum TL values from the measured ones can be observed. In fact, the measured maximum TL values are always lower than the predicted ones. This can be explained by the same reason put forward in Section 5.4 in that the presence of grazing flow increases the background noise, and by maintaining the low limited acoustic excitation to avoid nonlinear effects, the signal to noise ratio that can be achieved in the experiment is not good enough. Apparently, the high TL values cannot be measured when flow is present. Nevertheless, the above comparisons can still confirm the validity of the numerical approach.



(a)



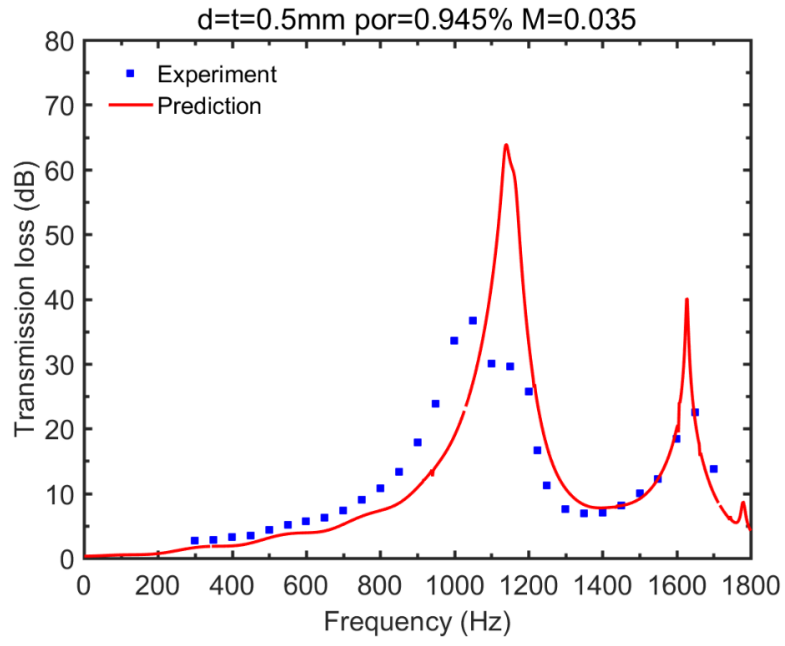
(b)



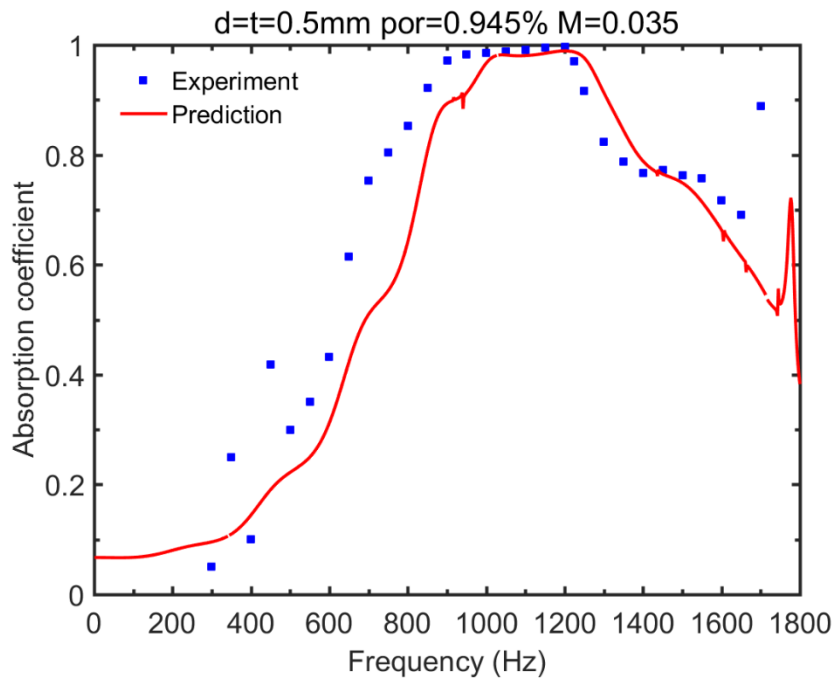
(c)

Figure 6.6. Comparisons between the predictions and experimental data at $M=0$, (a)

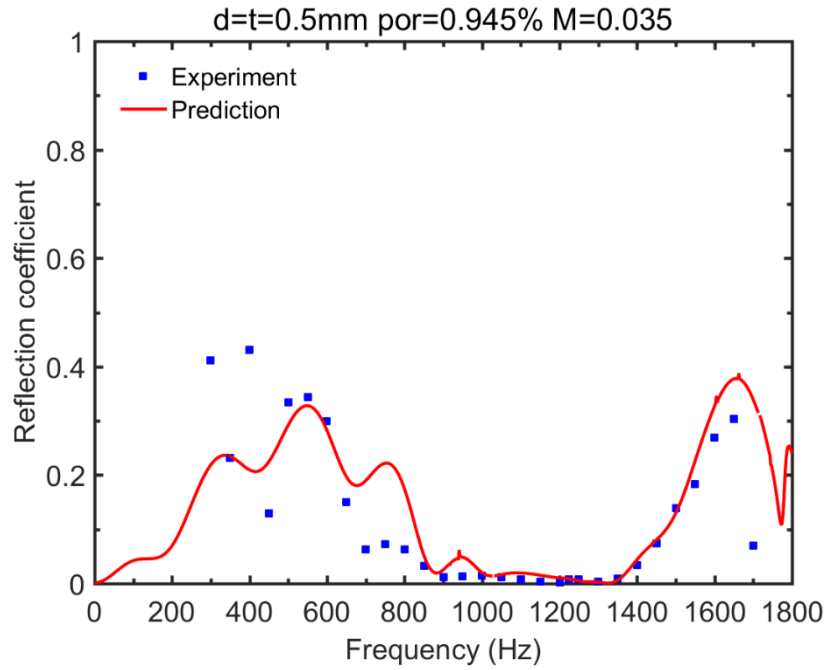
TL, (b) sound absorption coefficient, (c) reflection coefficient.



(a)

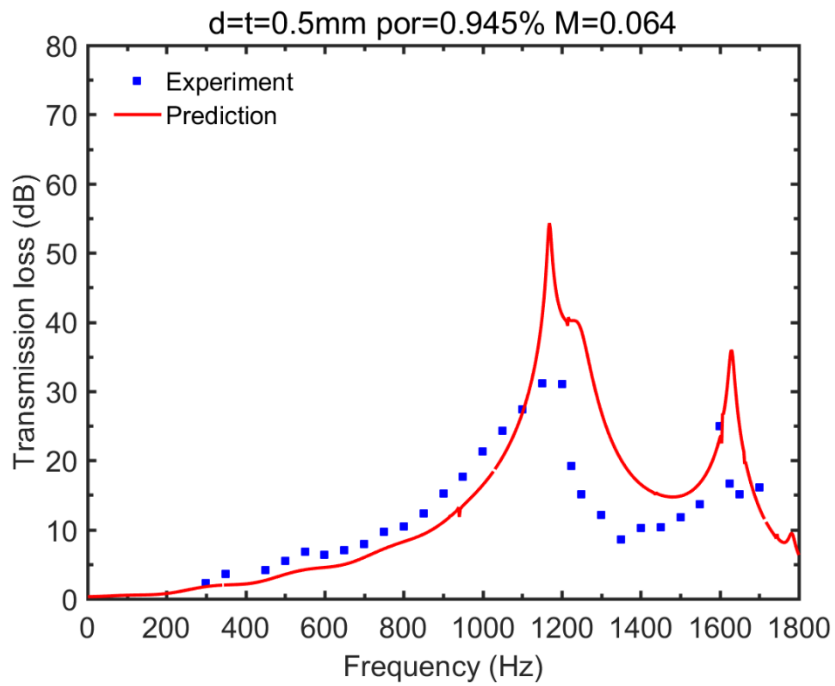


(b)

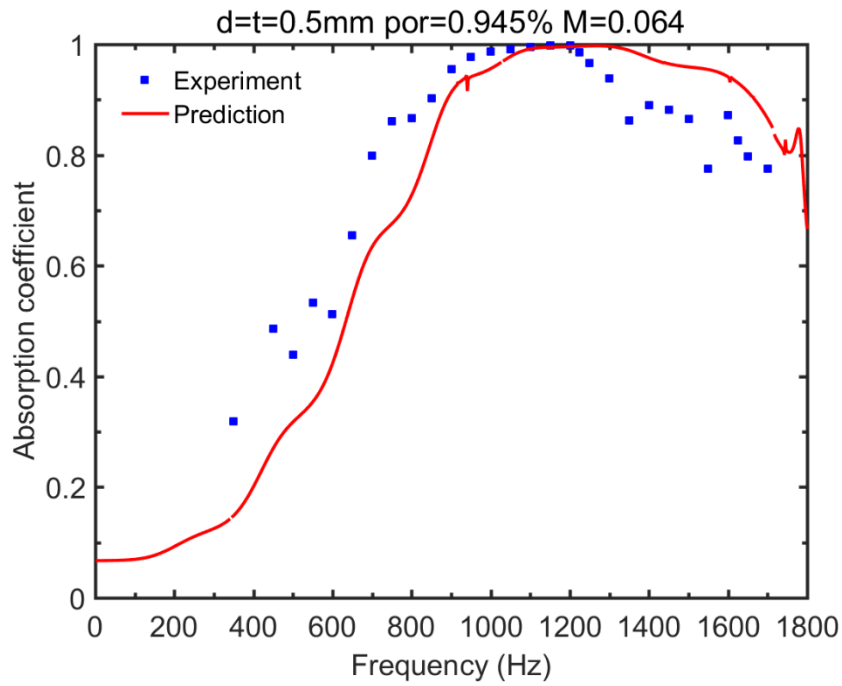


(c)

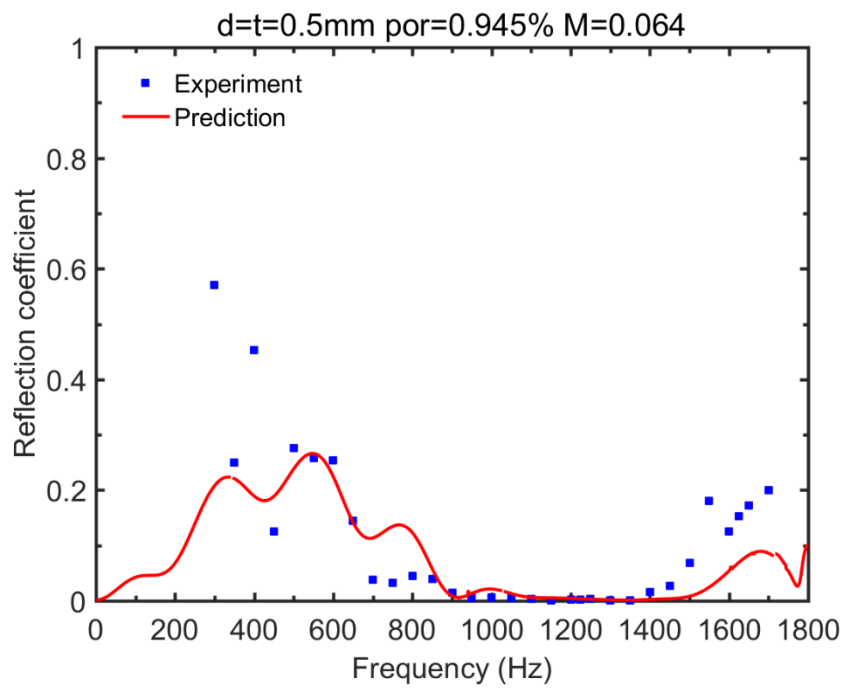
Figure 6.7. Comparisons between the predictions and experimental data at $M = 0.035$, (a) TL, (b) sound absorption coefficient, (c) reflection coefficient.



(a)



(b)



(c)

Figure 6.8. Comparisons between the predictions and experimental data at $M = 0.064$, (a) TL, (b) sound absorption coefficient, (c) reflection coefficient.

6.3. Numerical results and analyses

6.3.1. Duct without MPP

The Transmission Loss of the model without MPP in the absence of flow is first investigated, with the corresponding TL curve presented in Fig. 6.9. It can be seen that two peaks appeared on the TL curve, with their locations corresponding to $f = 1169\text{Hz}$ and $f = 1625\text{Hz}$, respectively, where a high acoustic attenuation can only be achieved at these two frequencies with very narrow bandwidth. The locations of these two TL peaks roughly correspond to the two natural frequencies of the hard-walled trapezoidal cavity $f_r^{irr} = 1216\text{Hz}$ and $f_r^{irr} = 1608\text{Hz}$. It is obvious that these two TL peaks are induced by the excitation of two corresponding trapezoidal cavity modes. To better understand the physical mechanism behind these phenomena, the absorption and reflection coefficient curves are plotted in Fig. 6.10 by using Eqs. 5.39 and 5.41 to separate the absorbed and reflected energy components. It can be seen that the acoustic energy is attenuated only by the reflection through typical reactive behavior, as expected, with virtually zero absorption across the entire frequency range, and consequently, only the reflection contributes to the appearance of these two peaks. The reactive effects are obviously due to the impedance mismatch induced by the cross-sectional changes in the trapezoidal part of the model. Meanwhile, this also points at the necessity of adding absorptions to the system to enhance the acoustic mitigation performance.

For further illustration, the sound pressure level distribution inside the model at the

two peaks ($f = 1169\text{Hz}$ and $f = 1625\text{Hz}$) on the TL curve are presented in Fig. 6.11.

It can be clearly seen that due to the reflection effects, standing waves are generated inside the duct with the maxima and minima of the acoustic amplitude appearing alternatively along the axial direction, as a result of the interference between the arriving and the reflected waves.

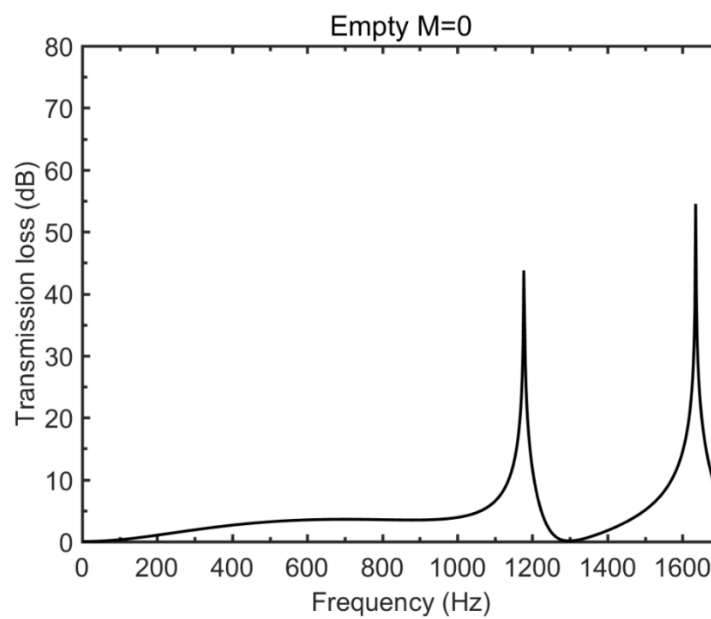


Figure 6.9. TL of the model without MPP.

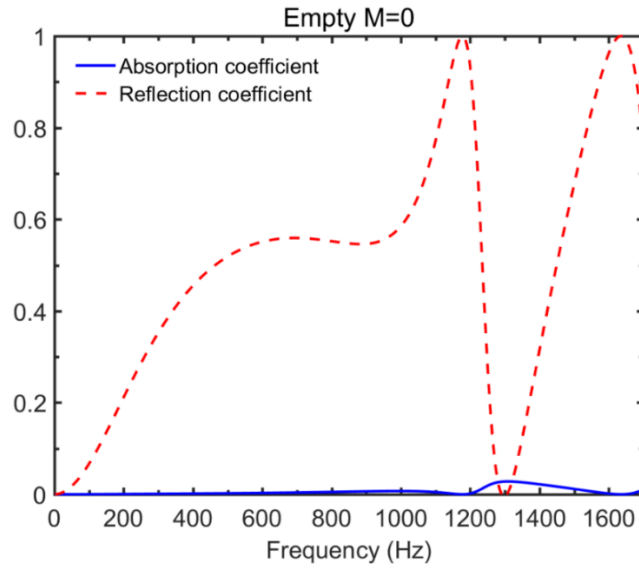
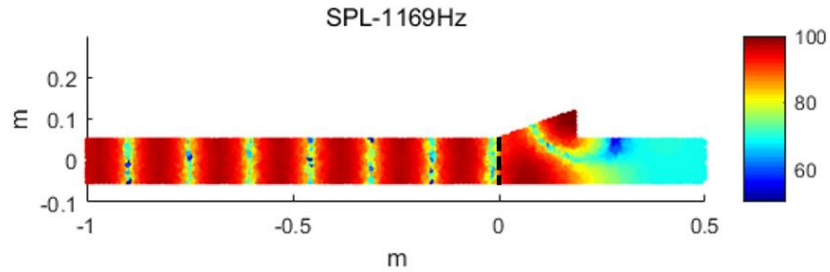
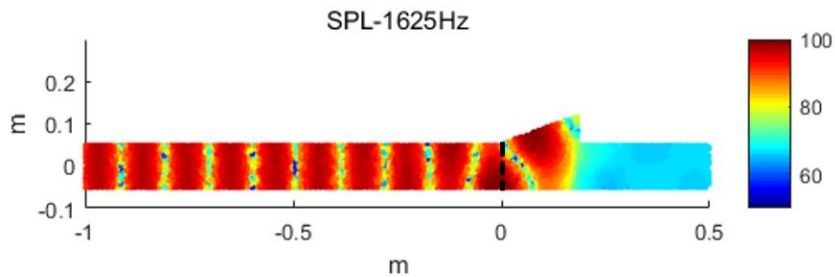


Figure 6.10. Sound absorption and reflection coefficient curves of the model without MPP.



(a)



(b)

Figure 6.11. Sound pressure field of the model without MPP in the absence of grazing flow, (a) $f = 1169\text{Hz}$, (b) $f = 1625\text{Hz}$.

6.3.2. Effects of the MPP absorber

The predicted TL curves of the model with and without MPP are compared and presented in Fig. 6.12. The parameters of the MPP ($d = t = 0.5\text{mm}$, $\delta = 0.945\%$), the partitions and the dimension of the backing cavity are the same as the test sample shown in Fig. 6.3. It can be seen that the MPP absorber generates an additional dominant peak on the TL curve ($f = 979\text{Hz}$), increases the TL value and broadens the attenuation bandwidth. Clearly, the acoustic performance of the system is improved after adding the MPP absorber.

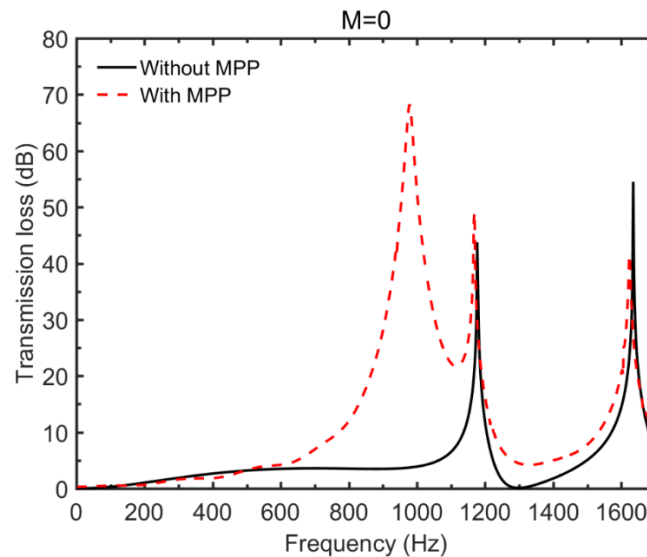


Figure 6.12. TL curves of the range hood model with and without MPP.

To further illustrate the above changes brought about by the MPP absorber, the absorption and reflection curves of the system are plotted in Fig. 6.13. It can be seen that the location of the absorption peak coincides with that of the newly appeared TL peak ($f = 979\text{Hz}$). Clearly, the new peak is due to the absorption effects of the

MPP absorber. The partition inside the backing cavity makes the MPP locally reacting, as previously analyzed in Chapters 4 and 5. Consequently, the absorption peak on the absorption curve is induced by the quarter-wavelength Helmholtz-type resonance in the backing cavity. Results in Fig. 6.13 also indicates that the absorption effects provided by the MPP absorber becomes dominant whilst the reflection effect reduces. To explain this phenomenon the sound pressure distribution inside the duct at $f = 979\text{Hz}$ is presented in Fig. 6.14. It can be seen that the incoming acoustic wave first interacts with MPP, and then enters into the trapezoidal part of the model and encounters an cross-sectional change, thus entailing wave reflections. The acoustic energy in the lined part decays continuously in the axial direction, thus, within the frequency range where MPP works effectively, most of the energy is absorbed and consequently the energy reflection reduces. However, Fig. 6.13 also shows that when MPP loses its absorption effect, the reflection provided by the system itself can compensate for the deficiency in energy dissipation of the MPP to ensure a broadband acoustic attenuation. Altogether such a hybrid mechanism finally ensures a relatively high and broadband TL. Therefore, a good design should be the one which allows a good balance between the absorption and reflection effects. Of course, it can be expected that, even when the absorption effect dominates, MPP absorbers with optimized parameters warrant even better silencing performance.

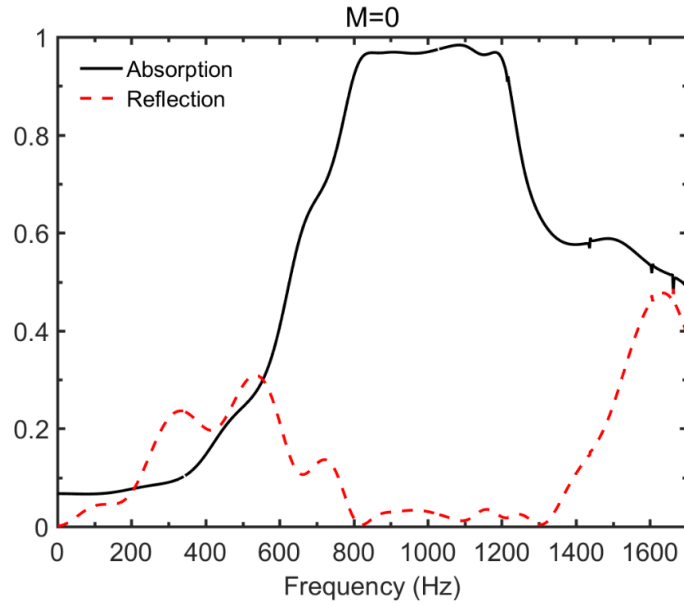


Figure 6.13. Sound absorption and reflection coefficient curves of the range hood model with MPP.

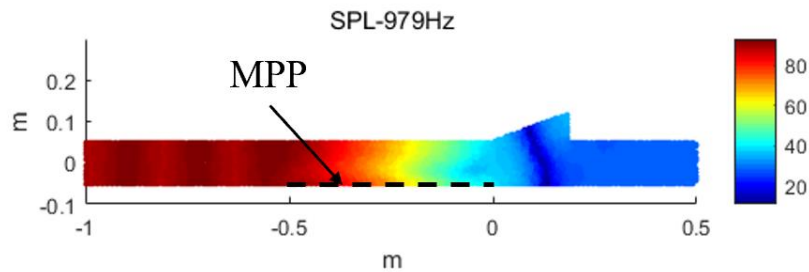


Figure 6.14. Sound pressure field in the model with MPP at $f = 979\text{Hz}$ in the absence of grazing flow.

6.3.3. Parametric studies

Striving for an optimal TL, influences of various system parameters with and without flow are examined numerically hereafter. In the following simulations, the

basic geometric configuration of the model remains unchanged, the flow velocity and the parameters related to the panel are varied.

The effects of the grazing flow are examined firstly. The TL curves of the system with MPP under different grazing flow velocities are compared in Fig. 6.15. Results show that the presence of grazing flow obviously affects the silencing performance of the system. More specifically, the grazing flow shifts the location of the TL peak at $f = 979\text{Hz}$, which is induced by the quarter-wavelength Helmholtz-type resonance effect, to a higher frequency and reduces its peak value. Accordingly, the TL value, the attenuation bandwidth and the effective frequency range are all altered by the presence of the flow. Generally speaking, the grazing flow results in a lower but wider TL curve, which is consistent with the conclusions drawn from MPPs in straight flow ducts in Section 5.5.1.

The corresponding sound absorption coefficient curves are plotted in Fig. 6.16 as well to explain the above observed changes. It can be seen that the grazing flow apparently influences the *in-situ* acoustic behavior of the MPP absorber, in terms of the shifting of the absorption curve to higher frequencies, changes in the maximum absorption value as well as the widening of the absorption bandwidth. These changes are consistent with those observed on the TL curve, which confirms that the changes of the TL curve are mainly attributed to the variations of the acoustic behavior of the MPPs. The above observation again demonstrates that the acoustic of MPP is sensitive to the

grazing flow.

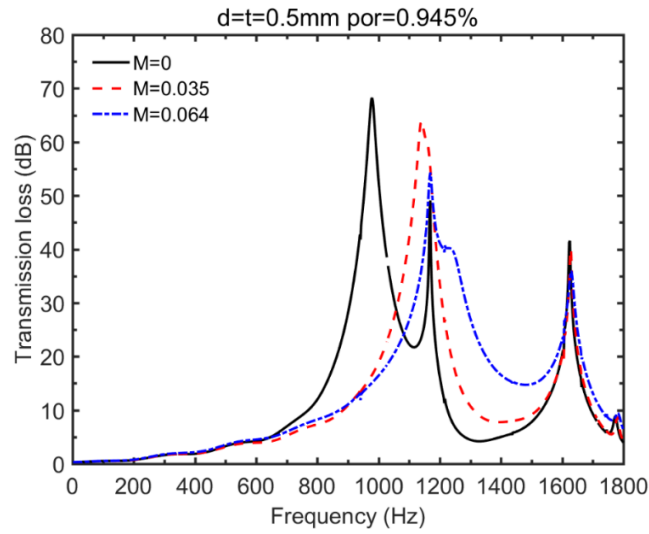


Figure 6.15. TL curves of the range hood model with MPP under different flow velocities.

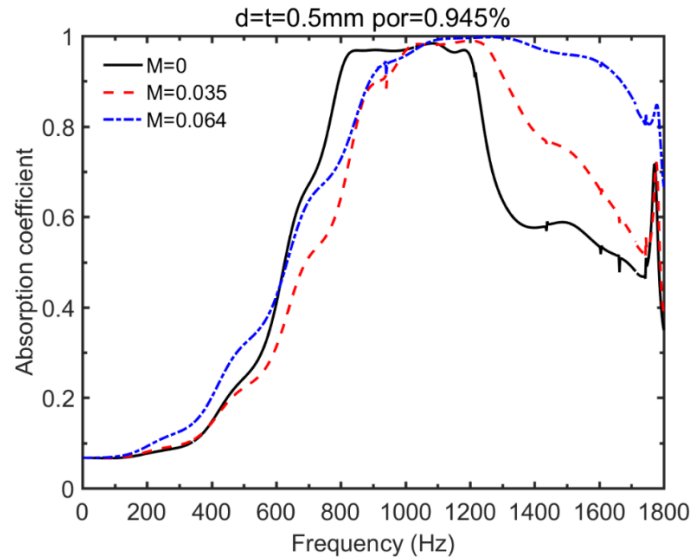


Figure 6.16. Absorption coefficient curves of the range hood model with MPP under different flow velocities.

The influence of the hole diameter with the grazing flow is presented in Fig. 6.17. The plotted TL curves correspond to MPPs with three different hole diameters, ranging from 0.3 to 0.8 mm. The thickness of the panel is taken as the same with the diameter of the hole and the perforation ratio remains $\delta=0.945\%$. It can be seen that different hole diameter gives rise to quite different TL response. The increase of the hole diameter moves the Helmholtz-type resonance induced TL peak toward a lower frequency and changes the corresponding peak value. However, as expected, no noticeable variations on the TL peaks, induced by the reflection effects of the system without MPP, can be observed. The results also indicate that a smaller hole is generally beneficial to improve the silencing performance with a wider attenuation bandwidth. It should be noted that this is only true for locally reacting cases, since the discussions in Section 5.5.2 indicate that locally reacting MPPs can only provide absorption effects. As to the non-locally reacting cases, however, the MPPs show hybrid behavior: both dissipative and reflective. Under these circumstances, to achieve optimal broadband performance, a balance between the dissipation and reflection effects needs to be struck and the panel with a small hole size may not necessarily be the best choice. The one with a proper hole diameter may provide the best combination of the dissipation and reflections.

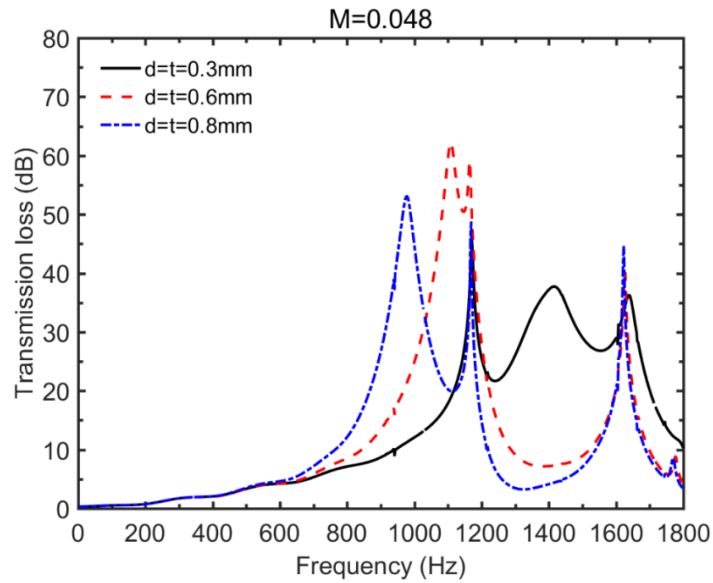


Figure 6.17. TL curves of the range hood model with MPP having different diameters under grazing flow.

Besides the diameter of the hole, the effects of the perforation ratio are also examined (not shown here), the main conclusion drawn from these analyses is that the TL is sensitive to the variations of MPP parameters in the presence of grazing flow. These effects can be predicted from the variation of the sound absorptions of the MPPs.

The above discussions indicate that the TL of the system is sensitive to many system parameters. Therefore, there is a considerable room for parameter tuning to achieve the so-called optimized system. To illustrate this and the potential advantages of the PFT approach, the following analyses show an example of optimization to find the best parameter combination to achieve the ultimate TL performance.

6.3.4. Optimizations

As an illustrative example, an optimization is performed through the tuning of two MPP parameters: the perforation ratio δ and the diameter of the hole d . For a given incident sound power, the total transmitted sound power in a prescribed frequency range is used to evaluate the silencing performance of the system, which is expressed as

$$\Pi_{sum}^{out}(d, \delta) = \int_{f_l}^{f_u} \Pi^{out}(f) df = \sum_{i=1}^{N_f} \Pi_i^{out}, \quad (6.8)$$

where f_l and f_u are the lower and upper bounds of the target frequency range, respectively; N_f is the number of discrete frequency points used for calculation and Π_i^{out} is the transmitted sound power at one discrete frequency point i in the target frequency range.

A better acoustic performance means a lower total transmitted sound power in the target frequency range. Hence, the whole optimization process is to find the optimal parameters to generate this minimum value. The problem can be formulated as:

$$\min. \Pi_{sum}^{out}(d, \delta), \quad (6.9a)$$

$$\text{s.t. } 0.1 \leq d \leq 0.9, \Delta d = 0.05 \text{ mm}, \quad (6.9b)$$

$$0.6\% \leq \delta \leq 2\%, \Delta \delta = 0.1\%, \quad (6.9c)$$

where Π_{sum}^{out} is the objective function; min. is the abbreviation of *minimize* and s.t. is the abbreviation of *subject to*. The constraint condition Eq. 6.9b imposes a restriction on the diameter of the perforation hole, which is incremented by a step of 0.05 mm (17 points in total). The constraint condition in Eq. 6.9c indicates that perforation ratio is varied within the constraint range from 0.6% to 2% with an increment of 0.1% amounting to a total of 15 points. Overall, this results in 255 different combinations of d and δ .

Two optimized problems are defined. The first case considers a broadband optimization, targeting a frequency range from 500 to 1700 Hz with an increment of 10 Hz. Owing to the sub-structure treatment, during the optimization process, only the subsystems being changed need to be recalculated. In the current case, only the mobility matrix of the MPP Y in Eq. 6.4 needs to be recalculated in each optimization loop, while the recalculations of the acoustic quantities of other subsystems are not needed. Finally, the computational time for the calculations of these 255 cases is less than 10 minutes using a standard personal computer, which further demonstrates the efficiency of the PTF approach for the design of MPPs in complex acoustic environment.

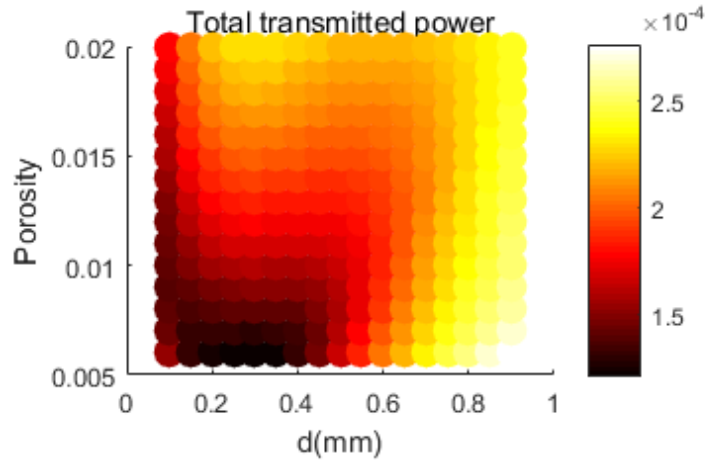


Figure 6.18. Distribution of the total transmitted power with respect to the diameter of the hole and perforation ratio.

The result of this first optimization study case is shown in Fig. 6.18, which shows the distribution of the total transmitted sound power defined in Eq. 6.8 with respect to d and δ . Results demonstrate the existence of a minimum total transmitted power and the corresponding MPP parameters to get the optimized acoustic mitigation performance. Within the pre-defined constraint range, the combination with $d = 0.3mm$ and $\delta = 0.6\%$ can best meet the designed requirement. The corresponding TL curve along with that of the model without MPP are compared in Fig. 6.19. The comparison clearly shows that the optimized configuration warrants significantly improved TL in the target frequency range and exhibits broadband TL characteristics compared with the one without MPP.

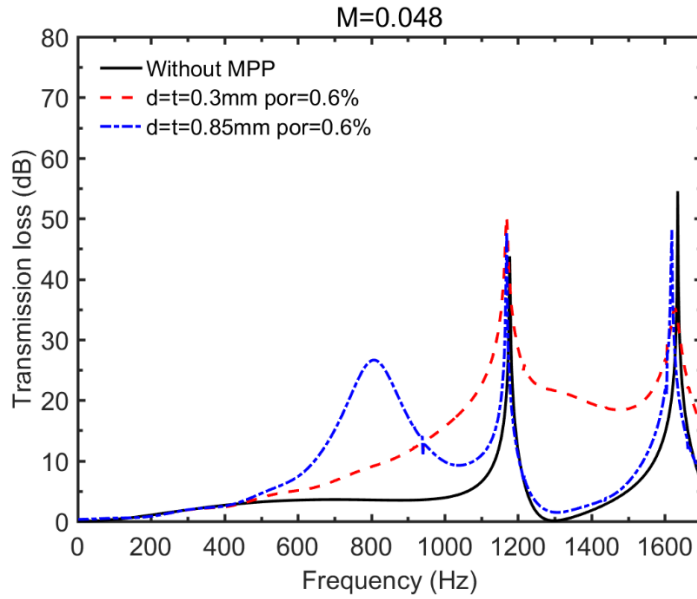


Figure 6.19. TL curves of optimization and empty model.

As an additional example, the targeted frequency range is set from 300 to 1200 Hz, thus a narrower and lower frequency bandwidth. The optimization process finally results in an optimal combination with $d = 0.85\text{mm}$ and $\delta=0.6\%$. The corresponding TL curve is also plotted in Fig. 6.19, showing that the TL of the system in the targeted frequency range can be significantly improved by the optimized combination.

To get further insights into the optimization results, the absorption and reflection curves for both case 1 and case 2 are plotted in Fig. 6.20 and 6.21, respectively. Fig. 6.20 shows that the broadband TL of the system is mostly due to the absorption effect provided by the MPP with a small hole size, which is consistent with the analyses in Section 5.5.3.1 in that for locally reacting case MPPs, smaller holes can provide wider acoustic attenuation performance. However, the results shown in Fig. 6.21 indicate that

the optimized silencing performance from 300 to 1200 Hz in case 2 is achieved by simultaneous absorption and reflection effects. Below 1000 Hz the absorption effect dominates, while above it the absorption effect decreases while the reflection effect increases correspondingly to provide compensation. This can be explained by the fact that the diameter of the hole in case 2 is relatively large. As a result, the absorption bandwidth is not wide enough to cover the entire targeted frequency range. Therefore, reflections are needed. This eventually results in a balanced hybrid effect in the system.

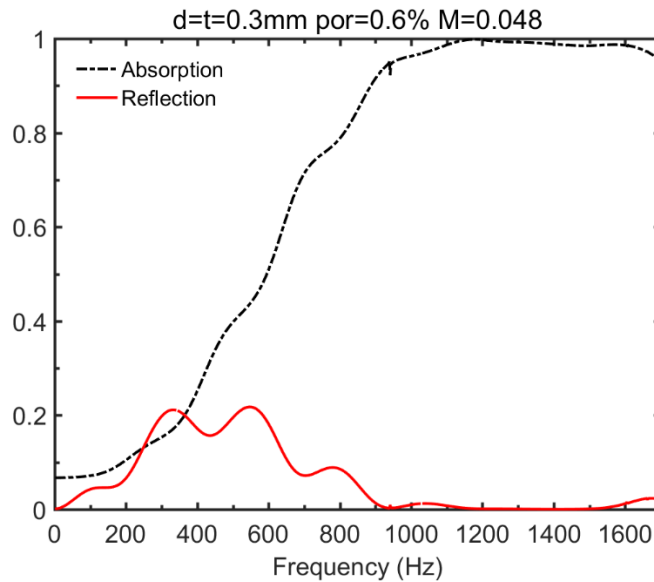


Figure 6.20. Sound absorption and reflection coefficient curves for the first optimization case.

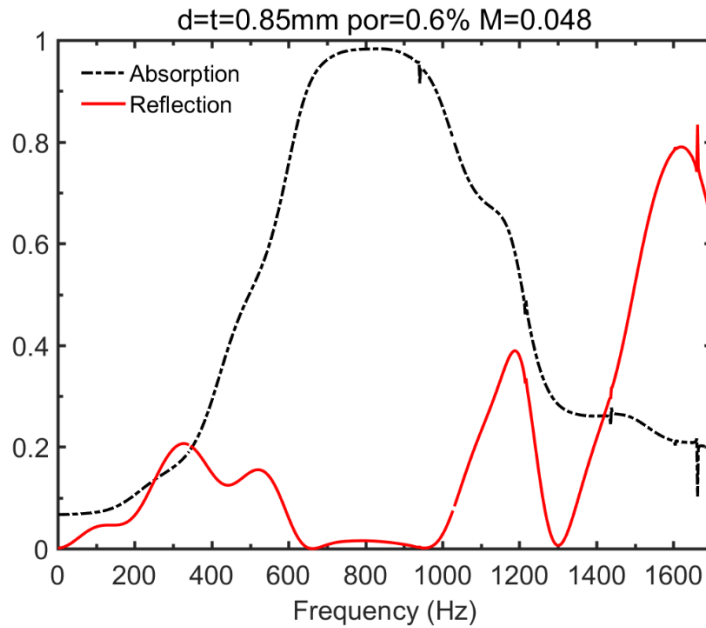


Figure 6.21. Sound absorption and reflection coefficient curves for the second optimization case.

The above discussions demonstrate the capability of the PTF approach as a practical design and optimization tool for the design of MPPs to achieve desired silencing performance in a complex acoustic environment with grazing flow. Note that, more variables can also be integrated into the optimization model for any given problem considering the demonstrated efficiency and flexibility of the PTF approach.

6.4. Improved PTF approach for systems with geometric complexities

The hybrid theoretical-numerical treatment presented above only allows for the system optimization through tuning system parameters related to MPP. It becomes

cumbersome when more complex subsystem parameters, such as the shape of the irregular acoustic cavities, are also included into the optimization process, since the PTFs of these irregular cavities are calculated through FEM. Therefore, an efficient treatment of the subsystems with irregular geometry is needed.

In the following, a new technique based on coordinate transformation is proposed to calculate the PTFs of an irregular shape cavity, exemplified by a trapezoidal cavity. Upon establishing its formulation and validation, the proposed technique is integrated into the previous PTF framework.

6.4.1. PTF calculations of irregular cavity with coordinate transformation

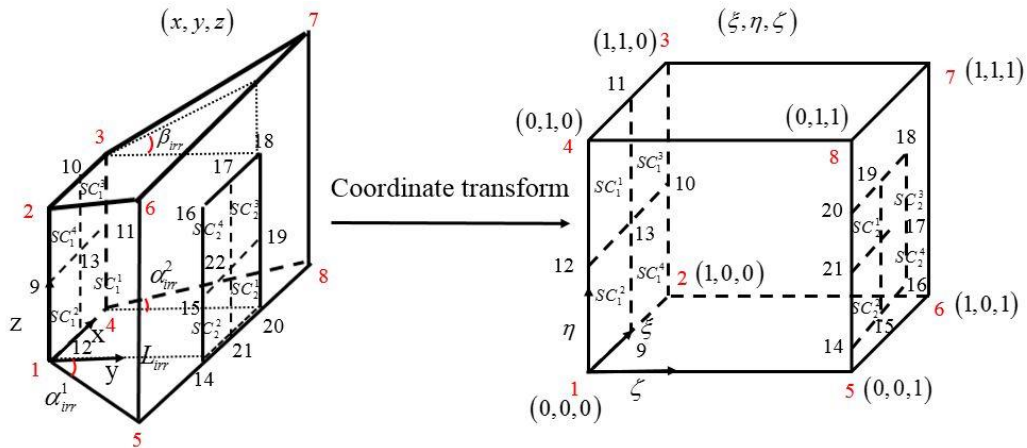


Figure 6.22. Illustration of coordinate transformation technique.

Consider a trapezoidal cavity shown in Fig. 6.22. Its description in the physical x-

y-z coordinate system can be mapped into a regular rectangular cavity with unit length described in a different coordinate system ξ - η - ζ by performing coordinate transformation, as shown in Fig. 6.22. After transformation, the PTF calculations of the irregular cavity with inclined walls can be analytically performed since the geometry of the transformed cavity has a regular and simple shape.

The mapping relationship between these two coordinate systems can be determined by the location relationship of eight vertexes (x_i, y_i, z_i) of the trapezoidal cavity shown in Fig. 6.22 through the following equations:

$$\begin{aligned} x &= N_1x_1 + N_2x_2 + N_3x_3 + N_4x_4 + N_5x_5 + N_6x_6 + N_7x_7 + N_8x_8, \\ y &= N_1y_1 + N_2y_2 + N_3y_3 + N_4y_4 + N_5y_5 + N_6y_6 + N_7y_7 + N_8y_8, \\ z &= N_1z_1 + N_2z_2 + N_3z_3 + N_4z_4 + N_5z_5 + N_6z_6 + N_7z_7 + N_8z_8, \end{aligned} \quad (6.10)$$

where

$$\begin{aligned} N_1 &= (1-\xi)(1-\eta)(1-\zeta), \quad N_2 = \xi(1-\eta)(1-\zeta), \\ N_3 &= \xi\eta(1-\zeta), \quad N_4 = (1-\xi)\eta(1-\zeta), \\ N_5 &= (1-\xi)(1-\eta)\zeta, \quad N_6 = \xi(1-\eta)\zeta, \\ N_7 &= \xi\eta\zeta, \quad N_8 = (1-\xi)\eta\zeta. \end{aligned} \quad (6.11)$$

Based on Eqs. 6.10 and 6.11, the relationship between the first spatial derivative with respect to x , y , z and ξ , η , ζ can be expressed as follows

$$\begin{pmatrix} \frac{\partial(O)}{\partial\xi} \\ \frac{\partial(O)}{\partial\eta} \\ \frac{\partial(O)}{\partial\zeta} \end{pmatrix} = \begin{bmatrix} \frac{\partial x}{\partial\xi} & \frac{\partial y}{\partial\xi} & \frac{\partial z}{\partial\xi} \\ \frac{\partial x}{\partial\eta} & \frac{\partial y}{\partial\eta} & \frac{\partial z}{\partial\eta} \\ \frac{\partial x}{\partial\zeta} & \frac{\partial y}{\partial\zeta} & \frac{\partial z}{\partial\zeta} \end{bmatrix} \begin{pmatrix} \frac{\partial(O)}{\partial x} \\ \frac{\partial(O)}{\partial y} \\ \frac{\partial(O)}{\partial z} \end{pmatrix} = \mathbf{J} \begin{pmatrix} \frac{\partial(O)}{\partial x} \\ \frac{\partial(O)}{\partial y} \\ \frac{\partial(O)}{\partial z} \end{pmatrix}, \quad (6.12)$$

where \mathbf{J} is called Jacobin matrix. The elements of the first column of this matrix write

$$\begin{aligned} \frac{\partial x}{\partial\xi} &= (-x_1 + x_2 - x_3 + x_4 + x_5 - x_6 + x_7 - x_8)\eta\zeta + (x_1 - x_2 + x_3 - x_4)\eta \\ &\quad + (x_1 - x_2 - x_5 + x_6)\zeta - x_1 + x_2 \end{aligned}, \quad (6.13 \text{ a})$$

$$\begin{aligned} \frac{\partial x}{\partial\eta} &= (-x_1 + x_2 - x_3 + x_4 + x_5 - x_6 + x_7 - x_8)\xi\zeta + (x_1 - x_2 + x_3 - x_4)\xi \\ &\quad + (x_1 - x_4 - x_5 + x_8)\zeta - x_1 + x_4 \end{aligned}, \quad (6.13 \text{ b})$$

$$\begin{aligned} \frac{\partial x}{\partial\zeta} &= (-x_1 + x_2 - x_3 + x_4 + x_5 - x_6 + x_7 - x_8)\xi\eta + (x_1 - x_4 - x_5 + x_8)\eta \\ &\quad + (x_1 - x_2 - x_5 + x_6)\xi - x_1 + x_5 \end{aligned}. \quad (6.13 \text{ c})$$

The pressure of a point in the irregular cavity $p_{irr}(x, y, z)$, is expressed as the summation of a series of cosine functions, expressed in terms of their corresponding locations in the transformed regular cavity as

$$p_{irr}(x, y, z) = p_{irr}(\xi, \eta, \zeta) = \sum_{m_\xi=0}^{N_\xi} \sum_{m_\eta=0}^{N_\eta} \sum_{m_\zeta=0}^{N_\zeta} \phi_{m_\xi m_\eta m_\zeta} \cos(m_\xi \pi \xi) \cos(m_\eta \pi \eta) \cos(m_\zeta \pi \zeta), \quad (6.14)$$

where $\phi_{m_\xi m_\eta m_\zeta}$ is the unknown coefficient.

The unknown coefficients $\phi_{m_\xi m_\eta m_\zeta}$ in Eq. 6.14 are to be determined based on the

energy principle. The total potential U_{irr} and kinetic energies T_{irr} of the trapezoidal cavity are expressed as

$$U_{irr} = \frac{1}{2\rho c^2} \int_V p_{irr}^2(x, y, z) dV = \frac{1}{2\rho c^2} \int_0^1 \int_0^1 \int_0^1 p_{irr}^2(\xi, \eta, \zeta) |\mathbf{J}| d\xi d\eta d\zeta, \quad (6.15)$$

and

$$\begin{aligned} T_{irr} &= \frac{1}{2\rho\omega^2} \int_V \left(\frac{\partial p_{irr}(x, y, z)}{\partial x} \right)^2 + \left(\frac{\partial p_{irr}(x, y, z)}{\partial y} \right)^2 + \left(\frac{\partial p_{irr}(x, y, z)}{\partial z} \right)^2 dV \\ &= \frac{1}{2\rho\omega^2} \int_0^1 \int_0^1 \int_0^1 \left[\left([\mathbf{J}^{-1}]_{11} \frac{\partial p_{irr}(\xi, \eta, \zeta)}{\partial \xi} + [\mathbf{J}^{-1}]_{12} \frac{\partial p_{irr}(\xi, \eta, \zeta)}{\partial \eta} + [\mathbf{J}^{-1}]_{13} \frac{\partial p_{irr}(\xi, \eta, \zeta)}{\partial \zeta} \right)^2 \right. \\ &\quad + \left([\mathbf{J}^{-1}]_{21} \frac{\partial p_{irr}(\xi, \eta, \zeta)}{\partial \xi} + [\mathbf{J}^{-1}]_{22} \frac{\partial p_{irr}(\xi, \eta, \zeta)}{\partial \eta} + [\mathbf{J}^{-1}]_{23} \frac{\partial p_{irr}(\xi, \eta, \zeta)}{\partial \zeta} \right)^2 \\ &\quad \left. + \left([\mathbf{J}^{-1}]_{31} \frac{\partial p_{irr}(\xi, \eta, \zeta)}{\partial \xi} + [\mathbf{J}^{-1}]_{32} \frac{\partial p_{irr}(\xi, \eta, \zeta)}{\partial \eta} + [\mathbf{J}^{-1}]_{33} \frac{\partial p_{irr}(\xi, \eta, \zeta)}{\partial \zeta} \right)^2 \right] |\mathbf{J}| d\xi d\eta d\zeta \end{aligned} \quad (6.16)$$

where \mathbf{J}^{-1} is the inverse of Jacobin matrix \mathbf{J} , and $[\mathbf{J}^{-1}]_{ij}$ is the element (i, j) in matrix \mathbf{J}^{-1} .

The work done by one excitation patch of the trapezoidal cavity, like the patch on the interface where $y = 0$ shown in Fig. 6.22, excited with uniformly distributed unit displacement is written as,

$$W_e = \int_{x_1^e}^{x_2^e} \int_{z_1^e}^{z_2^e} p_{irr}(x, 0, z) dx dz = \int_{\xi_1^e}^{\xi_2^e} \int_{\eta_1^e}^{\eta_2^e} p_{irr}(\xi, \eta, 0) |\mathbf{J}_{2 \times 2}| d\xi d\eta, \quad \forall e \in [1, \dots, N_2], \quad (6.17)$$

where $\mathbf{J}_{2 \times 2} = \begin{bmatrix} \frac{\partial x}{\partial \xi} & \frac{\partial z}{\partial \xi} \\ \frac{\partial x}{\partial \eta} & \frac{\partial z}{\partial \eta} \end{bmatrix}$.

The Lagrangian for the trapezoidal acoustical cavity can be written as

$$L = U_{irr} - T_{irr} - W_e. \quad (6.18)$$

Applying Lagrange equation with respect to all the unknown coefficients yields

$$\frac{dL}{dt} \left(\frac{\partial L}{\partial \dot{\phi}_{m_\xi m_\eta m_\zeta}} \right) - \frac{\partial L}{\partial \phi_{m_\xi m_\eta m_\zeta}} = \frac{\partial L}{\partial \phi_{m_\xi m_\eta m_\zeta}} = 0, \quad \forall m_I \in [0, \dots, N_I], \quad (6.19)$$

where the subscript index I can be ξ , η or ζ .

The above equations can then be written in the following condensed matrix form:

$$\left(\mathbf{M}_{irr} - \frac{\mathbf{K}_{irr}}{\omega^2} \right) \boldsymbol{\phi} = \mathbf{W}, \quad (6.20)$$

where \mathbf{M}_{irr} and \mathbf{K}_{irr} can be interpreted as the mass and stiffness matrices of the irregular cavity with rigid walls, $\boldsymbol{\phi}$ is the unknown coefficient vector and \mathbf{W} is the external work vector done by one excitation patch of the trapezoidal cavity.

Once Eq. 6.20 is solved, the unknown coefficient $\phi_{m_\xi m_\eta m_z}$ can then be obtained, which allows the calculation of the pressure field in the irregular cavity through Eq. 6.14.

Finally, according to Eq. 5.2, the PTF between patches in the irregular cavity, for example, when the receiving patch is on the interface where $y = 0$ shown in Fig. 6.22, can be obtained as

$$Z_{re}^{irr} = \frac{\bar{P}_{irr}^r}{\bar{u}_{irr}^e} = \frac{\bar{P}_{irr}^r}{j\omega} = \frac{\int_{\xi_1^r}^{\xi_2^r} \int_{\eta_1^r}^{\eta_2^r} P_{irr}(\xi, \eta, 0) d\xi d\eta}{j\omega S_{rec}^r}, \quad (6.21)$$

where S_{rec}^r is the surface area of one receiving patch in the transformed rectangular cavity.

The accuracy of the proposed technique is validated through comparison with FEM results. The TL curves of the complex system shown in Fig. 6.3 in the no-flow case are compared in Fig. 6.23, showing good agreement, which confirms the validity of the coordinate transformation technique.

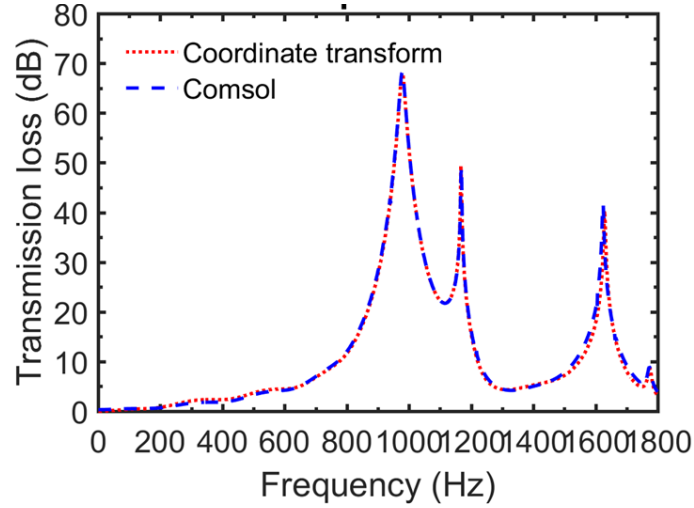


Figure 6.23. Comparison of the TL curve between coordinate transform technique and FEM method, $d = t = 0.5\text{mm}$, $\delta = 0.945\%$ and $M = 0$.

6.4.2. Effects of the shape of irregular cavity

Since the PTFs of the irregular trapezoidal cavity can now be analytically calculated through coordinate transformation, it is convenient to explore the effects of the cavity shape on the TL performance of the system. As illustrated in Fig. 6.22, the shape of the trapezoidal cavity is determined by its depth L_{irr} and the inclined angles of three tilted walls, α_{irr}^1 , α_{irr}^2 and β_{irr} . In the following simulations, the basic geometric configuration of the model remains unchanged and three tilted walls are inclined with the same angle ($\alpha_{irr}^1 = \alpha_{irr}^2 = \beta_{irr}$), the cavity depth L_{irr} and inclined angles of the tilted walls are varied.

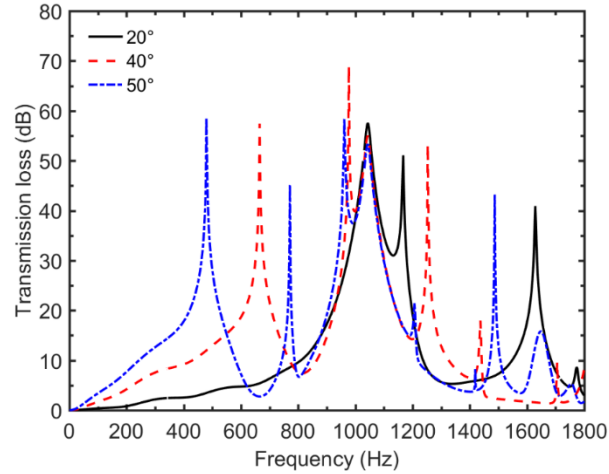


Figure 6.24. TL curves of the range hood model having MPP with the trapezoidal cavity having different inclined angles, $d = t = 0.7mm$, $\delta = 1\%$ and $M = 0.048$.

The effects of the inclined angle are examined firstly. The TL curves of the system with MPP having different inclined angles of the trapezoidal cavity under grazing flow are compared in Fig. 6.24. Results show that the inclined angle of the tilted walls obviously affects the silencing performance of the system. More specifically, increasing the inclined angle, the number of the peaks on the TL curve increases, with peaks shifted toward lower frequency range; consequently, the TL performance in low frequency range is improved. The reason is that, except for the peak induced by the absorption effects provided by the MPP absorber at $f = 1043Hz$, other peaks are generated by the reflection effects due to the impedance mismatch induced by the cross-sectional changes in the trapezoidal part of the model. The locations of these peaks correspond to the natural frequencies of the irregular cavity. Since the resonant frequencies decrease and the number increases in the frequency range of interest with respect to the

increasing size of the cavity, more cavity modes are excited, thus leading to an increase in the number of peaks on the TL curve and downward shift of the TL peaks when the angle of the tilted walls increases.

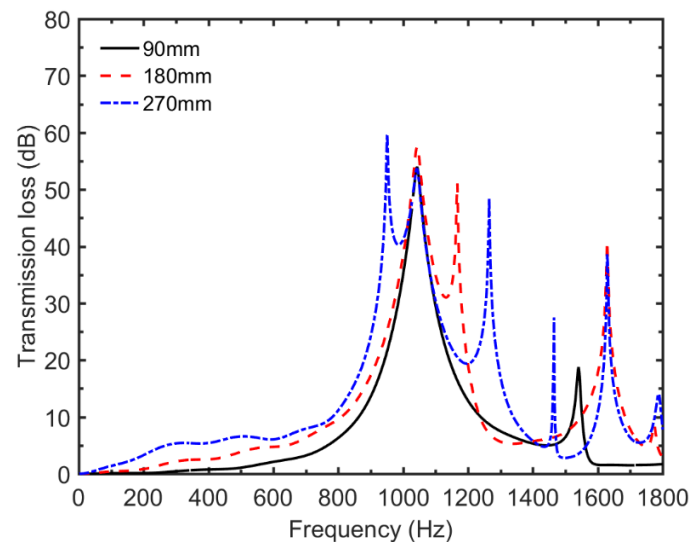


Figure 6.25. TL curves of the range hood model with MPP having different irregular cavity depths, $d = t = 0.7\text{mm}$, $\delta = 1\%$ and $M = 0.048$.

The influence of the trapezoidal cavity depth is shown in Fig. 6.25, for irregular cavities with three different depths, ranging from 90 to 270 mm. It can be seen that different cavity depths give rise to quite different TLs. Since the increase of the cavity depth can also lead to the increase of the irregular cavity dimension, the changes on the TL curves induced by the increase of the inclined angles can also be observed when the cavity depth increases, such as the increase in the number of peaks on the TL curve and the shift of TL peaks toward lower frequencies and the improvement of low frequency TL performance.

The above discussions indicate that the TL of the system is sensitive to the shape of the irregular cavity. An eventual optimal design need to take this factor into account.

6.4.3. Optimizations

To show the improvement brought about by further considering the cavity shape, the optimization study performed in Sec. 6.3.4 is revisited hereafter. The objective function, the constraints imposed on the hole diameter and perforation ratio of the MPP (Eq. 6.9) as well as the target frequency range for two optimization cases, case 1 and case 2, where the frequency range is set from 500 to 1700 Hz and 300 to 1200 Hz, respectively, both with an increment of 10 Hz, all remain the same as before. The only difference is that the parameters determine the shape of the irregular sub-system, inclined angles of three tilted walls (set to be the same) and the depth of the trapezoidal cavity, are now included in the optimization process. The constraints imposed on these two parameters are described as

$$0.12m \leq L_{irr} \leq 0.24m, \quad \Delta L_{irr} = 0.03m, \quad (6.22a)$$

$$20^\circ \leq \beta_{irr} = \alpha_{irr}^1 = \alpha_{irr}^2 \leq 60^\circ, \quad \Delta \beta_{irr} = 10^\circ. \quad (6.22b)$$

A total of 6375 different combinations are generated and calculated for each optimization case. The total computation time for the entire calculations is less than 6

hours using a standard personal computer, which demonstrates the efficiency of the improved PTF approach to model systems with complex geometry. The optimization process finally results in an optimal combination with $d = 0.3mm$, $\delta = 0.6\%$, $L_{irr} = 0.18m$, $\beta_{irr} = 30^\circ$ for case 1 and $d = 0.7mm$, $\delta = 0.6\%$, $L_{irr} = 0.21m$, $\beta_{irr} = 40^\circ$ for case 2.

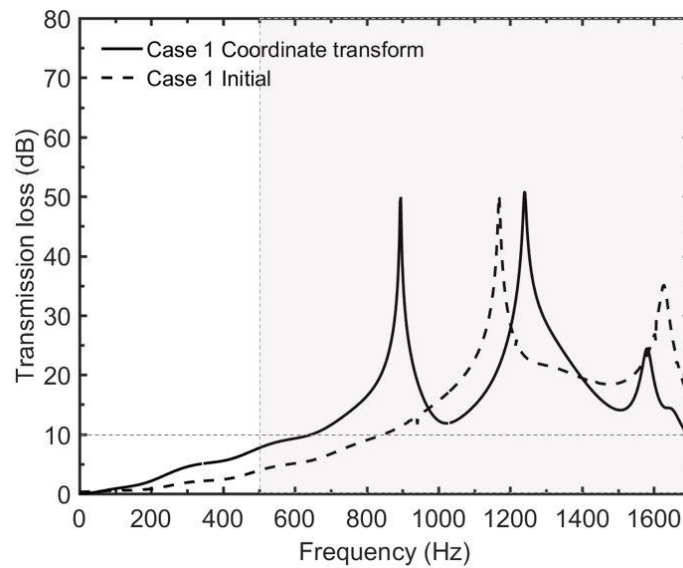


Figure 6.26. Optimized TL curves for case 1, $M = 0.048$.

The optimized TL curve achieved from employing coordinate transformation technique with the shape of the irregular cavity being considered and the one presented in Section 6.3.4 achieved by using hybrid theoretical-numerical treatment without considering the shape of the irregular cavity are compared in Fig. 6.26. It can be seen that for case 1, detailed in Section 6.3.4, where the target frequency range is set from 500 to 1700 Hz with an increment of 10 Hz, after using coordinate transformation

technique and including more system parameters, an additional peak appears on the optimized TL curve, which results in an enlargement of 10dB TL stop bandwidth. The optimized TL performance in the target frequency range is further improved as compared with the result from hybrid theoretical-numerical treatment. It is reasonable since the optimized combination result indicates that the inclined angle is increased from $\beta_{irr} = 20^\circ$ to $\beta_{irr} = 30^\circ$ after including the shape of the irregular cavity into the optimization process, the increase of the inclined angle generates additional peak on the TL curve as analyzed before. The improvement on the TL curve has also been observed from the comparisons with the other case (not shown here). These analyzes demonstrate that, by considering shape changes after integrating the coordinate transformation technique into the framework of PTF approach, the efficacy of the proposed approach is further improved. Note that, through system mapping, cavities with more general irregular shape can be dealt with. As a result, the proposed improved PTF approach actually can be applied to more general cases, not limited to the trapezoidal cavity investigated in the current work.

6.5. Summary

Through a combined numerical and experimental investigation, the potential of using MPPs in complex acoustic environment with grazing flow is explored. To tackle the numerical challenges and to facilitate the design of MPPs, the PTF approach is employed. The patch-based interface matching technique, loosely selected meshing

criteria and the modular nature of the present method collectively make it an efficient and practical tool for the design of practical industrial devices with MPP.

The hybrid theoretical-numerical technique based on PTF approach is firstly employed to numerically predict the acoustic behavior of a mock-up of a range hood having a complex geometry with MPP under grazing flow. An experiment is conducted to validate the numerical method and the accuracy of the calculations. The presented numerical simulations show that with MPP, the silencing performance of the range hood model can be significantly improved and be used for noise mitigation. With MPPs, the system shows a hybrid acoustic attenuation mechanism. Upon ensuring a proper balance among these effects through a suitable parameter tuning, a broadband silencing performance can be achieved. The influence of the grazing flow and the associated MPP parameters are investigated through parametric study. Results show that the silencing performance of the system is sensitive to the presence of grazing flow and other system parameters, and to meet specific TL requirements, system optimization is needed and definitely possible. As such, two optimization examples are given, with results further demonstrating the effectiveness of the presented hybrid theoretical-numerical method for the practical design of MPPs in complex acoustic environment with grazing flow. Finally, a coordinate transformation technique is proposed to calculate the PTFs of irregular subsystems. After integrating this technique into the PTF framework, the efficacy of the PTF approach is further improved as demonstrated by the revisited optimization study.

Chapter 7. Conclusions and Future Work

This thesis examines the acoustic behavior of MPPs under fully developed grazing flow in the linear low acoustic excitation region as well as typical applications in complex acoustic environment with grazing flow.

To deepen the understanding of the flow-acoustic interaction, the grazing flow and the acoustic wave-excited flow field near the orifice of the MPPs under different flow and excitation conditions are first scrutinized through 3D URANS CFD method. Based on the flow field analyses, the underlying physics of the flow-MPP interaction are revealed, mainly from three aspects: 1) The resistance effects of the vortex in the hole, as well as the movement of the shear layer above the hole are shown to be negligible. Within the considered linear acoustic regime, the viscous dissipation in the shear layer near the hole is identified as the dominant sound energy dissipation mechanism, which will gradually be taken over by the chaotic vortex shedding effect when the acoustic excitation SPL increases; 2) The reason behind the increase of the acoustic resistance with flow velocity is found to be a result of the enhancement of the viscous effect near the wall of the hole due to the increased size of the vortex in the hole with flow velocity; 3) The velocity gradient in the viscous sublayer over the duct wall is identified as the intrinsic flow parameter which is inherently correlated with the acoustic resistance of the MPPs with grazing flow.

Following the flow field analyses, numerical experiments are carried out, and a linear relationship between the velocity gradient in the viscous sublayer and the flow-related part in the acoustic resistance formula is revealed. Based on this linear relationship, a new acoustic resistance formula is proposed, which is shown to be applicable at a certain Reynolds number range under the linear acoustic excitation regime. Combined with Cummings' reactance model, a complete set of the acoustic impedance prediction formulae for MPPs with grazing flow is established. For validations, an inverse impedance derivation method is employed to experimentally obtain the acoustic impedance of a MPP under low-speed grazing flow within a linear acoustic excitation region. The accuracy and the superiority of the proposed prediction formula over the existing ones are demonstrated through comprehensive comparisons with the data provided in the open literature and those from experiments. It is shown that the proposed formula agrees well with the experimental data and outperforms existing models in terms of both prediction accuracy and application range. The impedance formulae are then used to investigate the grazing flow effects on the sound absorptions of infinite MPP absorbers under normal plane acoustic wave excitation. Results indicate that the grazing flow significantly affect the sound absorptions of MPP absorbers, which needs to be considered even for the applications of MPPs in simple acoustic environment.

Applications of MPPs in coupled acoustic environment under grazing flow are also exploited based on the developed impedance prediction formula and the PTF

approach. Investigations of MPPs in flow ducts show that partitions inside the backing cavity significantly affect the acoustic attenuation performance of the MPP silencers. The design of the backing cavity should be determined based on specific needs. Grazing flow typically shifts the TL peak to a higher frequency, alters its maximum level and flattens the TL curve with a wider bandwidth. The effect of the hole size and that of the perforation ratio on the silencing performance of MPPs under grazing flow are similar to the cases without flow. The panel dimension actually significantly affects the acoustic performance of the MPPs. While exhibiting a more intuitive influencing manner in locally reacting cases, the size of the MPP in a non-partitioned silencer, however, needs more meticulous consideration, which calls for a systematic system optimization to target a prescribed frequency range.

The investigations of MPPs in a domestic device having a more complex geometry and being subjected to flow show that, with MPP, the silencing performance of the range hood model can be significantly improved and be used for noise mitigation. With MPPs, the system shows a hybrid acoustic attenuation mechanism. Upon properly balancing these effects through suitable parameter tuning, a broadband noise attenuation can be achieved. The silencing performance of the system is sensitive to the presence of grazing flow and other system parameters, and to meet specific TL requirements, a system optimization is needed, which can be readily achieved by using the PTF approach established in this thesis.

In summary, the major contributions of this work can be summarized in three aspects.

1). Proposal of a full set of impedance prediction formula. A complete set of acoustic impedance prediction formula for MPPs with fully developed grazing flow under linear acoustic excitation region is established and validated through comparisons with experimental and CFD generated data. This enriches and extends the pioneer work of Maa and fills the gap left over for dealing with MPPs in flow.

2). Revelation of new physical insights. Depending on the energy level of the acoustic excitation, the dominant sound energy dissipation mechanism could be the viscous dissipation in the shear layer near the hole, chaotic vortex shedding effect or the combination of them with grazing flow. The traditionally-believed dissipation mechanisms based on overcoming the resistance effects of the vortex in the hole, or the movement of the shear layer above the hole are found to be negligible for small MPP holes. This new mechanism finally leads to a different explanation on the increase of the acoustic resistance with flow velocity. More specifically, the increase of the viscous force near the wall of the hole with flow velocities is responsible for the increase in the sound energy dissipation through the viscous effects in the shear layer near the hole wall. This is different from the explanations given in the open literature, such as the “blowing away” process, the changes of the extent of the movement of the shear layer above the hole and the variations of the discharge coefficient. Finally, a new flow

parameter, namely the velocity gradient in the viscous sublayer over the duct wall, is identified as the intrinsic flow parameter which can describe the grazing flow effects on the acoustic resistance of the MPPs with grazing flow.

3). Provision of an effective analysis and optimization tool to guide practical applications. The established PTF-based sub-structuring approach allows an effective handling of complex acoustic systems with MPPs as integrative system components. Its application on MPPs in a coupled complex acoustic environment under grazing flow provide useful guidance for practical design of the MPPs.

In addition to the above major conclusions, a few future suggestions arising from the present thesis are proposed.

1) The acoustic impedance formula presented in this work is established and validated based on the data obtained from a square flow duct carrying a fully developed grazing flow within a certain flow speed range. Therefore, strictly speaking, the validated acoustic impedance formulae have only been shown to be applicable to flow ducts in the application range defined in this thesis. As to other more complex cases which go beyond the pre-defined range, like flow with a higher Reynolds number or over an open space, although we still believe that, as far as the grazing incidence is concerned, the proposed formula should still apply to a certain extent, further verifications are definitely needed before a conclusive statement can be made.

2) The current study only considers the acoustic behaviors of the MPPs under fully developed turbulent flow, in which case the thickness of the boundary layer is larger than the diameter of the hole. Although it is often the case in practice, studies of cases where the boundary layer thickness is comparable with or smaller than the size of the hole would probably allow a better understanding on the influence of the boundary layer towards the MPPs.

3) The perforation ratios of the MPPs being investigated in this work are relatively low. As a result, interactions between MPP holes are considered to be weak and negligible. Increasing the perforation ratio, the interactions between holes would increase and affect the acoustic behavior of MPPs. Meanwhile, the current research focuses on the region where MPPs behave linearly under low SPL excitation. Increasing the SPL would definitely affect the acoustic impedance of MPPs. Last but not the least, the temperature effect on the acoustic behavior of MPPs is not considered in this work, which may constitute a real issue for some applications. Therefore, the impedance formulae established in this work should be employed with care. Obviously, more future efforts are still needed to develop the impedance prediction formulae applicable for high perforation ratio, high SPL regime and with possible temperature variations.

4) The presented numerical method, PTF approach, only considers still media with the convection effects on the propagation of acoustic wave ignored. Though reasonable for low-speed flow cases, it does not allow the consideration of the flow convection

effects, or in a more general case, the aero-acoustic noise induced by turbulent flow itself. In addition, the current PFT version only allows the consideration of linear systems. Therefore, its further extension to consider the above factors will definitely be a giant leap forward.

5) In Chapter 6, a hybrid theoretical-numerical technique and an improved PTF approach are presented to extend the applications of MPPs to more real-life and complex systems, with the PTFs of a complex sub-system calculated through either FEM or coordinate transformation technique. Although the capability and the efficiency of these treatments have been well demonstrated, it is definitely desirable if more applications involving complex systems can be explored.

References:

- [1] H. Fuchs, "Alternative fibreless absorbers–New tools and materials for noise control and acoustic comfort," *Acta Acustica united with Acustica*, vol. 87, no. 3, pp. 414-422, 2001.
- [2] J. P. Arenas and M. J. Crocker, "Recent trends in porous sound-absorbing materials," *Sound & vibration*, vol. 44, no. 7, pp. 12-18, 2010.
- [3] M. Delany and E. Bazley, "Acoustical properties of fibrous absorbent materials," *Applied acoustics*, vol. 3, no. 2, pp. 105-116, 1970.
- [4] Y. Miki, "Acoustical properties of porous materials-Modifications of Delany-Bazley models," *Journal of the Acoustical Society of Japan (E)*, vol. 11, no. 1, pp. 19-24, 1990.
- [5] J. F. Allard and Y. Champoux, "New empirical equations for sound propagation in rigid frame fibrous materials," *The Journal of the Acoustical Society of America*, vol. 91, no. 6, pp. 3346-3353, 1992.
- [6] M. A. Biot, "Theory of propagation of elastic waves in a fluid-saturated porous solid. II. Higher frequency range," *The Journal of the acoustical Society of america*, vol. 28, no. 2, pp. 179-191, 1956.
- [7] K. Attenborough, "The influence of microstructure on propagation in porous fibrous absorbents," *Journal of sound and vibration*, vol. 16, no. 3, pp. 419-442, 1971.
- [8] Y. Champoux and M. R. Stinson, "On acoustical models for sound propagation in rigid frame porous materials and the influence of shape factors," *The journal*

- of the acoustical society of America*, vol. 92, no. 2, pp. 1120-1131, 1992.
- [9] K. Attenborough and L. Walker, "Scattering theory for sound absorption in fibrous media," *The Journal of the Acoustical Society of America*, vol. 49, no. 5A, pp. 1331-1338, 1971.
- [10] M. Berengier, M. Stinson, G. Daigle, and J. Hamet, "Porous road pavements: Acoustical characterization and propagation effects," *The Journal of the Acoustical Society of America*, vol. 101, no. 1, pp. 155-162, 1997.
- [11] R. H. Bolt, "On the design of perforated facings for acoustic materials," *The Journal of the Acoustical Society of America*, vol. 19, no. 5, pp. 917-921, 1947.
- [12] J. Lee, "Compact sound absorbers for low frequencies," *Noise Control Eng. J.*, vol. 38, pp. 109-117, 1992.
- [13] N. Atalla and F. Sgard, "Modeling of perforated plates and screens using rigid frame porous models," *Journal of sound and vibration*, vol. 303, no. 1, pp. 195-208, 2007.
- [14] D. Takahashi, "A new method for predicting the sound absorption of perforated absorber systems," *Applied Acoustics*, vol. 51, no. 1, pp. 71-84, 1997.
- [15] A. Selamet, M. Xu, I. J. Lee, and N. Huff, "Analytical approach for sound attenuation in perforated dissipative silencers," *The Journal of the Acoustical Society of America*, vol. 115, no. 5, pp. 2091-2099, 2004.
- [16] I. Lee, A. Selamet, and N. T. Huff, "Impact of perforation impedance on the transmission loss of reactive and dissipative silencers," *The Journal of the Acoustical Society of America*, vol. 120, no. 6, pp. 3706-3713, 2006.

- [17] N. Hillereau, A. Syed, and E. Gutmark, "Measurements of the acoustic attenuation by single layer acoustic liners constructed with simulated porous honeycomb cores," *Journal of sound and vibration*, vol. 286, no. 1-2, pp. 21-36, 2005.
- [18] R. Lord, "The theory of sound," ed: Dover, New York, 1945.
- [19] I. B. Crandall, *Theory of vibrating systems and sound*. D. Van Nostrand Company, 1954.
- [20] D. Y. Maa, "Theory and design of microperforated panel sound-absorbing constructions," *Scientia Sinica*, vol. 18, no. 1, pp. 55-71, 1975.
- [21] L. Sivian, "Acoustic impedance of small orifices," *The Journal of the Acoustical Society of America*, vol. 7, no. 2, pp. 94-101, 1935.
- [22] U. Ingard, "On the theory and design of acoustic resonators," *The Journal of the acoustical society of America*, vol. 25, no. 6, pp. 1037-1061, 1953.
- [23] D.Y. Maa, "Potential of microperforated panel absorber," *the Journal of the Acoustical Society of America*, vol. 104, no. 5, pp. 2861-2866, 1998.
- [24] C. Wang, L. Cheng, J. Pan, and G. Yu, "Sound absorption of a micro-perforated panel backed by an irregular-shaped cavity," *The Journal of the Acoustical Society of America*, vol. 127, no. 1, pp. 238-246, 2010.
- [25] J. Missaoui and L. Cheng, "A combined integro-modal approach for predicting acoustic properties of irregular-shaped cavities," *The Journal of the Acoustical Society of America*, vol. 101, no. 6, pp. 3313-3321, 1997.
- [26] Y. Li and L. Cheng, "Modifications of acoustic modes and coupling due to a

- leaning wall in a rectangular cavity," *The Journal of the Acoustical Society of America*, vol. 116, no. 6, pp. 3312-3318, 2004.
- [27] K. Sum and J. Pan, "Geometrical perturbation of an inclined wall on decay times of acoustic modes in a trapezoidal cavity with an impedance surface," *The Journal of the Acoustical Society of America*, vol. 120, no. 6, pp. 3730-3743, 2006.
- [28] C. Yang, L. Cheng, and J. Pan, "Absorption of oblique incidence sound by a finite micro-perforated panel absorber," *The Journal of the Acoustical Society of America*, vol. 133, no. 1, pp. 201-209, 2013.
- [29] F. Asdrubali and G. Pispola, "Properties of transparent sound-absorbing panels for use in noise barriers," *The Journal of the Acoustical Society of America*, vol. 121, no. 1, pp. 214-221, 2007.
- [30] Y. Wuzhou, "Design and noise reduction of elevated road barrier of micro-perforated panels with linear-change cavity," *Environmental Pollution & Control*, vol. 7, pp. 67-69, 2008.
- [31] T. Yoo, J. S. Bolton, J. Alexander, and D. Slama, "Absorption from finite-sized microperforated panels at arbitrary incidence angles," *한국소음진동공학회 국제 학술 발표 논문집*, pp. 2879-2886, 2008.
- [32] D.Y. Maa and K. Liu, "Sound absorption characteristics of microperforated absorber for random incidence," *Acta Acustica*, vol. 4, p. 000, 2000.
- [33] C. Yang and L. Cheng, "Sound absorption of a baffled cavity-backed micro-perforated panel absorber under oblique and diffused incidence," 2011, pp.

3634-3639(6).

- [34] X. Yu, L. Cheng, and X. You, "Hybrid silencers with micro-perforated panels and internal partitions," *The Journal of the Acoustical Society of America*, vol. 137, no. 2, pp. 951-962, 2015.
- [35] S. Allam and M. Åbom, "A new type of muffler based on microperforated tubes," *Journal of Vibration and Acoustics*, vol. 133, no. 3, p. 031005, 2011.
- [36] S. Huang, S. Li, X. Wang, and D. Mao, "Micro-perforated absorbers with incompletely partitioned cavities," *Applied Acoustics*, vol. 126, pp. 114-119, 2017.
- [37] S. Allam, "Optimal design of compact multi-partition MPP silencers for IC engines noise control," *Noise Control Engineering Journal*, vol. 64, no. 5, pp. 615-626, 2016.
- [38] K. Sakagami, K. Matsutani, and M. Morimoto, "Sound absorption of a double-leaf micro-perforated panel with an air-back cavity and a rigid-back wall: Detailed analysis with a Helmholtz–Kirchhoff integral formulation," *Applied Acoustics*, vol. 71, no. 5, pp. 411-417, 2010.
- [39] T. Bravo, C. Maury, and C. Pinhède, "Enhancing sound absorption and transmission through flexible multi-layer micro-perforated structures," *The Journal of the Acoustical Society of America*, vol. 134, no. 5, pp. 3663-3673, 2013.
- [40] R. L. Mu, M. Toyoda, and D. Takahashi, "Sound insulation characteristics of multi-layer structures with a microperforated panel," *Applied Acoustics*, vol. 72,

- no. 11, pp. 849-855, 2011.
- [41] I. M. Miasa, M. Okuma, G. Kishimoto, and T. Nakahara, "An experimental study of a multi-size microperforated panel absorber," *Journal of System Design and Dynamics*, vol. 1, no. 2, pp. 331-339, 2007.
- [42] I. M. MIASA and M. Okuma, "Theoretical and experimental study on sound absorption of a multi-leaf microperforated panel," *Journal of System Design and Dynamics*, vol. 1, no. 1, pp. 63-72, 2007.
- [43] C. Wang and L. Huang, "On the acoustic properties of parallel arrangement of multiple micro-perforated panel absorbers with different cavity depths," *The Journal of the Acoustical Society of America*, vol. 130, no. 1, pp. 208-218, 2011.
- [44] K. Sakagami, Y. Nagayama, M. Morimoto, and M. Yairi, "Pilot study on wideband sound absorber obtained by combination of two different microperforated panel (MPP) absorbers," *Acoustical science and technology*, vol. 30, no. 2, pp. 154-156, 2009.
- [45] C. Wang, L. Huang, and Y. Zhang, "Oblique incidence sound absorption of parallel arrangement of multiple micro-perforated panel absorbers in a periodic pattern," *Journal of Sound and Vibration*, vol. 333, no. 25, pp. 6828-6842, 2014.
- [46] J. Kang and M. Brocklesby, "Feasibility of applying micro-perforated absorbers in acoustic window systems," *Applied Acoustics*, vol. 66, no. 6, pp. 669-689, 2005.
- [47] J. Kang and Z. Li, "Numerical simulation of an acoustic window system using finite element method," *Acta acustica united with acustica*, vol. 93, no. 1, pp.

- 152-163, 2007.
- [48] R. Corin and L. Weste, "Sound of silence," *iVT International*, pp. 105-107, 2005.
- [49] G. Li and C. K. Mechefske, "A comprehensive experimental study of micro-perforated panel acoustic absorbers in MRI scanners," *Magnetic Resonance Materials in Physics, Biology and Medicine*, vol. 23, no. 3, pp. 177-185, 2010.
- [50] X. Yu, F. Cui, and L. Cheng, "On the acoustic analysis and optimization of ducted ventilation systems using a sub-structuring approach," *The Journal of the Acoustical Society of America*, vol. 139, no. 1, pp. 279-289, 2016.
- [51] L. Maxit, C. Yang, L. Cheng, and J. L. Guyader, "Modeling of micro-perforated panels in a complex vibro-acoustic environment using patch transfer function approach," *The Journal of the Acoustical Society of America*, vol. 131, no. 3, pp. 2118-2130, 2012.
- [52] C. Yang and L. Cheng, "Sound absorption of microperforated panels inside compact acoustic enclosures," *Journal of sound and vibration*, vol. 360, pp. 140-155, 2016.
- [53] C. Yang, L. Cheng, and Z. Hu, "Reducing interior noise in a cylinder using micro-perforated panels," *Applied Acoustics*, vol. 95, pp. 50-56, 2015.
- [54] A. Hersch and B. Walker, "Effect of grazing flow on the acoustic impedance of Helmholtz resonators consisting of single and clustered orifices," *The Journal of the Acoustical Society of America*, vol. 72, no. 2, pp. 642-642, 1982.
- [55] C. Malmay, S. Carbonne, Y. Auregan, and V. Pagneux, "Acoustic impedance measurement with grazing flow," in *AIAA Conference Paper*, 2001.

- [56] X. Jing, X. Sun, J. Wu, and K. Meng, "Effect of Grazing Flow on the Acoustic Impedance of an Orifice," *AIAA journal*, vol. 39, no. 8, 2001.
- [57] K. J. Baumeister and E. J. Rice, "Visual study of the effect of grazing flow on the oscillatory flow in a resonator orifice," 1975.
- [58] T. Rogers and A. Hersh, "The effect of grazing flow on the steady state resistance of square-edged orifices," in *Proceedings of the Second AIAA Aeroacoustics Conference*, 1976.
- [59] P. Doak, N. Halliwell, and P. Nelson, "Fluid dynamics of a flow excited resonance," *J. Sound Vibr., Part I: Experiment*, vol. 78, p. 15, 1981.
- [60] P. Nelson, N. Halliwell, and P. Doak, "Fluid dynamics of a flow excited resonance, Part II: Flow acoustic interaction," *Journal of sound and vibration*, vol. 91, no. 3, pp. 375-402, 1983.
- [61] P. Westervelt, "Acoustical impedance in terms of energy functions," *The Journal of the Acoustical Society of America*, vol. 23, no. 3, pp. 347-348, 1951.
- [62] P. J. Westervelt and P. W. Sieck, "The Correlation of Non-Linear Resistance, Flow Resistance, and Differential Resistance for Sharp-Edged Circular Orifices," *The Journal of the Acoustical Society of America*, vol. 22, no. 5, pp. 680-680, 1950.
- [63] Y. Hirata and T. Itow, "Influence of air flow on the attenuation characteristics of resonator type mufflers," *Acta Acustica united with Acustica*, vol. 28, no. 2, pp. 115-120, 1973.
- [64] D. Ronneberger, "The acoustical impedance of holes in the wall of flow ducts,"

- Journal of Sound and Vibration*, vol. 24, no. 1, pp. 133-150, 1972.
- [65] B. Walker and A. Charwat, "Correlation of the effects of grazing flow on the impedance of Helmholtz resonators," *The Journal of the Acoustical Society of America*, vol. 72, no. 2, pp. 550-555, 1982.
- [66] Q. Zhang, *Direct numerical investigation and reduced-order modeling of 3-D honeycomb acoustic liners*. University of Illinois at Urbana-Champaign, 2014.
- [67] M. Escouflaire, "Theoretical and Numerical Investigation of Time-Domain Impedance Models for Computational AeroAcoustics," Le Mans, 2014.
- [68] M. Howe, M. Scott, and S. Sipcic, "The influence of tangential mean flow on the Rayleigh conductivity of an aperture," in *Proceedings of the Royal Society of London A: Mathematical, Physical and Engineering Sciences*, 1996, vol. 452, no. 1953, pp. 2303-2317: The Royal Society.
- [69] E. J. Rice, "Theoretical study of the acoustic impedance of orifices in the presence of a steady grazing flow," *The Journal of the Acoustical Society of America*, vol. 59, no. S1, pp. S32-S32, 1976.
- [70] R. Kirby and A. Cummings, "The impedance of perforated plates subjected to grazing gas flow and backed by porous media," *Journal of Sound and Vibration*, vol. 217, no. 4, pp. 619-636, 1998.
- [71] B. Phillips, "Effects of high-wave amplitude and mean flow on a Helmholtz resonator," 1968.
- [72] A. B. Bauer, "Impedance theory and measurements on porous acoustic liners," *J. Aircr*, vol. 14, no. 8, pp. 720-728, 1977.

- [73] L. Dean, "Coupling of Helmholtz resonators to improve acoustic liners for turbofan engines at low frequency," 1975.
- [74] T. Elnady and H. Bodén, "An inverse analytical method for extracting liner impedance from pressure measurements," in *Proceedings of the 10th AIAA/CEAS Aeroacoustics Conference, Manchester, UK, May, 2004*, pp. 10-12.
- [75] S. Allam and M. Åbom, "Experimental characterization of acoustic liners with extended reaction," in *The 14th AIAA/CEAS Conference*, 2008, vol. 3074.
- [76] J. Kooi and S. Sarin, "An experimental study of the acoustic impedance of Helmholtz resonator arrays under a turbulent boundary layer," in *AIAA, Astrodynamics Specialist Conference*, 1981.
- [77] A. Cummings, "The effects of grazing turbulent pipe-flow on the impedance of an orifice," *Acta Acustica United with Acustica*, vol. 61, no. 4, pp. 233-242, 1986.
- [78] N. Dickey, A. Selamet, and M. Ciray, "An experimental study of the impedance of perforated plates with grazing flow," *The Journal of the Acoustical Society of America*, vol. 110, no. 5, pp. 2360-2370, 2001.
- [79] S. H. Lee and J. G. Ih, "Empirical model of the acoustic impedance of a circular orifice in grazing mean flow," *The Journal of the Acoustical Society of America*, vol. 114, no. 1, pp. 98-113, 2003.
- [80] A. Goldman and C. Chung, "Impedance of an orifice under a turbulent boundary layer with pressure gradient," *The Journal of the Acoustical Society of America*, vol. 71, no. 3, pp. 573-579, 1982.

- [81] A. Goldman and R. L. Panton, "Measurement of the acoustic impedance of an orifice under a turbulent boundary layer," *The Journal of the Acoustical Society of America*, vol. 60, no. 6, pp. 1397-1405, 1976.
- [82] C. K. Tam and K. A. Kurbatskii, "Micro uid Dynamics and Acoustics of Resonant Liners," *AIAA journal*, vol. 38, no. 8, pp. 1331-1339, 2000.
- [83] K. A. Kurbatskii and C. K. Tam, "Micro-fluid dynamics of a resonant liner in a grazing flow," *AIAA Paper*, vol. 1951, 2000.
- [84] C. K. Tam, H. Ju, and B. E. Walker, "Numerical simulation of a slit resonator in a grazing flow under acoustic excitation," *Journal of Sound and Vibration*, vol. 313, no. 3, pp. 449-471, 2008.
- [85] E. Selamet, A. Selamet, A. Iqbal, and H. Kim, "Effect of Flow on Helmholtz Resonator Acoustics: A Three-Dimensional Computational Study vs. Experiments," SAE Technical Paper0148-7191, 2011.
- [86] C. Liu and Z. Ji, "Computational fluid dynamics-based numerical analysis of acoustic attenuation and flow resistance characteristics of perforated tube silencers," *Journal of Vibration and Acoustics*, vol. 136, no. 2, p. 021006, 2014.
- [87] J. Su, J. Rupp, A. Garmory, and J. F. Carotte, "Measurements and computational fluid dynamics predictions of the acoustic impedance of orifices," *Journal of Sound and Vibration*, vol. 352, pp. 174-191, 2015.
- [88] M. Q. Wu, "Micro-perforated panels for duct silencing," *Noise Control Engineering Journal*, vol. 45, no. 2, pp. 69-77, 1997.
- [89] M. Abom and S. Allam, "Dissipative silencers based on micro-perforated

- plates," SAE Technical Paper0148-7191, 2013.
- [90] J. M. Roche, F. Vuillot, L. Leylekian, G. Delattre, E. P. E. F. SIMON, and E. Piot, "Numerical and experimental study of resonant liners aeroacoustic absorption under grazing flow," in *Proceedings of the 16th AIAA/CEAS Aeroacoustics Conference*, 2010, no. 2010-3767.
- [91] S. B. Pope, "Turbulent flows," ed: IOP Publishing, 2001.
- [92] H. Fujita, "Turbulent flow in smooth and rough-walled square ducts," *Trans. Jpn. Soc. Mech. Eng., Ser. B*, vol. 45, pp. 197-207, 1979.
- [93] W. Y. Wu, S. Weinbaum, and A. Acrivos, "Shear flow over a wall with suction and its application to particle screening," *Journal of Fluid Mechanics*, vol. 243, pp. 489-518, 1992.
- [94] I. J. Sobey, "Laminar boundary-layer flow past a two-dimensional slot," *Journal of Fluid Mechanics*, vol. 83, no. 1, pp. 33-47, 1977.
- [95] S. Smith, "Stokes flow past slits and holes," *International journal of multiphase flow*, vol. 13, no. 2, pp. 219-231, 1987.
- [96] O. Tutty, "Flow in a tube with a small side branch," *Journal of fluid mechanics*, vol. 191, pp. 79-109, 1988.
- [97] A. Davis, "Shear flow disturbance due to a hole in the plane," *Physics of Fluids A: Fluid Dynamics*, vol. 3, no. 3, pp. 478-480, 1991.
- [98] C. Yang, Y. Fang, C. Zhao, and X. Zhang, "On modeling the sound propagation through a lined duct with a modified Ingard-Myers boundary condition," *Journal of Sound and Vibration*, vol. 424, pp. 173-191, 2018.

- [99] M. G. Jones, W. R. Watson, B. M. Howerton, and S. Busse-Gerstengarbe, "Comparative study of impedance reduction methods, Part 2: NASA tests and methodology," in *19th AIAA/CEAS Aeroacoustics Conference*, 2013, p. 2125.
- [100] X. Wang, Y. Choy, and L. Cheng, "Hybrid noise control in a duct using a light micro-perforated plate," *The Journal of the Acoustical Society of America*, vol. 132, no. 6, pp. 3778-3787, 2012.
- [101] X. Shi and C. M. Mak, "Sound attenuation of a periodic array of micro-perforated tube mufflers," *Applied Acoustics*, vol. 115, pp. 15-22, 2017.
- [102] X. Yu, L. Cheng, and X. You, "Hybrid silencers with micro-perforated panels and internal partitions," *Journal of the Acoustical Society of America*, vol. 137, no. 2, pp. 951-962, 2015.
- [103] T. Bravo, C. Maury, and C. Pinhède, "Optimisation of micro-perforated cylindrical silencers in linear and nonlinear regimes," *Journal of Sound and Vibration*, vol. 363, pp. 359-379, 2016.
- [104] A. Selamet and Z. Ji, "Acoustic attenuation performance of circular expansion chambers with extended inlet/outlet," *Journal of Sound and Vibration*, vol. 223, no. 2, pp. 197-212, 1999.
- [105] A. Selamet, F. Denia, and A. Besa, "Acoustic behavior of circular dual-chamber mufflers," *Journal of Sound and Vibration*, vol. 265, no. 5, pp. 967-985, 2003.
- [106] M. Ouisse, L. Maxit, C. Cacciolati, and J. L. Guyader, "Patch transfer functions as a tool to couple linear acoustic problems," *Journal of vibration and acoustics*, vol. 127, no. 5, pp. 458-466, 2005.

- [107] J. D. Chazot and J. L. Guyader, "Prediction of transmission loss of double panels with a patch-mobility method," *The Journal of the Acoustical Society of America*, vol. 121, no. 1, pp. 267-278, 2007.
- [108] X. Yu and L. Cheng, "Duct noise attenuation using reactive silencer with various internal configurations," *Journal of sound and vibration*, vol. 335, pp. 229-244, 2015.
- [109] M. Munjal and A. Doige, "Theory of a two source-location method for direct experimental evaluation of the four-pole parameters of an aeroacoustic element," *Journal of Sound and Vibration*, vol. 141, no. 2, pp. 323-333, 1990.
- [110] M. Åbom, "Measurement of the scattering-matrix of acoustical two-ports," *Mechanical systems and signal processing*, vol. 5, no. 2, pp. 89-104, 1991.